Mass Loading Effect of Resonant Structures in Surface Acoustic Wave Devices Suitable for Sensing Applications

N. Ramakrishnan

அகர முதல எழுத்தெல்லாம் ஆதி
பகவன் முதற்றே உலகு.

"A" is the first and source of all the letters. Even so is
God primordial the first and source for the entire world.
-Thirukural, verse -1

To my

Parents, *Narayanan and Suseela*
Grand Parents, *Srinivasan and Saroja*
Sister, *Aparna*

&

Wife, *Purabi*

Acknowledgement

I feel it as a great privilege in expressing my deepest and most sincere gratitude to my thesis main supervisor Dr. Harshal B. Nemade for his excellent guidance throughout my study. His kindness, dedication, hard work, and attention to detail have been a great inspiration to me. I thank him for the unlimited support and infinite patience he has shown to me. He is more than a supervisor for me. I would like to thank my thesis co-supervisor Dr. Roy Paily Palathinkal, the man from whom I learnt the inner technical aspects of MEMS. His unwavering support, invaluable guidance and suggestions in performing this research and presenting the thesis are extraordinary.

I am thankful to my doctoral committee members Professor A. Srinivasan, Dr. P. K. Giri and Dr. R. Bhattacharjee for sparing their precious time to evaluate the progress of my work. I express my heartfelt thanks to Professor Arun Chattopodhyay for his tremendous support and constant encouragement from the day I joined this Institute. He has boosted my confidence every time. I would like to thank him for all the support he gave me during my stay in IIT Guwahati. I am also thankful to Dr. S. S. Ghosh, head of the centre for providing the facility to carry out the research work.

My special thanks to staff of centre, Dr. Manoranjan Kar, Kaustabh, Indrajit, Paran, and Pranjoli Das without their help I could not have completed this thesis. I would also like extend my thanks to technical staff in ECE Department, IIT Guwahati.

I would like give my sincere thanks to Dr. Amitava Das Gupta and Dr. Nandita Das Gupta, IIT Madras for sharing the micro fabrication facility to carry out some parts of fabrication work. I am highly thankful to Indian Nanoelectronics User Program (INUP), and Centre for Excellence in Nanoelectronics (CEN), IISc., Bangalore for providing the fabrication facility to carry out major part of my experimental work. I would like to thank all faculty coordinators of INUP, In particular I would like to thank Dr. Vijay Mishra, INUP coordinator for his tremendous help and support in carrying out my work in IISc., Bangalore. Most importantly I would like give my gratitude to the INUP staff at CEN, IISc., Bangalore especially Balaji for helping me with most of the fabrication work.

Thanks go out to all my friends in Centre for Nanotechnology - IIT Guwahati, Microelectonics Lab - IIT Madras, INUP-IISc., Bangalore. They have always been around to provide useful suggestions, companionship and created a peaceful research environment. They all contributed directly or indirectly to this thesis. I would like to thank Gowind for helping in sorting out some of the experimental data.

I am extremely thankful to Mrs. Leena Nemade and Mrs. Josephine madam for their care shown and support given to me during my stay at IIT Guwahati. I would like express my thanks to my friends Dr. Gopinath, Monash, Pandian, Krishna, Adaleesan, Ashok, Dr. Atul K Singh, Sukhivinder Singh, Dilip Kumar Singh, Pallab Sanpui, Agile Mathew, Dr. Saravanan, and Dr. Aslam Khan. My work in this remote place definitely would not be possible without their love and care that helped me to enjoy my new life in this IIT Guwahati.

My special thanks to my SAW group member the guys who are always with me, Ashish Kumar Namdeo, Sai Krishna, Vivek Lukose, John Pradeep, Satyam Lama, Omkaram, Vamsi, Subhankar, Jitender, Mandar, and Basudeba, for their care, support, and extreme cooperation during my stay in IIT Guwahati.

During these five years at IIT Guwahati I have had several friends that have helped me in several ways, I would like to say a big thank you to all of them for their friendship and support.

My deepest gratitude goes to my parents, grandparents and sister for their continuous love and support throughout my studies. Especially I want to thank my father for the opportunities he has given me and his unlimited love and support are the reasons where I am and what I have accomplished so far. I want give my most special thanks for Purabi, who is the one giving me the mental support and making my life more colorful.

Finally, I believe this research experience will greatly benefit my career in the future.

N. Ramakrishnan

Certificate

This is to certify that the thesis entitled "**Mass Loading Effect of Resonant Structures in Surface Acoustic Wave Devices Suitable for Sensing Applications**", submitted by N. Ramakrishnan (05615302), a research scholar in the Centre for Nanotechnology, Indian Institute of Technology Guwahati, for the award of the degree of Doctor of Philosophy, is a record of an original research work carried out by him under our supervision and guidance. The thesis has fulfilled all requirements as per the regulations of the institute and in our opinion has reached the standard needed for submission. The results embodied in this thesis have not been submitted to any other University or Institute for the award of any degree or diploma.

Dated:

Guwahati.

Dr. Harshal B. Nemade

Associate Professor

Centre for Nanotechnology and
Dept. of Electronics and Communication Engg.

Indian Institute of Technology Guwahati

Guwahati - 781 039, Assam, India.

Dated:

Guwahati.

Dr. Roy Paily Palathinkal

Associate Professor

Dept. of Electronics and Communication Engg.

Indian Institute of Technology Guwahati

Guwahati - 781 039, Assam, India.

Abstract

Surface acoustic wave (SAW) devices are widely used in sensors, actuators, filters, and telecommunication systems. Surface acoustic waves are elastic waves launched on a piezoelectric substrate when an electrical signal is applied to metallic comb-like electrodes patterned on the surface of the substrate. SAW devices used in sensing applications extensively employ mass loading effect of a sensing film coated over the surface of the device. Changes in the properties of the sensing film due to the measurand cause variation in mass loading that alters the velocity of the surface wave and results in deviation in the electrical properties of the device, e.g. change in resonance frequency in a SAW resonator. Some other properties of sensing films that can affect SAW velocity are conductivity, permittivity, viscosity, and temperature; hence sensing films can be developed accordingly.

In this thesis, mass loading effect of resonant structures (in place of sensing films) has been investigated. High aspect ratio pillars are proposed as the resonant structures to be fabricated on SAW resonators. Finite Element Method (FEM) simulation shows that when the resonance frequency of the pillars is close to the resonance frequency of the resonator, extraordinary changes in mass loading occur. The pillars and the SAW resonator form a system of coupled resonators, and the deviations in the system frequency are large when the resonance frequencies of the two coupled systems are close. The rapid variation in the mass loading characteristics at the resonance frequency can be used to develop highly sensitive sensors. It is observed that the sensitivity with resonant pillars is at least 10 times that obtained by thin film as the sensing medium. FEM simulation is carried out for wide range of pillar dimensions and it is observed that the thinner pillars offer greater sensitivity implying that nano size pillars will be the most desirable sensing medium. As an example, a hydrogen sensor using nano size pillars of palladium as sensing medium has been simulated and the results show high sensitivity for sensing hydrogen at concentrations below 1%.

Experiments are carried out by fabricating SAW resonators with SU-8 micro-pillars of varying dimensions. Experimental results and the FEM simulation show typical characteristics of a system of coupled resonators, viz. increase in frequency in certain cases and the state of zero mass loading. The present work is not restricted to any specific sensor; rather introduces a technique for the development of a novel class of SAW sensors. In addition to the highly sensitive sensors, the technique has potential applications in filters and other SAW devices.

List of Figures

List of Tables

List of Acronyms

APM	Acoustic Plate Mode
BAW	Bulk Acoustic Wave
COM	Coupling of Mode
DI	De-ionized
DOF	Degrees of Freedom
FEM	Finite Element Method
FESEM	Field Emission Scanning Electron Microscope
GUI	Graphical User Interface
HAR	High Aspect Ratio
IDT	Interdigital Transducer
MEMS	Microelectromechanical Systems
NIPAAm	N-isopropylacrylamide
PDE	Partial Differential Equation
RF	Radio Frequency
RFID	Radio Frequency Identification
RH	Relative Humidity
SAW	Surface Acoustic Wave
SEM	Scanning Electron Microscope
SH	Shear Horizontal
TCE	Trichloro ethylene
TEM	Transmission Electron Microscope
TSM	Thickness Shear Mode
UV	Ultraviolet

List of Symbols

α	Transduction coefficient
$< >$	Denote average
σ_{avg}	Average stress at the surface
$\boldsymbol{a}$	Coordinate transform matrix
a_{ij}	Elements in coordinate transform matrix
A_{dm}	Mass proportional damping parameter
β_n	Resonance mode constant
B_a	Radiation susceptance of IDT
$\mathbf{B}$	Magnetic field
B_{dk}	Stiffness proportional damping parameter
C_s	Static capacitance for single pair of electrode
C_T	Total capacitance of IDT
C_{ijkl}^{E}	Elasticity matrix (Stiffness tensor)
d	Length of the SAW delay line
$\Delta\Phi$	Change in phase of SAW
Δv	Change in velocity of SAW
Δf_0	Resonance frequency shift
Δf^*	Complex resonance frequency shift
Δt	Time delay
D	Detuning parameter
$\mathbf{D}$	Electrical displacement
δ	Elementary length of a cube inside a piezoelectric material
E	Youngs modulus of a material

E_n	Electric potential equivalent to F_n (n stands for number of electrodes)
$\mathbf{E}$	Electric field
e_{ijk}	Piezoelectric tensor matrix
ϕ, Θ, and ψ	Euler angles
ε_{ij}^{s}	Permittivity matrix
f	Frequency of operation of the SAW IDT
$f_0\|_{h=0}$ and $f_0\|_{w=0}$	Resonance frequency of the SAW resonator without any sensing medium/pillars
f_0	Resonance frequency of the SAW resonator
f_F	Fundamental resonance frequency of the quartz coupled resonator
f_i	Frequency of the input electric potential to the SAW IDT
F_n	Acoustic terminal force(n stands for number of electrodes)
f_n	n^{th} mode resonance frequency of a cantilever beam
Γ_L	Denotes left side boundary of the SAW resonator geometry
Γ_R	Denotes right side boundary of the SAW resonator geometry
Γ_1, Γ_2	Denotes boundaries of the SAW resonator geometry along its aperture
G_0	Conductance per electrode pair of IDT
G_a	Radiation conductance of IDT
γ	Propagation loss per unit length
Γ_{DL}	Denotes boundary between transmitting IDT and delay line

	in SAW delay line model
$G1$	Represents transmitting IDT in reduced SAW delay line model
$G2$	Represents delay line in reduced SAW delay line model
$G3$	Represents absorber in reduced SAW delay line model
h	Height of sensing medium(thin film or pillar)
I	Cross-section moment of inertia
i_n	Current equivalent to particle velocity for a single pair of electrode of IDT
I_{IDT}	Current due to flow of charges in IDT
j	Imaginary unit
k_1, k_2	Piezoelectric constants, For example, Y-Z lithium niobate has $k_1 = -3.775\times10^{-8}$ m^2skg^{-1} and $k_2 = -1.73\times10^{-8}$ m^2skg^{-1}
K	Spring constant of quartz resonator
k	Force constant or Stiffness constant or contact stiffness of the particle resonator
K^2	Electromechanical coupling coefficient
K_i	Reflection parameter
k_0	Wave number
k_e	Element coefficient matrix
K_1, K_2, K_3	Proportionality constants
k_s	Stiffness of contact of the pillar
λ	Wavelength of SAW
λ'	Bulk modulus of a material
L	Length of IDT

m_p	Mass per unit length of the pillar
m	Mass of the particle resonator
M	Mass of the quartz resonator
M_b	Bond matrix
m_{film}	Mass of the sensing film
μ'	Shear modulus of a material
N	Number of fingers in IDT
N_s	Number density of spheres in particle resonator
$N(r)$	Interpolation function
N_R	Number of finger pair in receiver IDT
ω	Angular frequency ($\omega = 2\pi f$)
ω_0	Angular resonance frequency of the quartz resonator
p	Pitch of the IDT
Φ	Phase of SAW
φ	Turns ratio of an acoustic to electric circuit transforms
φ_a	Phase offset of the gratings of IDT
φ_t	Phase offset in the potential
P_{11} and P_{22}	Reflections coefficients of IDT in P-Matrix
P_{12} and P_{21}	Transmission coefficients of IDT in P-Matrix
P_{13} and P_{23}	Excitation coefficients of IDT in P-Matrix
P_{31} and P_{32}	Current generated by the wave arriving at acoustic ports of IDT
P_{33}	Admittance of IDT in P-matrix
Q_e	Applied load to the FEM model
q_{out}	Charge produced in each finger

r_s	Reflection coefficient of one electrode
ρ	Density of a material
r_p	Pitch of the reflector
R_0	Electrical equivalent of Z_0
R, S	SAW mode amplitudes in P - matrix model of IDT
R_f	Thin film resistance of electrode in one transduction unit
$\mathbf{r}$	Indicates position vector
ς	Piezoelectric constant used in mason equivalent circuit
S_{ij}	Strain at a point in a solid
σ	Stress at the surface of the substrate
t	Time variable
$\mathbf{T}$	Stress (Second rank tensor)
$T_{ij(mech)}$	Stress due to mechanical strain
$T_{ij(mech)}$	Stress due to electric field
$\mathbf{u}$	SAW particle displacement
u'_i	Particle velocity of SAW along i direction
$\mathbf{u'_p}$	Displacement of partial waves
v	Phase velocity of SAW
V_{in}	Input electric potential to IDT
V	Scalar electric potential
V'	Potential of partial waves
V_{in}	Input voltage to IDT
V_o	Output voltage from IDT
W	IDT aperture length
w	Width of the pillar

x_i Co-ordinate axis (i = 1, 2, 3)

ξ Damping ratio

Y_3 Input admittance of IDT

ζ Dissipative component of sphere-plate interaction in quartz coupled resonator

Z_o Acoustic impedence

$\mathbf{Z}$ Rayleigh damping matrix

1

Introduction to Surface Acoustic Wave Sensors

There has been tremendous growth in the microelectromechanical systems (MEMS) industry and subsequent increase in demand for high quality components. Surface acoustic wave (SAW) devices form an important part of MEMS family. A SAW is an acoustic wave traveling along the surface of a material exhibiting elasticity. The amplitude of these waves is higher at the surface and decreases exponentially along the depth of the substrate. The basic principle behind SAW generation and detection is the well known piezoelectricity. In piezoelectric materials electrical charge is produced when mechanically strained and vice versa. The SAW devices exhibit a frequency response according to the properties of surface acoustic waves propagating over their substrate.

SAW devices are one of the major components in many communication systems such as satellite receivers, remote control units, keyless entry system, radio frequency identification (RFID), television sets, and mobile phones. SAW devices are also used as micro actuators such as SAW nano-stepping motors and SAW micropumps. Sensors based on SAWs find diverse applications ranging from gas and vapor detection to strain and pressure measurement. Onboard antennas can be integrated within the SAW devices and applied in sensors for remote and inaccessible locations [1]. There is always a need for superior SAW sensors such as improvement in sensitivity, selectivity, and fabrication techniques. The thesis mainly focuses on the research work carried on novel class of SAW sensors and their characteristics. The results and analysis obtained during the simulation and experiments on these devices are presented in this thesis.

1.1 Types of surface acoustic waves

The relative position changes (strain) in atoms in a solid material appear to be as elastic or acoustic wave. In presence of strain the material experiences internal forces (stresses) which tend them to retain their original equilibrium, unstrained state. Surface acoustic waves, the wave propagates at the surface of the material, whereas bulk waves the wave propagate to the whole extent of the solid. There are two basic types of wave motions: Longitudinal waves are of one type where the displacement of the particle is parallel to the wave propagation direction. Second type is transverse or shear wave, where the displacement is in any direction parallel to the wave front, normal to the propagation direction [2]. The type of acoustic waves generated in a piezoelectric material mainly depends upon substrate material properties, the crystal cut, and the structure of electrodes used in the transducers. The various possible waves that could be employed in SAW sensors are Rayleigh waves, shear horizontal (SH) waves, Love waves, and acoustic plate mode (APM) waves [1].

Rayleigh waves were first identified by Lord Rayleigh in 1885. The particles in an elastic Rayleigh wave have both a surface-normal and a surface parallel component with respect to the direction of propagation. The particles movement takes elliptical path and particle in the surface takes anti-clockwise direction of motion, whereas a particle within a wavelength of distance along the depth of material has clockwise direction of motion [1]. Figure 1 shows displacements for Rayleigh wave propagation.

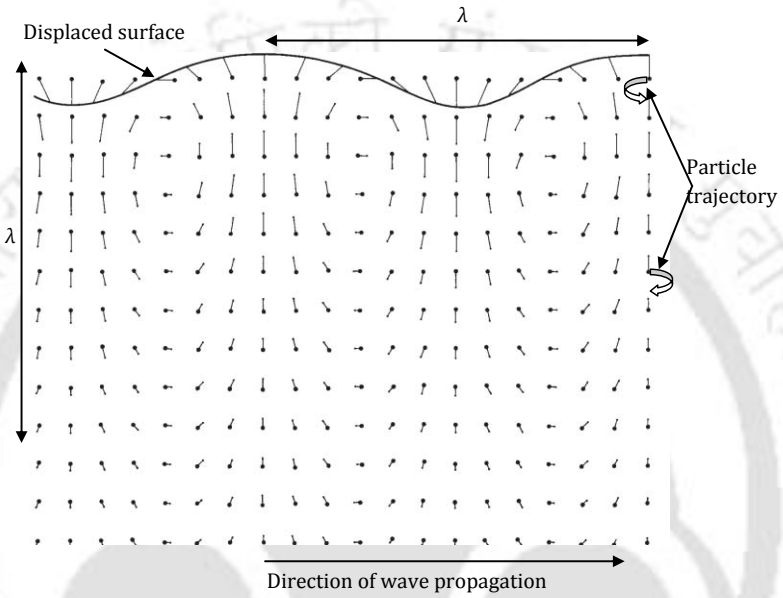

Figure 1. 1. Displacement for Rayleigh wave propagation.

The selection of a different crystal cut can yield a SH surface waves. The particle displacements of this type of wave are transverse to wave propagation direction and parallel to the plane of the surface. The SH-APM are similar to Rayleigh wave, however their substrate thickness is of few wavelengths. The Love waves are SAWs that propagate in a waveguide deposited on a substrate whose thickness is infinite compared the waveguide layer [1]. These waves are transverse and they bring only shear stresses into action.

1.2 Generation of surface acoustic waves

Various types of transducers are reported for generation of SAWs over non-piezoelectric substrate. For example, a wedge shaped longitudinal bulk wave transducer as shown in figure 1.2 (a) generates unidirectional Rayleigh wave. This type of transducer is widely used for non-destructive testing of flaws in non-piezoelectric materials. A shear wave transducer as shown in figure 1.2 (b)

can also be employed to generate Rayleigh waves. The depth of the wave generated is comparable to the width of the transducer. However, an interdigital transducer (IDT) as shown in figure 1.2 (c) and figure 1.2 (d) consisting of comb like metallic electrodes (fingers) fabricated over piezoelectric substrate is a common method to excite and receive surface waves in SAW devices. The IDT performs the function of conversion of electrical energy to mechanical energy, and vice versa. A voltage applied to the finger structure cause spatial periodic fringing field at the substrate, accordingly due to piezoelectric coupling, a strain field is generated. The stress developed with the strain will propagate as SAW in both left and right sides of the transducer. The waves add constructively and reach maximum if the distance between two adjacent fingers is half a SAW wavelength. The frequency of operation of the IDT depends on the period (p) of the IDT, for instance the frequency of operation f for the structure shown in figure 2 (d) is given by

$$f = \frac{V}{\lambda} \tag{1}$$

$$\lambda = 2p \tag{2}$$

where v is the phase velocity of the SAW, which is a constant for a material, λ is the wavelength of

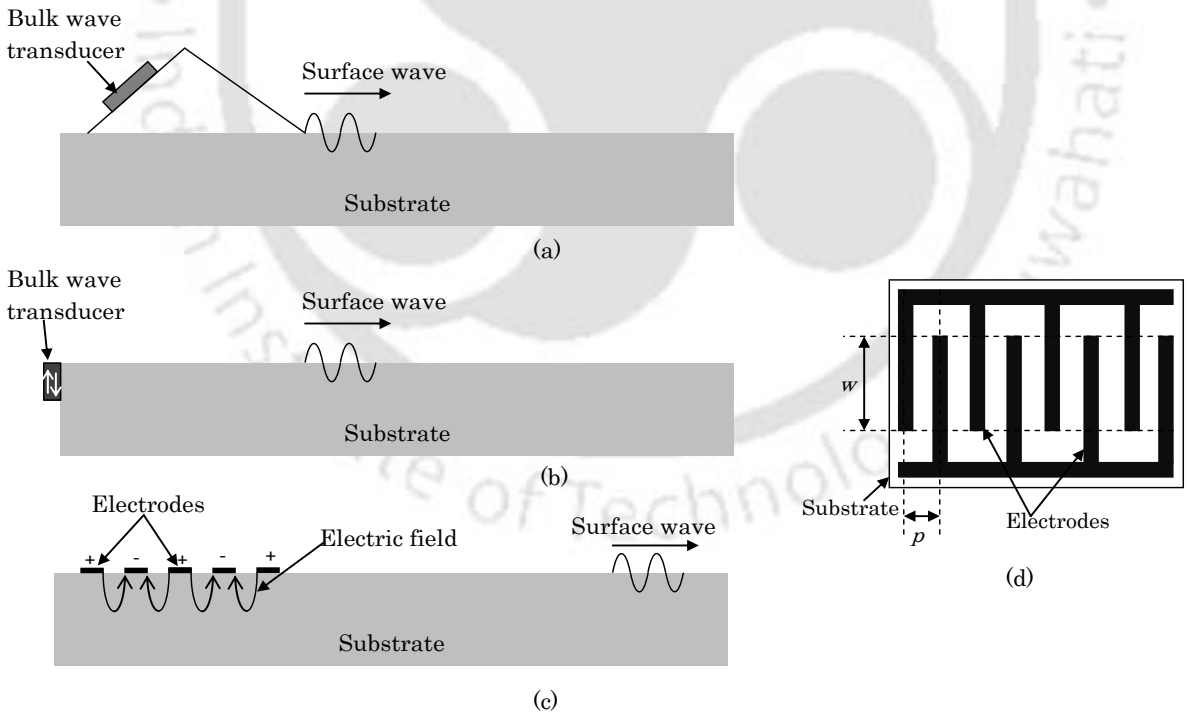

Figure1. 2. Various transducers employed to excite SAW over piezoelectric substrates. (a) Wedge transducer, (b) Edge transducer, (c) interdigital transducer, (d) Top view of (c).

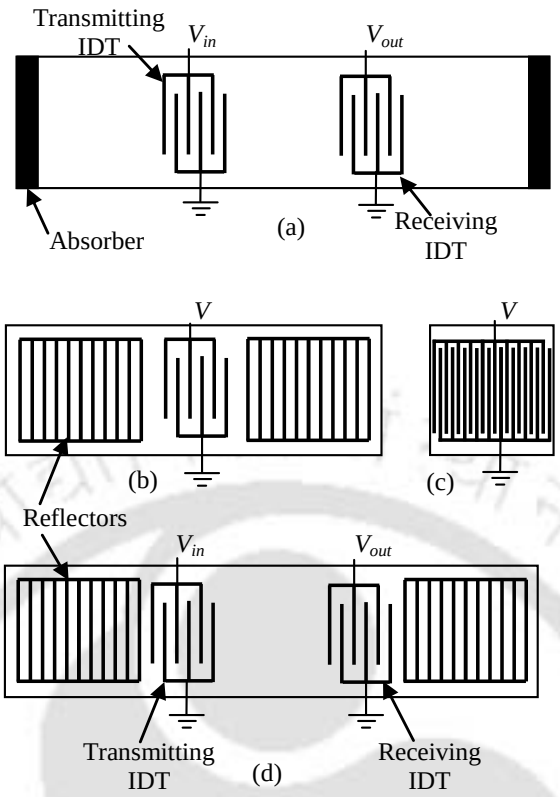

Figure1. 3. (a) SAW delay line, (b) &(c) One-port SAW resonators, (d) Two-port SAW resonator.

the wave, p is the pitch of the IDT. The IDTs can be fabricated on piezoelectric substrate using well established lithography techniques used in semiconductor industry.

1.3 SAW devices

Devices based on SAW are usually developed on piezoelectric substrates such as lithium niobate, lithium tantalate, langasite, and quartz. Non piezoelectric materials such as silicon dioxide and diamond are usually coated with piezoelectric substrates and SAW devices are realized. The two basic configuration of SAW devices are the SAW delay line model and SAW resonator model. A SAW delay line consists of two IDTs on the surface of the substrate separated by a few wavelengths. Figure 1.3 (a) shows the elements of a SAW delay line device. The transmitter IDT excites and receiver IDT detects the SAW over the substrate.

In case of one port resonator, two sets of reflectors are fabricated in the either side of the bidirectional IDT as shown in figure 1.3 (b) [2]. The reflectors could be made of shorted metal strips or grooves. At the Bragg frequency, such that the periodicity of reflector electrodes equals half the wavelength, reflections from individual strips have the same phase so they add coherently, as in a

single electrode of an IDT. Strong reflections are obtained when $N|r_s|>1$, where N is the number of strips and r_s is the reflection coefficient of one strip. Typically, $|r_s|$ is about 2 % and N is 200 or more [2]. One port SAW resonator action can be achieved by single long IDT as shown in figure 1.3 (c), where multiple reflections within the IDT lead to standing waves and resonate in a particular frequency. SAW resonators can be used as a controlling element for a high stability oscillator. For this purpose a two-port SAW resonator can be used as shown in the figure 1.3 (d).

1.4 SAW devices in sensor applications

SAW devices based on various types of acoustic waves such as Rayleigh wave, SH-SAW, Love wave, acoustic plate mode (APM) and flexural plate wave (FPM) have been explored for sensors, actuators and telecommunication applications. The thesis mainly focuses on development of novel SAW

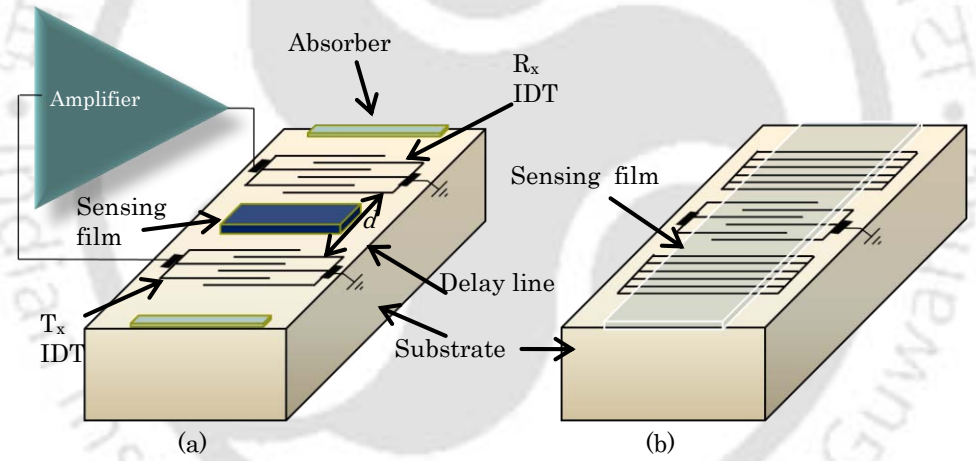

Figure 1.4. (a) A SAW delay line sensor and (b) One port SAW resonator sensor.

sensors. It's worthwhile to mention the operation principle of SAW device used in sensing applications. Scope

Figure1. 4 (a) shows a SAW delay line sensor. It consists of transmitting IDT (T_x IDT) and receiving IDT (R_x IDT) separated by delay line of length d. The delay line is covered by sensing film. Changes in the properties and dimensions of the sensing material caused by a particular measurand introduce perturbations such as change in mass loading, conductivity, permittivity, viscosity, temperature, strain and voltage over the acoustic path and alter the velocity, amplitude and phase of the SAW [3]. Let V_1 and V_2 be the velocity of the SAW that is received in the receiver without and

with measurand input to the sensor respectively. Then $t_1 = d/V_1$ and $t_2 = d/V_2$ are the time taken by the wave to reach the receiver accordingly. If Δt is delay time than one can derive the relation between the changes in phase of the SAW with angular frequency $\omega = 2\pi f$ to the change in velocity (Δv) of the wave due to measurand as given below,

$$\Delta t = t_2 - t_1 = \frac{d}{v_2 - v_1} = \frac{d}{\Delta v} \tag{3}$$

$$\Delta\Phi = \omega \Delta t = \omega \frac{d}{\Delta v} \tag{4}$$

This change in phase ($\Delta\Phi$) of the wave can be measured as change in the oscillator frequency of the delay line oscillator, when the R_x IDT is connected to an RF amplifier in a closed loop as shown in the figure 4(a), the system oscillates at a frequency determined by the wave velocity and the geometry of the electrodes in the IDTs. The output of the amplifier can be measured using a frequency counter.

The other sensor configuration is the resonator type, figure 1. 4 (b) shows an one-port SAW

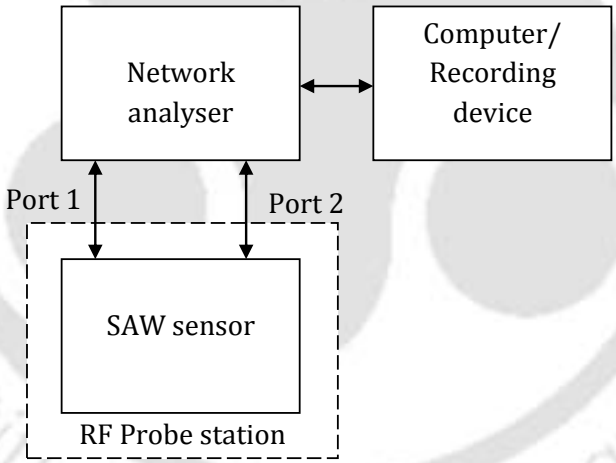

Figure1.5. Setup for measuring SAW sensor characteristics using network analyzer.

resonator, where the sensing film is coated over the entire acoustic path. Thus change in properties of sensing medium will alter the resonance frequency of the SAW resonator. Figure 1. 5 shows a block diagram of a measurement scheme that can be used in measuring the characteristics of SAW sensor. The IDTs can be excited using network analyzer and from the scattering parameters of the device one can characterize the SAW sensor. The measurements of the experimental part of the

thesis are entirely done using network analyzer [1]. A recording device or a computer can be interfaced with the network analyzer to record the outputs.

1.5 Literature reports on SAW sensors

There are several reports in the literature on SAW sensors to detect chemicals, gases, temperature, voltage, liquids, biomolecules, etc. These sensors work on the principles of change in SAW properties due to perturbations in the SAW path caused by the measurand. The thesis focuses on mass loading effect in SAW sensors. There are several reports on SAW sensors working on the principle of mass loading effect. One of the early reports on such sensors is a SAW hydrogen sensor reported by Amico *et al* [4] in 1982. The SAW hydrogen sensor consists of a sensing medium made of thin palladium film coated over its acoustic path. It's reported that in the presence of hydrogen the palladium film material density decreases and Young's modulus increases. Further the volume of the film increases due to the addition of hydrogen molecules to the film [4]. These changes in the sensing film properties introduce mass loading to the SAW device and hence alters the SAW properties and corresponding hydrogen concentration is measured. Table 1 shows a brief list of various SAW sensors reported in last three decades. The table also shows the type of wave, principle of operation, sensing medium used, measurand, and reference.

Table 1.1. List of selected reports of SAW sensors used in various sensing applications

Sl. No	**Type of acoustic wave**	**Principle**	**Sensing medium**	**Measurand**	**Reference and year**
1.	Rayleigh	Strain	No medium	Pressure	Reeder *et al.* [5] 1975
2.	Rayleigh	Mass loading	Dow Corning 970 V vacuum grease, squalane, Apiezon L vacuum grease, di-n-decyl phthalate, and Carbowax 20 M.	Vapour sensor	Wohltjen *et al.* [6] 1979
3.	Rayleigh	Mass loading	Palladium thin film	Hydrogen	Amico *et al.* [4] 1982
4.	Rayleigh	Voltage/Strain	Metal coating	Voltage	Gatti *et al.* [7] 1983

5.	Rayleigh	Conductivity change	Lead Pthalocya-nine film	Nitrogen di oxide	Ricco *et al.* [8] 1985
6	Rayleigh	Mass loading	Platinum thin film	Ammonia	Amico *et al*. [9] 1987
7.	Flexural plate mode (FPM)	Mass loading	Zinc oxide and Silicon nitride films	Vapors of toluene, trichloroethane, and carbon tetrachlonde	Wenzel *et al.* [10] 1989
8.	Rayleigh	Conductivity change	Tungsten oxide film	Hydrogen Sulphide	Falconer *et al.* [11] 1990
9.	Rayleigh	Mass loading	Polymer	Methanol in fuel	J. Reichert *et al.* [12] 1993
10.	Rayleigh	Mass loading	polyisobutylene (PIB) film	CCl_4 Vapors	Pfeifer *et al*. [13] 1994
11.	SH Wave	Conductivity change	Urease enzyme	Urea content in blood	Kondoh *et al.* [14] 1994
12.	Rayleigh	Conductivity change	Copper Pthalocyanine	NO_2	Beck *et al*. [15] 1999
13.	SH– wave	Mass loading	Antibody	Biochemical's	Josse *et al.* [16] 2001
14.	Rayleigh	Mass loading	Antibody	Uranine vapor, Alexa vapor (Electronic nose)	Stubbs *et al.* [17] 2002
15.	SH - wave	Conductivity change Viscosity change	No medium	Milk, Orange juices, and water (Smart Tongue)	Cole *et al* [18] 2004
16.	Rayleigh	Voltage/Strain	No medium	Strain/Pressure	Jiang *et al.* [19] 2005

17.	Rayleigh	Mass loading/Conductivity	Chemical warfare agents	Various polymers	Joo *et al.* [20] 2007
18.	Rayleigh	Mass loading and conductivity change	Graphene sheet	CO and H_2	Arsat *et al.* [21] 2009

1.6 Problem definition

Designing SAW sensors based on mass loading principle involves design of SAW transducers and suitable sensing medium. There are number of reports on sensing film made of thin film or nanostructures. However, uses of resonant structures in sensing medium for SAW sensors are not reported. In this thesis design of novel class of SAW sensor using resonant structure as sensing medium is reported. SAW device and the resonant structure attached to it form a system of coupled resonator. The coupled resonance is well known in early piezoelectric devices and their characteristics are defined by Dybwad model [22]. Recently similar system of coupled resonance using quartz crystal micro (QCM) balance has been reported by pomorska *et al*. [23]. Finite element method (FEM) simulation and experiments on the proposed novel design of SAW devices are performed to analyze the mass loading effect and feasibility use of resonant structures in SAW devices.

1.7 Scope of the thesis

The thesis aim in studying the mass loading effect of resonant structures such as a high aspect ratio pillars fabricated on SAW devices and their possible use in sensor applications. The various scope of the thesis is as follows,

- Methodologies to model and perform simulation of SAW resonator, SAW delay line device, and mass sensitivity analysis using finite element method
- Study of mass loading characteristics of high aspect ratio structures attached to the surface of SAW devices

- Methodology to fabricate SAW devices, SAW devices with resonant structures
- Investigation on mass loading effect of resonant structures to design novel class of SAW devices suitable for sensing applications

1.8 Thesis outline

In the initial part of the chapter 2, we introduce Rayleigh waves, surface waves with piezoelectric effects, and various modeling and simulation techniques for SAW devices such as the circuit model, Coupling of mode (COM) model, and finite element simulation (FEM) of SAW devices using COMSOL Multiphysics (commercial FEM software). In the later part of the chapter the FEM simulation and results of one port SAW resonator, SAW delay line configuration, mass sensitivity analysis of a SAW delay configuration, and SAW hydrogen sensor are reported. A new simplified FEM simulation methodology is employed using COMSOL Multiphysics for solving time domain response of SAW delay line devices.

In chapter 3, initially mass loading effect of thin film in SAW devices is discussed. FEM simulation of mass loading effect of high aspect ratio structures on SAW resonators is discussed. Simulation setup, results and discussion of the study are reported. Results of FEM simulation of SAW hydrogen sensor with resonant structure made up of palladium metal are described and discussion on increase in sensitivity compared to a palladium thin film is reported. Experiment on mass loading of thin film made of *N*-isopropylacrylamide (NIPAAm) nanogel and its potential in development of SAW humidity sensor are discussed.

In chapter 4, fabrication of SAW devices, fabrication of resonant structures made of SU-8 on SAW devices, various issues in fabrication on a complete 4 inch wafer in fabrication, design aspects of SAW transducers and resonant structures, various fabrication trails performed to optimize the process flow are discussed in this chapter. The experimental setup, measurement techniques and results on SAW humidity sensor are also discussed in the chapter.

In chapter 5, measurement and calculation of resonance frequencies of fabricated SAW resonators and of SAW resonators with SU-8 resonant structures are elaborated. Analysis on resonance frequency for different dimensions of resonant structures is presented. Validation of experimental results with FEM simulation of the SAW resonator with SU-8 resonant pillar structure is described in the chapter. Increase in resonance frequency of SAW resonator caused by mass loading of SU-8 resonant pillars is analyzed and discussions on contact stiffness, relating to the increase in

resonance frequency of the SAW coupled resonator are presented in the chapter. Mass loading characteristics of a system of coupled resonator is discussed with help of Dybwad model and results on identifying zero mass loading condition due to resonant structures is discussed in this chapter.

In chapter 6, List of conclusion of the research work and recommendation for future work in designing SAW sensors with resonant structures are given.

2

Modeling and Simulation of SAW Devices

SAW devices can be modeled using various techniques such as the delta function model, equivalent circuit model, coupling of mode (COM) method, and can be simulated using techniques such as the finite element method (FEM). In this chapter FEM simulation of SAW devices such as SAW resonator, SAW delay line devices and SAW device model to study mass loading effect are discussed.

Early researchers rely on experiments to design and develop SAW devices. There were frequent discrepancies in actual function of devices. Basic design of SAW transducers has to be optimized with the help of modeling techniques. Nowadays computer aided simulation helps in designing SAW devices and studying the characteristics of these devices made on new piezoelectric substrates. Simulations of SAW devices help in estimating and visualizing the SAW device response before fabricating these devices.

2.1 The equivalent circuit model

The mason equivalent circuit is well documented by smith *et al*. [24]. The response of the SAW device can be represented as an equivalent circuit model consisting of three ports, viz. two acoustic and one electric port as shown in figure 2.1[24]. The electrical equivalent of the two acoustic ports is represented as a SAW transmission line and voltages are applied and sensed at the third electrical port. Figure 2.1 shows equivalent circuit of a single pair of electrode in an IDT. $\theta = 2\pi f/f_0$ (where f is the frequency of the input potential and f_0 is the resonance frequency of the IDT) is the periodic section transit angle, R_0 is the electrical equivalent to Z_0, acoustic impedance given by

$$R_0 = \frac{Z_0}{\varphi^2} \tag{5}$$

where $\varphi = \varsigma C_s/2$ is the turns ratio of an acoustic-to-electric circuit transformer. C_s is the static electrode capacitance of one periodic section, which can be found out theoretically or experimentally, ς is a piezoelectric constant. If F_n is acoustic terminal force and u_n' is the particle velocity, then their electric equivalent: electric potential (E_n) and current (i_n) is $E_n = F_n/\phi$ and $i_n = u_n'\varphi$ respectively. The entire IDT can be realized by placing the equivalent circuit of a single pair in cascade. In this model, the acoustic forces are converted into electrical voltages and SAW velocities are converted into equivalent electric currents. These transformations allow the mechanical characteristic admittance (similar to the transmission line characteristic impedance which is expressed in ohms) to be expressed as an equivalent transmission line characteristic admittance in mho as,

$$G_0 = \frac{1}{R_0} = \frac{\omega C_s k^2}{2\pi} \tag{6}$$

where, k is the electro-mechanical coupling coefficient, the k^2 values can be approximated by $-2\Delta v/v$, where Δv is the change in wave velocity when the piezoelectric surface is electrically shorted by a thin metal film and it can be theoretically determined. The values of k^2 for typical substrates are given in Appendix A.

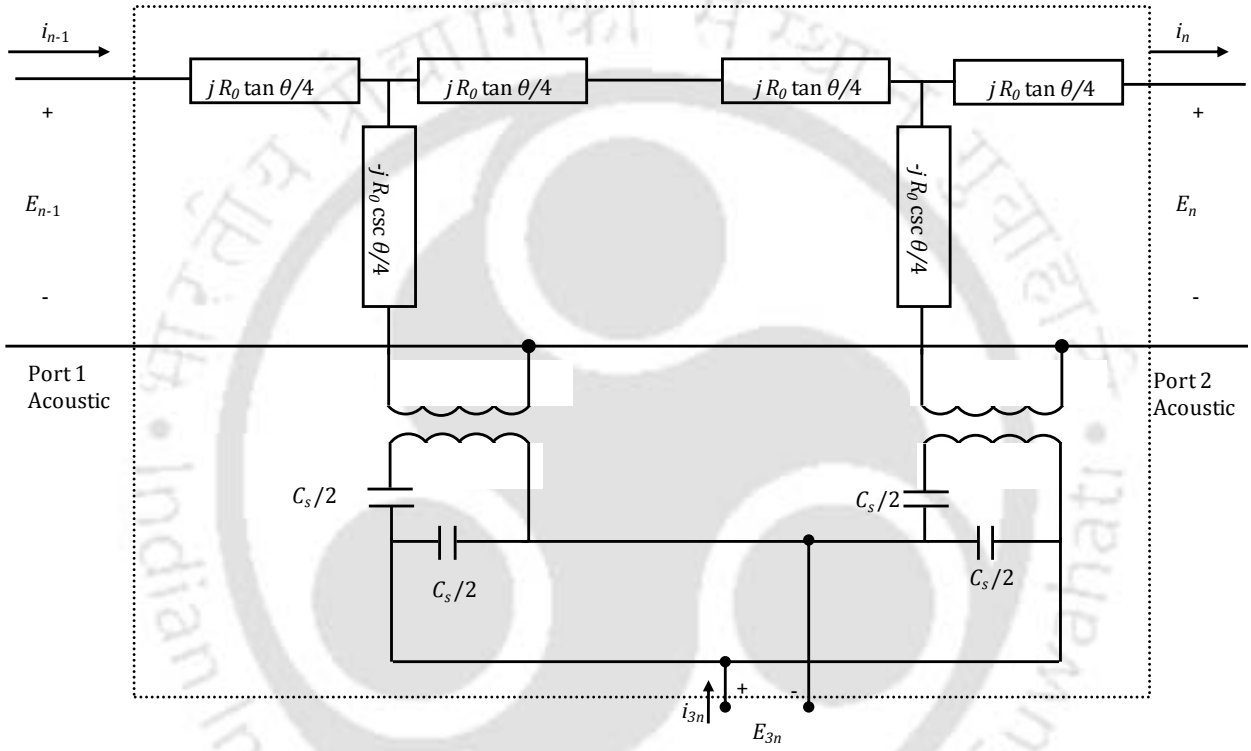

Figure 2.1. Mason equivalent circuit used by Smith *et al.* [24]for SAW equivalent circuit model where θ is periodic section transit angle, R_0 is electrical equivalent of mechanical impedence, C_s is electrode capacitance per electrode (Static), j is the imaginary unit, E_n is equivalent electric potential, and I_n is equivalent electric current.

For a SAW device consisting of a generator IDT and a receiver IDT that are completely matched, the Y parameters of the 3-port network using the equivalent circuit for a pair of electrodes in an IDT can be written as matrix equation is given by smith *et al* [24] as

$$\begin{bmatrix} i_1 \\ i_2 \\ i_3 \end{bmatrix} = \begin{bmatrix} -jG_0 \cot N\theta & jG_0 \csc N\theta & -jG_0 \tan\left(\frac{\theta}{4}\right) \\ jG_0 \csc N\theta & -jG_0 \cot N\theta & jG_0 \tan\left(\frac{\theta}{4}\right) \\ -jG_0 \tan\left(\frac{\theta}{4}\right) & jG_0 \tan\left(\frac{\theta}{4}\right) & j\omega C_T + jG_0 \tan\left(\frac{\theta}{4}\right) \end{bmatrix} \times \begin{bmatrix} E_1 \\ E_2 \\ E_3 \end{bmatrix} \quad (7)$$

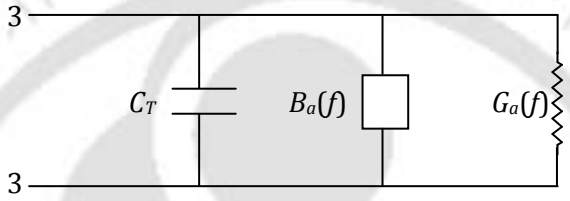

Figure 2. 2. Overall equivalent circuit of an IDT.

where, $C_T = NC_s$ (total capacitance of IDT), N being the number of electrode pairs. The overall equivalent circuit of a SAW IDT is shown in figure 2.2 [23]. The input admittance for this circuit is given as

$$Y_3(f) = G_a(f) + B_a(f) + j\omega C_T \quad (8)$$

$G_a(f)$ and $B_a(f)$ are defined as the radiation conductance and susceptance, respectively.

$$G_a(f) \approx 8N^2 G_0 \left| \frac{\sin X}{X} \right|^2 \quad (9)$$

$$B_a(f) = 8N^2 G_0 \left| \frac{\sin(2X) - 2X}{2X^2} \right|^2 \quad (10)$$

where $X = N\pi(f - f_0)/f_0$. The radiation susceptance is a reactive parameter that goes to zero at the centre frequency. This term is often omitted in calculations near the centre frequency because it is negligible compared to the total IDT capacitance term. Researchers have also involved in simulating and improving the equivalent circuit of IDT. Bhattacharyya *et al.* [25] has simulated IDT with other

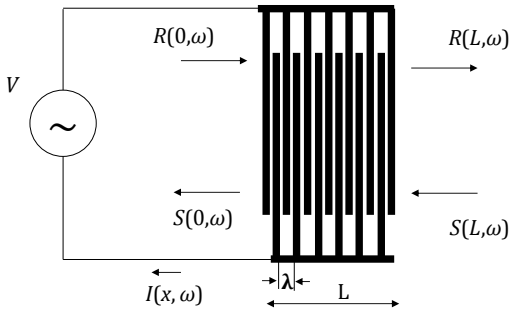

Figure 2. 3. Coordinates of an IDT [27].

external circuits using SPICE software. Munshi *et al*. [26] has improved the equivalent circuit of an IDT by including the effects of metal shorting and energy storage at metal discontinues, as well as an arbitrary polarity sequence of fingers.

2.2 Coupling of mode model

COM model is widely used in designing SAW devices [27]. To present the COM model in this chapter, the determination of COM parameters reported by Wu *et al*. [28] will be briefly described in this section. Figure 2.3 shows the coordinates of IDT of length *L*. The COM model comprises of differential equations governing SAW mode amplitudes $R(x,\omega)$, $S(x,\omega)$ in either side of IDT and the current due to the flow of charges $I(x,\omega)$(see figure 2.3).

$$\begin{aligned}
\frac{dR(x)}{dx} &= -jk_E R(x) + jK_R e^{-j2k_0 x} S(x) + j\alpha_R V e^{-jk_0 x} \\
\frac{dS(x)}{dx} &= -jk_E S(x) + jK_s e^{+j2k_0 x} R(x) - j\alpha_S V e^{+jk_0 x} \\
\frac{dI(x)}{dx} &= +j2\alpha_S R(x) e^{+j2k_0 x} + j2\alpha_R S(x) e^{-jk_0 x} - j\left(\frac{3\omega C_F/\lambda}{3+j\omega R_F C_F}\right)_S V
\end{aligned} \tag{11}$$

where V is the voltage across the IDT, $k_0=2\pi/\lambda$ is transducer synchronous wave number, and

$$K_E = +\frac{\omega}{v} - \left(\frac{2\alpha_R^2 \omega R_f^2 C_f^{\,2}\lambda}{9+(\omega R_f C_f)^2}\right) - j\left[\gamma + \left(\frac{6\alpha^2 R_f \lambda}{9+(\omega R_f C_f)^2}\right)\right]$$

$$\alpha_R = \frac{3\alpha e^{-j\pi}}{3+j\omega C_f R_f}$$

$$\alpha_S = \frac{3\alpha e^{j\pi}}{3+j\omega C_f R_f}$$

$$K_R = +K_i e^{j\pi/2} + \frac{2j\alpha^2 R_f \lambda e^{-2j\pi}}{3+j\omega C_f R_f}$$

$$K_S = +K_i e^{-j\pi/2} + \frac{2j\alpha^2 R_f \lambda e^{2j\pi}}{3+j\omega C_f R_f}$$

In the above equations ϕ_b and ϕ_t are phase offsets of the grating and the potential respectively and angular frequency $\omega = 2\pi f$. The COM parameters are as follows. v the phase velocity of the SAW, α the transduction coefficient, R_f the thin film resistance in one transduction unit, C_f interdigital capacitance in one transduction period, K is the reflection parameter, γ propogation loss per unit length. The suffix R and S represents the value for the corresponding direction of wave propagation (see figure 2.3). These parameters can be computed through computer simulation such as FEM or experimental analysis of a test structure. The COM equations can be represented in the P matrix form. The acoustic ports are treated as scattering port and electric port as admittance port as

$$\begin{bmatrix} S(0) \\ R(L) \\ I \end{bmatrix} = \begin{bmatrix} P_{11} & P_{12} & P_{13} \\ P_{21} & P_{22} & P_{23} \\ P_{31} & P_{32} & P_{33} \end{bmatrix} \begin{bmatrix} R(0) \\ S(L) \\ V \end{bmatrix} \tag{12}$$

where

$$P_{11} = \frac{+jK_S \sin(DL)}{D\cos(DL) + j\Delta\sin(DL)}$$

$$P_{12} = \frac{D}{D\cos(DL) + j\Delta\sin(DL)} e^{-jK_0 L}$$

$$P_{13} = P_{31} + jL\frac{\sin(DL/2)}{DL/2} \times \frac{\alpha_s D\cos(DL/2) + j(K_S\alpha_R + \Delta\alpha_s)\sin(DL/2)}{D\cos(DL) + j\Delta\sin(DL)}$$

$$P_{22} = \frac{+jK_R \sin(DL)}{D\cos(DL) + j\Delta\sin(DL)} e^{-j2K_0 L}$$

$$P_{23} = P_{32} + jL\frac{\sin(DL/2)}{DL/2} \times \frac{\alpha_R D\cos(DL/2) + j(K_R\alpha_S + \Delta\alpha_R)\sin(DL/2)}{D\cos(DL) + j\Delta\sin(DL)}$$

$$P_{33} = +j2\left(\frac{K_S\alpha_R^2 + K_R\alpha_S^2 + 2\Delta\alpha_R\alpha_S}{D^3}\right) \times DL - \frac{D\sin(DL) + j\Delta(1-\cos(DL))}{D\cos(DL) + j\Delta\sin(DL)}$$

$$-2\left(\frac{K_S\alpha_R^2 + K_R\alpha_S^2 + 2\Delta\alpha_R\alpha_S}{D^3}\right) \times \left(\frac{1-\cos(DL)}{D\cos(DL) + j\Delta\sin(DL)}\right) \times j\left(\frac{3\omega C_f L/\lambda}{3 + j\omega R_f C_f}\right)$$

$$\Delta = K_E - K_0$$

$$D = \sqrt{\Delta^2 - K_R K_S}$$

P_{11} and P_{22} are the reflection coefficients, P_{12} and P_{21} are the transmission coefficient. The remaining terms P_{13} and P_{23} correspond to the excitation coefficient of the IDT and the term P_{33} clearly represents the admittance of the structure relating the current in the electrode (i) and the drive voltage (V). P_{31} and P_{32} terms represent the current generated by the waves arriving at the acoustic ports. Admittance or P_{33} can be calculated from simulations and is the most useful in device design.

The admittance component P_{33} consists of two parts namely, homogeneous solution part and particular solution part.

2.3 Solution of surface wave

Before briefing about the finite element method (FEM) model for a SAW device, the basics of piezoelectricity and differential equations governing SAW propagation, boundary conditions and solutions to the differential equations will be discussed.

Many different types of waves can propagate in solids as described in section 1.1 of chapter 1. The work in this thesis is mainly related to the surface waves. It is important to study the nature of the waves and piezoelectric theory to understand the SAW devices. In this thesis, the term 'SAW' without further qualification is taken to mean Rayleigh waves in piezoelectric substrates.

2.3.1 Elasticity in piezoelectric materials

As introduced in chapter 1, SAW devices make crucial use of piezoelectricity, it is necessary to take account of it in the analysis. The elasticity in piezoelectric materials is explained in [29],[30],[31] and,[2]. In a piezoelectric solid the interdependence of electric and mechanical variables implies a coupling between the elastic and electromagnetic waves [30]. Theoretically, the field distribution can be found by solving simultaneously the equations of both Newton and Maxwell. In case of elastic waves in piezoelectric crystals, the velocity of the elastic waves is much smaller than the electromagnetic waves. Hence the magnetic field due to these waves is negligible. Thus Maxwell equation can be approximated as

$$\operatorname{curl} E = -\frac{\partial \mathbf{B}}{\partial t} \simeq 0 \text{ giving } \mathbf{E} = -\operatorname{grad} V \tag{13}$$

where **B** is the magnetic field, **E** is the electric field derived from the scalar electric potential V. Elasticity in solids is concerned with internal forces within the solid and related displacement of the solid from its equilibrium. The forces are expressed in terms of stress **T** and displacements in terms of strain S. A 'particle' is referred to a smaller elementary region than characteristic elastic dimension such as wavelength, but larger compared to inter-atomic distance. For example as shown in figure 2.4 a particle situated at point $\mathbf{x} = (x_1, x_2, x_3)$ is displaced by an amount $\mathbf{u} = (u_1, u_2, u_3)$, where u_1, u_2, and u_3 are displacement values of the particles along x_1, x_2, and x_3, coordinates respectively. Thus in the example the particle from the equilibrium position **x** has been displaced to a new position **x**+**u**. The strain at each point can be expressed as

$$S_{ij}(x_1, x_2, x_3) = \frac{1}{2}\left(\frac{\partial u_i}{\partial x_j} + \frac{\partial u_j}{\partial x_i}\right) \quad i, j = 1, 2, 3 \tag{14}$$

The displacements or rotation as a whole of the material does not contribute to strain, further strain is a second-rank tensor and is clearly symmetrical, so that $S_{ij} = S_{ji}$

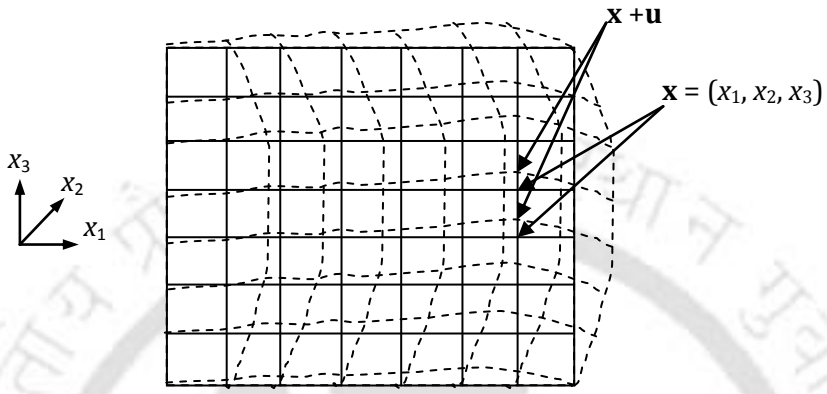

Figure 2.4. Particle position in equilibrium and deformed states of solid body.
The deformation of the solid is shown in dotted lines.

Similarly the stresses can be represented as a second rank tensor T_{ij} (x_1, x_2, x_3). According to Hooke's law, the stress components are linear combination of strain components .The coefficients needed are given by stiffness tensor C^E_{ijkl} or the elasticity matrix, accordingly the stress due to the mechanical strain or $T_{ij(mech)}$ is given by

$$T_{ij(mech)} = \sum_k \sum_l C^E_{ijkl} S_{kl}, \quad i, j, k, l = 1, 2, 3 \tag{15}$$

On the other hand the stress, $T_{ij(elec)}$ produced by the piezoelectric effect,

$E_k = -\frac{\partial V}{\partial x_k}$ is given by

$$T_{ij(elec)} = \sum_k e_{kij} E_k, \quad i, j, k = 1, 2, 3 \tag{16}$$

The total stress T_{ij} is sum of stresses due to the electric field and mechanical strain and is given by

$$\begin{aligned} T_{ij} &= \sum_k \sum_l C^E_{ijkl} S_{kl} - \sum_k e_{kij} E_k \\ &= \sum_k \sum_l C^E_{ijkl} S_{kl} + \sum_k e_{kij} \frac{\partial V}{\partial x_k} \end{aligned} \tag{17}$$

Substituting (14) in (17) result in

$$T_{ij} = \sum_k C_{ijkl}^E \frac{\partial^2 u_k}{\partial x_k} + \sum_k e_{kij} \frac{\partial V}{\partial x_k} \tag{18}$$

when an electric field **E** is applied between two plates separated by a dielectric medium of permittivity ε, the electric field displacement **D** is ε ·**E**. In case of piezoelectric material due to the piezoelectric effect, there is additional electric field displacement caused by the strain developed on application of potential. The total D_i is given by

$$D_i = \sum_j \varepsilon_{ij}^s . E_j + \sum_j \sum_k e_{ijk} . S_{jk} \tag{19}$$

Where e_{ijk} is the piezoelectric tensor, ε_{ij}^s is the permittivity matrix, **E** is the electric field vector, S_{ij} is the strain vector, **D** is the electrical displacement. For an elementary cube of length δ inside the piezoelectric material of density ρ, the mass is $\rho\delta^3$. The total force in terms of stress along x_i direction is given by

$$\delta^3 \left[\sum_k \frac{\partial T_{ij}}{\partial x_j} \right], \; i, \text{j} = 1, 2, 3 \tag{20}$$

Hence Newton's law of motion can be expressed as,

$$\rho \frac{\partial^2 u_i}{\partial t^2} = \left[\sum_k \frac{\partial T_{ij}}{\partial x_j} \right], \; i, j, k = 1, 2, 3 \tag{21}$$

Substituting (18) in (21) the equation of motion becomes,

$$\rho \frac{\partial^2 u_i}{\partial t^2} = \sum_j \sum_k \left\{ e_{kij} \frac{\partial^2 V}{\partial x_j \partial x_k} + \sum_l C_{ijkl}^E \frac{\partial^2 u_k}{\partial x_j \partial x_l} \right\} \tag{22}$$

As there are no free charges, since the material is taken to be as an insulator, hence div **D** = 0 thus (19) can be written as

$$\sum_i \sum_j \left\{ \varepsilon_{ij}^S \frac{\partial^2 V}{\partial x_i \partial x_j} - \sum_k e_{ijk} \frac{\partial^2 u_j}{\partial x_i \partial x_k} \right\} = 0 \tag{23}$$

for i, j, k, l = 1, 2 and 3.

The degrees of freedom (dependent variables) are the global displacements u_1, u_2, and u_3 in the global x_1, x_2, and x_3 directions, respectively and the electric potential *V,* can be obtained by solving the equations given in 22 and 23.

2.3.2. The solution of surface wave in piezoelectric media

The detailed procedure for finding the solution of surface waves in isotropic and anisotropic materials is explained in [2]. In this section, boundary conditions and solutions of surface waves are briefly elaborated. In case of piezoelectric crystal the care has to be taken in specifying the orientation of the material. For crystalline material the uppercase X, Y, and Z denotes the set of axes with directions defined by convention to the crystal lattice. For example in case of Y cut Z propagating lithium niobate (Y-Z $LiNbO_3$) material x_3 is parallel to crystal *Y* axis and x_1 is parallel to crystal *Z* axis. The orientation of x_3 is also referred to as cut, so that for *Y-Z* $LiNbO_3$ the crystal is *Y* cut. The material tensors – the stiffness, permittivity and piezoelectric tensors – are specified in relation to the X, Y, and Z axes. The literature normally provides *X-Y* material tensors. So for analysis they must first to be rotated into the frame defined by x_1, x_2 and x_3 using tensor transformations. The algorithms to perform these transformations are well documented in [30] and can also be found in the appendix B of this thesis.

The boundary conditions at the surface should be satisfied in order to determine the phase, velocity and amplitude of the waves. In case of piezoelectric materials the following mechanical and electrical boundary conditions are to be satisfied simultaneously. The mechanical boundary conditions at the surface of the substrate is stress-free condition as expressed in equation below

$$T_{13} = T_{23} = T_{33} = 0 \text{ at } x_3 = 0 \tag{24}$$

The electrical boundary is imposed by Maxwell's equation, the normal component of **D** being continuous across the air/substrate interface (at $x_3 = 0$). To find the surface wave solutions, we first consider the partial waves in which the displacements and potential, denoted by **u'** and V'**,** take the form

$$\mathbf{u}' = \mathbf{u}'_0 \exp(j\tau x_3) \exp[j(\omega t - K_0 x_1)], \tag{25}$$

$$V' = V'_0 \exp(j\tau x_3) \exp[j(\omega t - K_0 x_1)] \tag{26}$$

where K_0 is the wavenumber of the surface wave, assumed to be real. These expressions are substituted to equation (22) and (23). Then these equations are solved for τ numerically, giving

eight solutions for the same. Accordingly for every solution of τ, relative solutions of $\mathbf{u}'$ and V' are obtained. There are four values of τ in general denoted by τ_1, τ_2 τ_3 ,and τ_4. The partial waves are therefore,

$$\mathbf{u}_i' = \mathbf{u}_{0i}' \exp(j\tau_i x_3)\exp[j(\omega t - K_0 x_1)], \tag{27}$$

$$V_i' = V_{0i}' \exp(j\tau_i x_3)\exp[j(\omega t - K_0 x_1)], \quad i = 1,2,3,4 \tag{28}$$

In the half-space it is assumed that the solutions is a linear sum of these partial waves, so that

$$\mathbf{u} = \sum_{i=1}^{4} A_i \mathbf{u}_i' \tag{29}$$

$$V = \sum_{i=1}^{4} A_i V_i' \tag{30}$$

The coefficients A_i are to be such that the solution satisfies the electrical and mechanical boundary conditions. These conditions give a determinant which must be zero for a valid solution for a right choice of K_0. The velocity than can be determined by ω/K_0 and displacement and potential are given by equation (29) and (30).

2.4. Finite element method (FEM)

The FEM is used almost in every discipline of engineering particularly in the areas of stress/strain analysis of solid structures, heat conduction analysis, and fluid dynamics. Only some basic procedures and techniques used in finite element formulations will be presented here and a detailed theory can be found in [31] and [32].

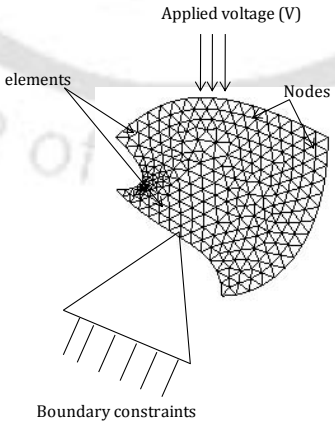

Figure 2.5. Illustration showing a solid body discretized into finite number of elements

2.4.1. Input and output information in FEM

In the finite element method, following input information about the structure and material are to be provided,

1. Profile of the structure geometry

2. Coordinates systems according to the geometry in 3D or 2D

4. Properties of the materials used in the model for instance for a piezoelectric material, elasticity matrix, piezoelectric constant, permittivity constant, density are to be furnished and for an isotropic properties such as Young's modulus, density, Poisson ratio, etc. are to be provided.

4. Boundary conditions to the boundaries of the structure are to be provided. For example in case of stress/strain analysis for piezoelectric material the boundary conditions can be displacement constraints and electric boundary conditions such as electric potential, electric displacement, charge etc.

Further the problem domain is to be discretized into smaller regions called elements which are connected at specific points called nodes as shown in the figure 2.5.The elements created may be two or three dimensional and can have triangular, quadrilateral, tetrahedral or brick shapes depending on the dimensionality. The output information in case of stress/strain analysis in piezoelectric material involves nodal and elemental information, the solution to the primary unknown quantities, the displacements in all directions and the voltage are determined at nodes and these unknowns are known as degrees of freedom (DOF).

2.4.2. Finite element formulation

This process begins with subdividing a continuum into an assembly of elements interconnected at nodes as shown in the figure 2.5. It can be seen that after discretization, the original curved boundaries are approximated by straight edges of the elements of the boundary. The primary unknown quantities for the case of stress/strain analysis of piezoelectric material are the displacement $\{\mathbf{u}(\mathbf{r},t)\}$ and voltage $\{V(\mathbf{r},t)\}$ where t denotes time, $\mathbf{r}$ indicates position vector that defines the elements. These position vector represents the spatial coordinates (x_1, x_2, x_3) or cylindrical polar coordinates ($\mathbf{r}$,z) for an axis symmetric solid. The continuity of the solution (since solutions are determined at specific points, the nodes) is taken care of by introduction of shape functions or interpolation functions. The choice of these functions determines or approximates how the field varies across a single element domain. Normally, a polynomial function is chosen as a shape function and the number of nodes assigned to a particular element defines the order of the polynomial. Thus the mathematical expression for discritization can be written as

$$\{\mathbf{u}(\mathbf{r},t)\} = [N(\mathbf{r})]\{u\} \tag{31}$$

where [N(**r**)] is the interpolation function and the vector {**u**} is the corresponding nodal displacement components. The values of primary unknown quantities at the nodes of an element can be related to the applied nodal loads as $\{K_e\}$ $\{u\}$ = $\{Q_e\}$ where, $\{K_e\}$ is the element coefficient matrix, $\{Q_e\}$ is the applied load, in case of stress/strain analysis of piezoelectric material the applied loads are force and applied electric potential. A system of equations in terms of unknown nodal values is formulated for that element and subsequently for the whole domain. This system of equations can be solved by appropriate numerical techniques. In this thesis work numerical techniques used in commercial FEM software COMSOL Multiphysics are utilized for solving the system of equations. These techniques are not the focus of this research and will not be discussed in this thesis. All finite element method (FEM) analysis of SAW devices in this thesis are carried out using piezoelectric module and the PDE module of COMSOL Multiphysics software. The software has well developed solvers, graphical user interface (GUI), and post-processing capabilities. More details of the software can be inferred from the user guide of the software [33].

2.4.3. Finite element simulation of SAW devices

FEM simulations of similar devices have been reported by the following researchers. Lerch *et al*. [34] presented an FEM scheme to calculate eigen modes, and dynamic response to mechanical and electrical excitations of 2D and 3D piezoelectric transducer of any geometry. Rahman *et al*. [35] performed FEM simulation to study SAW based quantum devices. Atashbar *et al.* [36] simulated mass loading effect of palladium sensing film in the presence of hydrogen. Wu *et al.* [37] used Taguchi method on FEM results and established robust design processes for SAW sensors based on the mass loading principle. Ippolito *et al*. [38] performed FEM analysis of acoustic waves propagating on layered SAW devices. Wang *et al*. [39] carried out FEM study of the effect of change in film properties on the mass sensitivity of SAW sensors. Xu [40] has reported FEM simulation of a SAW filter. Subraminian *et al*. [41] used FEM simulation to design SAW device suitable in remotely readable microaccelerometers. In most of the earlier work the number of DOF to solve is more due to the large size of the SAW structures considered in the model. In order to solve DOF for an entire SAW device requires high computing facility and consumes time in computation. Thus valid approximation and simplified model is required to perform FEM simulation of SAW devices.

2.5. FEM Simulation of One-Port SAW resonator using COMSOL Multiphysics

One-port resonator action can be achieved by multiple reflections between the fingers of a long IDT or reflections by the reflectors at the either side of a short IDT [2]. The geometry of the segment

(figure 2.6) considered for the simulation is chosen to simulate a 100 MHz SAW resonator. Its dimensions are as follows: electrode width 34.88 μm, pitch (p) 69.76 μm, height of the substrate 174.4 μm, and thickness in x_2 direction (aperture) 10 μm, 20 μm and 30 μm. The constants used in the simulation are given in the appendix. The bottom surface is fixed. 3D simulations are performed with plane strain conditions. It is possible by modeling a thin strip of thickness of w in x_2 direction, cut out from the SAW device, and applying zero displacement constraint in the x_2 direction on the boundaries Γ_1 and Γ_2 (see figure 2.6). It is valid in the case of Rayleigh SAW as it has no variation and the displacement vectors have no component in x_2 direction [1]. The degrees of freedom of the right periodic boundary (Γ_R) are set to be negative of those from the left periodic boundary (Γ_L) [42] (see figure. 2. 6). In general the periodic boundary expression for SAW resonator model can be written as (8). Lithium niobate piezoelectric crystal is used as the substrate. The elastic constants, permittivity constants, stress constants are taken from [43] and Y cut Z propagating constants are provide as in appendix C.

$$\Gamma_R(u_i, V) = \eta\, \Gamma_L(u_i, V) \tag{32}$$

where $\eta = (-1)^n$, u_i is the displacement, V is the potential. A potential of 10 V is applied to the electrodes in the simulation. Eigen frequency response analysis is performed to find the resonance frequency of the SAW resonator. Figure 2.4 (a) and figure 2.4 (b) shows the total displacement of the SAW resonator at resonance frequency of 97.4 MHz and anti resonance frequency of 98.5 MHz respectively. The resonance frequency is identified from the list of eigen frequencies and their displacement amplitude and mode of vibration. At resonance frequency the displacement is maximum at the edge of the resonator while for the anti-resonance frequency the displacement is

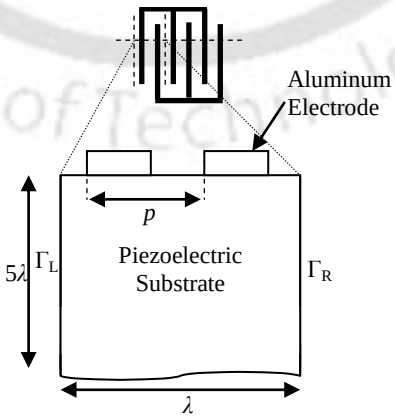

Figure 2.6. Geometry employed in the one port SAW resonator simulation.

maximum at the middle of the finger. Figure 2.4(c) and figure 2.4(d) shows the x_1 and x_2 displacements respectively, the arrows indicate the direction of particle displacement.

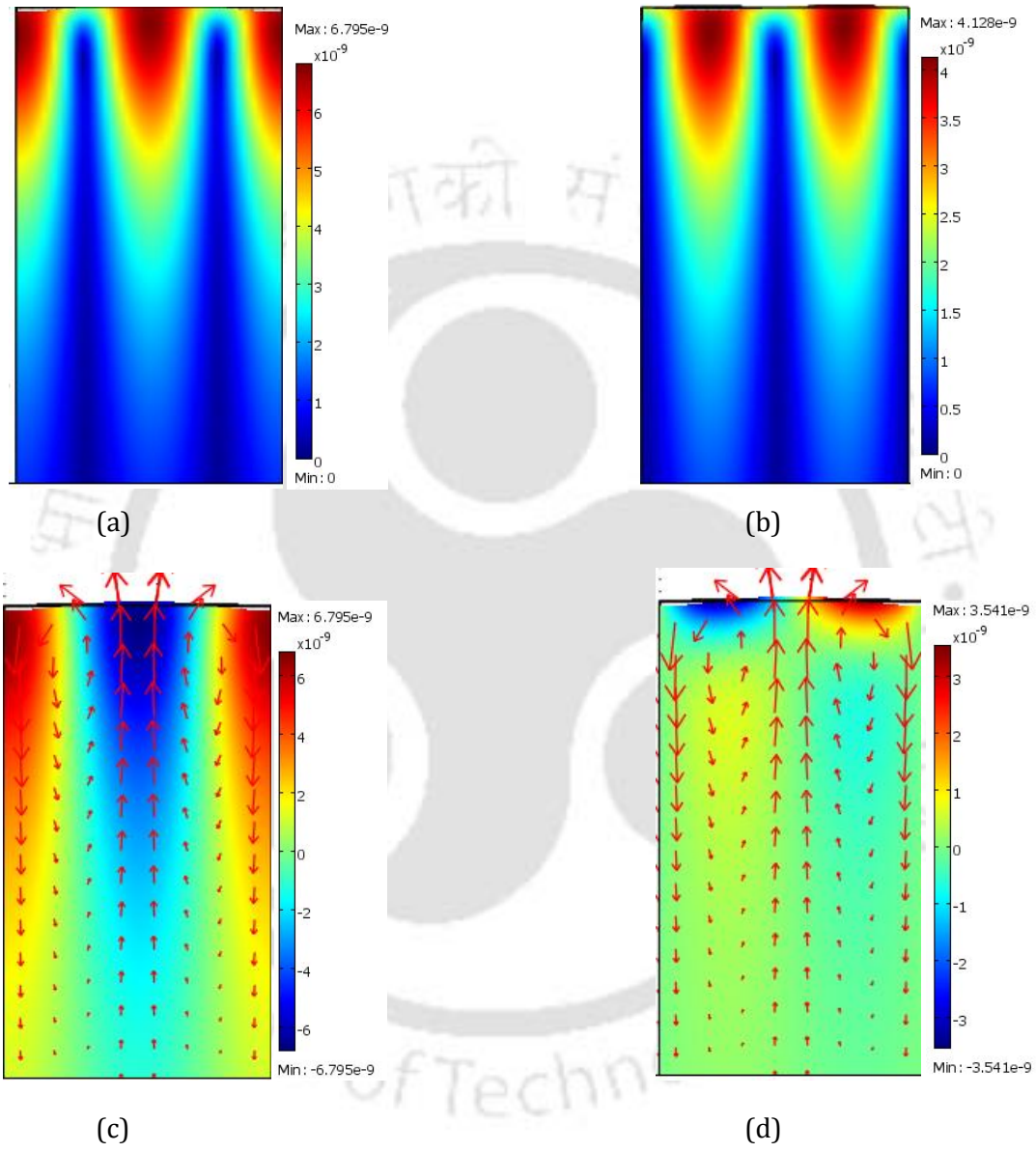

Figure 2.7. (a) Total displacement profile at resonance frequency 97.5 MHz, (b) Total displacement profile at anti-resonance frequency 98.5 MHz, (c) Vertical displacement of the particle, (d) horizontal displacement of the particle. The arrow marks in the figure (c) and (d) shows the particle displacement direction. Note: For simplicity the substrate length shown in the figure is 1.5 λ.

Further eigenfrequency response analysis is performed for varying length of aperture (*W*). Admittance versus frequency plots for an aperture *W* of 10 μm to 150 μm and resonance frequency of the resonator is recorded and tabulated in table 2. It can be seen that the resonance frequency variations are within ± 0.1 MHz.

Table 2.1 Variation in resonance frequency for change in *W*

W (μm)	Resonance frequency (MHz)
10	97.5034
20	97.4703
30	97.4457
50	97.4236
100	97.4972
150	97.4299

Also frequency response analysis is performed using the parametric solver available in COMSOL Multiphysics for varying length of aperture (*W*). Admittance versus frequency plots for an aperture *W* of 10 μm, 30 μm, and 50 μm are shown in figure 2.8. The resonance frequency of the resonator is

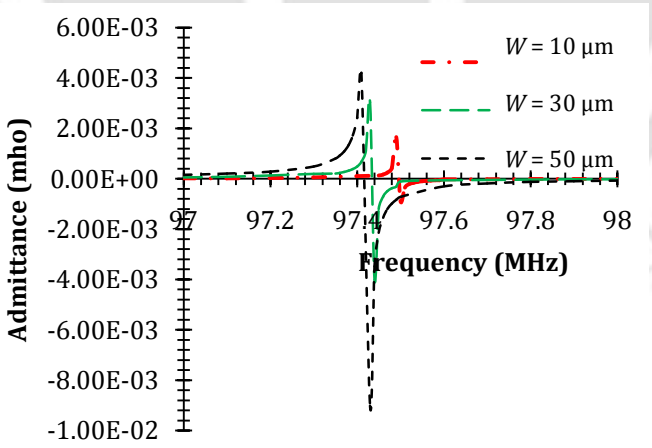

Figure 2.8. Plot of admittance versus frequency for different values of aperture (*W*).

identified as the frequency of for which the admittance value is zero. As an outline the admittance

value increases for increase in aperture length. Accordingly total IDT admittance for fixed aperture is an integral multiple of the reduced model. Thus a SAW resonator structure with minimum aperture length is sufficient to study the effect its resonance frequency of SAW resonator, by this one can minimize the computational cost mentioned in the section 2.4.3.

2.6 FEM simulation of a SAW delay line using COMSOL Multiphysics

2.6.1. The mathematical model for a SAW delay line

As explained in the earlier in section 1.8, the IDT converts electrical energy to mechanical energy and vice versa. The mathematical model of a SAW delay line given by Feng *et al*. [44] is adopted in formulating the simplified simulation methodology. The transmitting IDT can be considered as a force generator that converts electrical voltage to mechanical forces. These forces travel as SAW on the piezoelectric substrate. Consider a transmitting IDT as shown in figure 2.9, and with the number of force generators (fingers) of N_M equal to 5. If the force generated at each finger of transmitter IDT is proportional to the applied voltage, the force at n^{th} finger pair can be written as $F_n(t) = K_1 V_{in}(t)$

where K_1 is proportionality constant of the transducer. V_{in} is the input voltage. The displacement of the wave **u** at the edge of IDT of N_M finger pair can be written as

$$\mathbf{u}(t) = \frac{1}{2v}\sum_{n=1}^{N_M} F_n\left(t - \frac{n\lambda}{v}\right) \tag{33}$$

The displacement of the wave at receiver IDT of the SAW delay line device with delay line of length

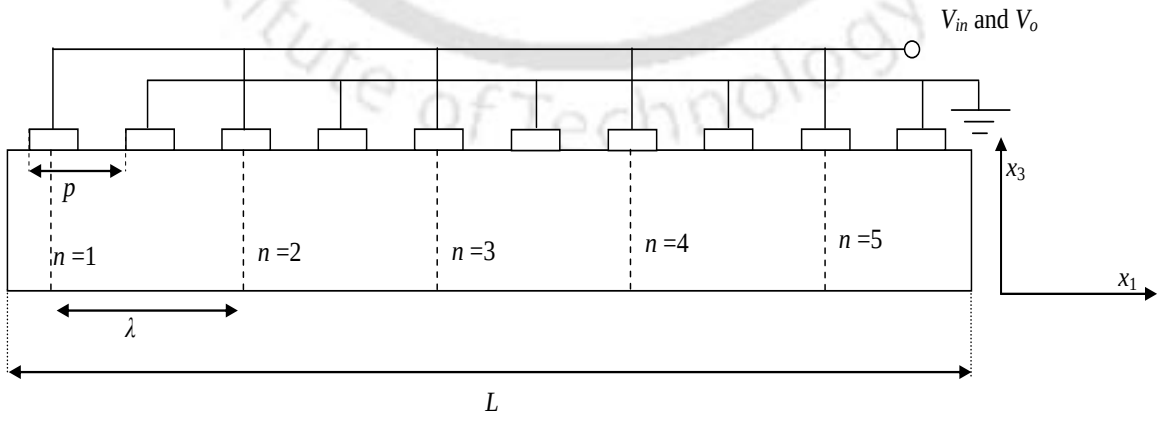

Figure 2.9. A Typical IDT with 5 pairs of electrodes.

L can be written as

$$\mathbf{u}(t)=\frac{1}{2v}\sum_{n=1}^{N_M}F_n\left(t-\frac{n\lambda+N_R\lambda+L}{v}\right) \tag{34}$$

where N_R is the number of finger pair at the receiver IDT. Let q_{out} denote the electric charge produced when the electrodes are subjected to local strain. Assuming that the charge is the sum of the charges produced at each finger and the charge from each finger is proportional to displacement,

$$q_{out}(t)=K_2\sum_{l=1}^{N_R}u_l(t) \tag{35}$$

Accordingly assuming the output voltage is proportional to charge,

$$v_{out}(t)=K_3\,q_{out}(t) \tag{36}$$

K_2 and K_3 are proportionality constants. Thus combining the above equations the output voltage can be expressed as

$$v_{out}(t)=\frac{K_1K_2K_3}{2v}\sum_{l=1}^{N_R}\sum_{n=1}^{N_T}v_{in}\left(t-\frac{n\lambda+l\lambda+L}{v}\right) \tag{37}$$

If an IDT of 100 finger pair, and displacement at edge of point 5th pair from equation (34) can be rewritten as

$$\mathbf{u}(t)=\frac{1}{2v}\sum_{n=1}^{n=100}F_n\left(t-\frac{n\lambda}{v}\right)-\frac{1}{2v}\sum_{n=6}^{n=100}F_n\left(t-\frac{n\lambda}{v}\right) \tag{38}$$

$$\mathbf{u}(t)=\mathbf{u}_a(t)-\mathbf{u}_b(t) \tag{39}$$

The above equation can be further realized in terms of time t as below

$$\mathbf{u}_a(t)=\frac{1}{2v}\sum_{n=1}^{n=100}F_n\left(t-\frac{n\lambda}{v}\right) \text{ for all } t \tag{40}$$

$$\mathbf{u}_b(t)=\frac{1}{2v}\sum_{n=1}^{n=94}F_n\left(t-\frac{n\lambda}{v}\right) \text{ for t >= } n\lambda/v \tag{41}$$

In general, equation (40) can be realized as a one-port SAW resonator consisting of single IDT with 100 finger pairs. As explained in simulation of one-port SAW resonator it is convenient to model equation (40) and (41) by applying infinite periodic boundary conditions to a section of SAW resonator of length $n\lambda$ consisting of single or a pair of IDT. The simulation procedure adopted in COMSOL Multiphysics to solve the SAW delay line model is explained in the following section.

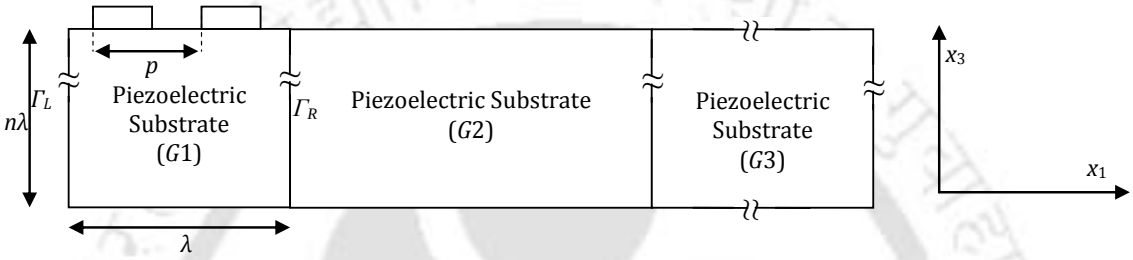

Figure 2.10. SAW delay line structure considered for simulation.

2.6.2. Simulation methodology

YZ-lithium niobate piezoelectric crystal is assumed as the piezoelectric substrate in the simulations. The alternate fingers are shorted and given input voltage. The SAW delay line structure used in simulation consists of 2 blocks, the transmitter IDT ($G1$) to generate the rayleigh waves, delay line ($G2$) as shown in Figure 2.10. The SAW delay line structure consists of transmitter and receiver IDT with two electrodes of each 8.75 μm ($\lambda/4$) in width (wavelength of λ= 34.88 μm) and a delay line of 69.76 μm (2 λ) in length. Standing waves at the transmitter IDT propagates SAW in the both directions of the IDT [45]. Periodic boundary conditions are applied for transmitter and receiver IDTs as discussed in previous section. Critical damping is assumed at the edge of the receiver ($G3$) and bottom of the whole device to avoid reflections to the delay line. The equations relating to critical damping are provided in appendix D. To analyze propagation of SAW waves over the delay line, transient analysis of the SAW delay line is performed using direct solver SPOOLES available in COMSOL Multiphysics [33] with a time interval of 0.1 ns for 12 ns for 100 MHz 1 V peak to peak input sine wave. As a first stage in test simulation, time domain analysis is performed only for the SAW transmitter alone and the solutions (displacement and potential) of the transmitters are stored and provided to boundary of delay line. For the final stage solutions computed at the end of

delay line are stored and given to the receiver IDT. The displacements along x_1 and x_3, potential at the transmitter, delay line and receiver electrode are recorded for every time t.

2.6.3. Results and discussions

The propagation of SAW (along x_3) over the delay line after 100 ns is shown in figure 2.11 (a). The maximum x_3 displacement generated at the transmitter IDT is 3.8×10^{-11} m as shown in figure 2.11 (b). As the input potential is a continuous sinusoidal wave and for an IDT of five fingers considered, the amplitude attains stability from the fifth cycle. To detect the SAW travelled along the delay line even a single point at the end of the delay line can convey the information of the SAW passing by. Any delay or attenuation caused due the sensing film can be inferred, by which simulation of receiver can be avoided, and number of degrees of freedom to be solved can be reduced. The recorded x_3 and x_1 displacements of the SAW at the edge of delay line are as shown in the Figure 2.11 (c) and they are out of phase by 90° with amplitude of 2.8×10^{-11} m and 2.1×10^{-11} m, respectively. For a case of transmitter IDT with N_M = 10 the degrees of freedom to be computed is found to be 26082, by this method it can be reduced up to 1377. In case of simulating the total SAW device with transmitter of 10 finger pair and a delay line of two wave lengths the degrees of freedom found to be 58125, by this method it can be reduced up to 16128 and the computational complexity is reduced by 72.25 %. Thus the proposed simplified FEM methodology can be extended to study the various other aspects of SAW sensor.

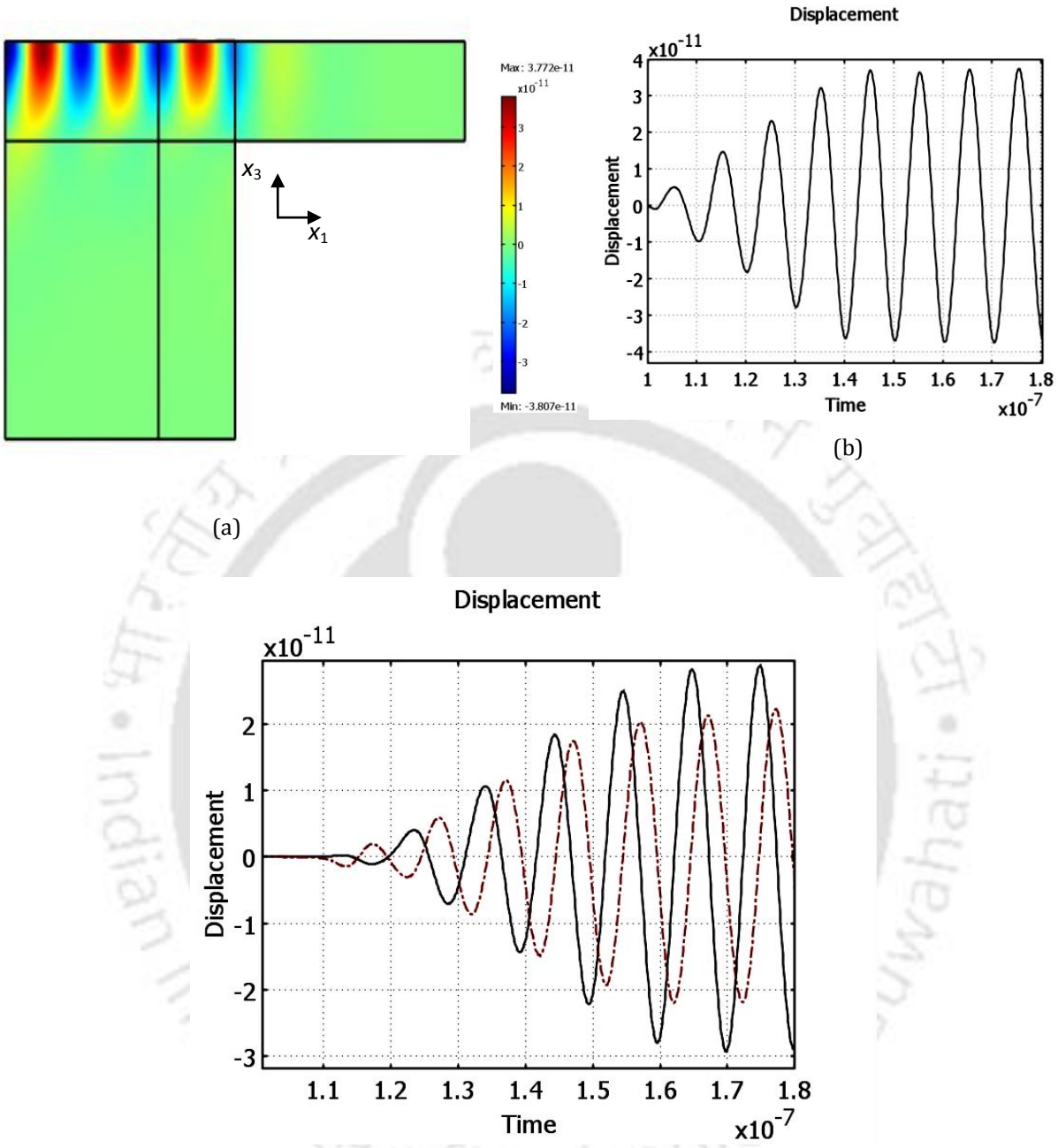

Figure 2.11. (a) Profile of vertical displacement of SAW amplitude over the delay line, (b) Vertical displacement of SAW measured at the edge of the transmitter IDT, (c) Vertical and horizontal displacement of SAW measured at the edge of the delay line.

2.7 FEM simulation of SAW sensor for studying mass loading effect

To design SAW sensors based on mass loading principle, it is very essential to study the effect of density and elastic property of the sensing film separately. In concern with memory usage of the machine and computation time, we have assumed two finger model transmitting IDT, as the fingers of IDT are periodic in nature, infinite periodic boundary conditions are applied for the boundaries of the transmitting IDT.

2.7.1. Material and design of the structure

A slice of SAW device along x_1 is considered and is divided in sections as shown in the figure 2.12. The SAW model considered in this simulation consists of 3 geometries, the transmitter IDT ($G1$) to generate the standing Rayleigh waves, delay line with a two receiving electrodes as receiver IDT ($G2$). Further delay line is extended to two wavelengths and critical damping is assumed for the extended substrate ($G3$) (as explained in previous section) to avoid reflections at the end of the delay line. All 3D structures are made out from extrusion of a 2D mapped mesh in COMSOL Multiphysics.

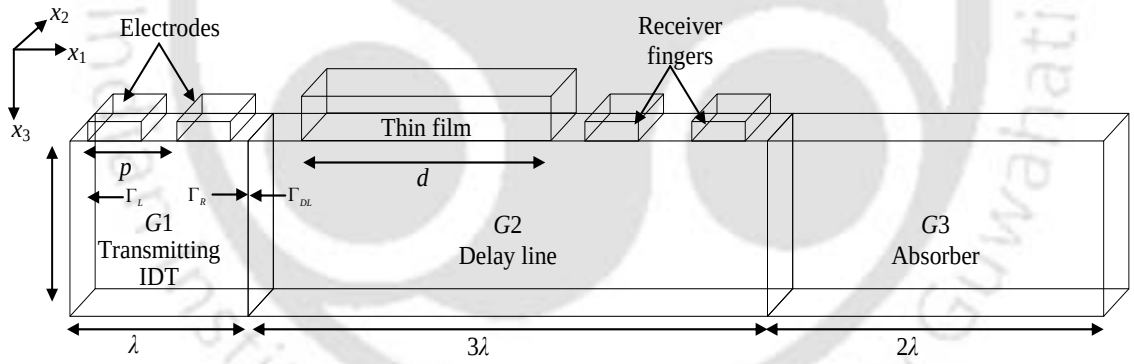

Figure 2. 12. 3D SAW sensor geometry considered for the simulation.

A delay line of 120.8 μm (3.4 λ) in length and 174.4 μm (5 λ) in height is considered and a thin film with dimensions of 65μm (1.8 λ) × 2 μm ×1 μm is placed 8.75 μm ($\lambda/4$) from IDT over the delay line. Mass less electrodes is assumed for the transmitting IDT and receiving fingers to avoid mass loading due to these electrodes. To study the effect of mass loading over the SAW for the model considered, Young's modulus and density of the thin film over the delay line is varied and time domain analysis is performed for every trail. The transmitting and receiving finger has length of 8.75 μm along x_2. The displacement in the x_2 is constrained to zero. The fingers in IDTs are periodic, hence appropriate periodic boundary conditions are applied for the transmitting IDT using the

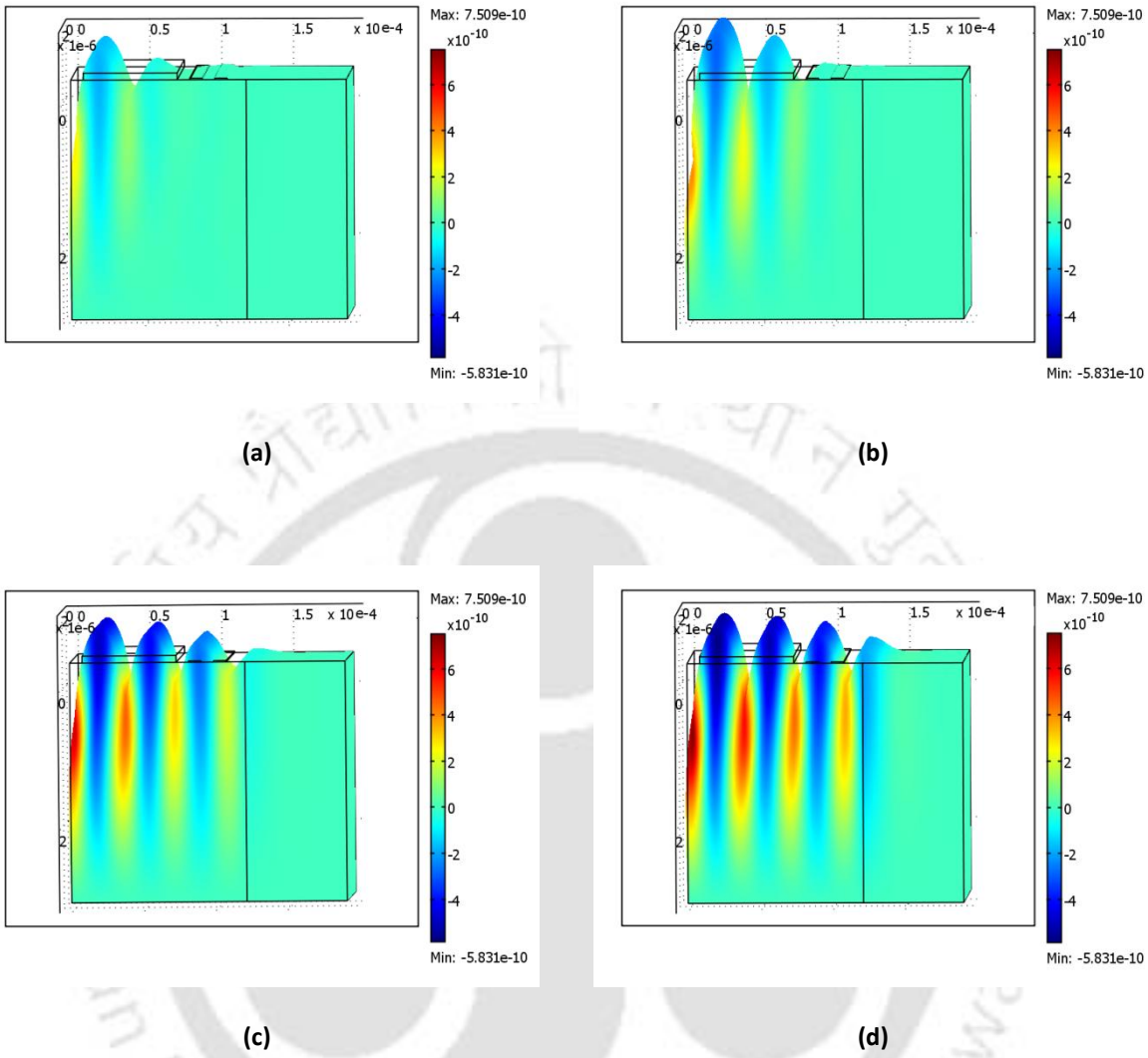

Figure 2.13. Propagation of SAW in the delay line and absorber sections. Vertical displacements along x_3 and resultant deformation are shown for time interval of (a) after 20 ns, (b) 30 ns, (c) 50 ns, (d) 100 ns. For simplicity propagation of SAW in the transmitter section is not shown.

equation (32). The degrees of freedom of the right periodic boundary (Γ_R) are set to be negative of those from the left periodic boundary (Γ_L) (see Figure 2.12) [42].

2.7.2. Simulation procedure

2D mapped mesh is extruded to 3D geometries ($G1$, $G2$, and $G3$). The total mesh has 17714 degrees of freedom. Frequency response analysis is performed for the transmitter electrodes and synchronous frequency of the transmitter found to be 100 MHz. In order to analyze propagation of

SAW waves over the delay line, a 100 MHz, 10 V peak to peak sinusoidal signals is applied to the electrodes of transmitting IDT and time domain analysis of the SAW sensor is performed with a time interval of 0.1 ns for 12 ns. As a first stage, time domain analysis is performed only for the SAW transmitter and computed solutions (displacement and potential) of the transmitters are stored and provided to boundary Γ_{DL} of $G2$ (see figure 2.12) for the further stages of simulation. The Young's modulus (E) and density (ρ) of the thin film is varied to study the sensitivity to mass loading of the modeled SAW sensor. Mass loading due to hard material (young's modulus greater than 1 GPa) like metals and soft material (young's modulus in the order of 10^6) like polymers is studied in four cases. In the first case young's modulus of 10 GPa is assumed for the sensing film, which is equivalent to hard film and three density values 1000 kg/m^3, 2500 kg/m^3 and 5000 kg/m^3 are assumed. For the second case, a constant density of 1000 kg/m^3 is assumed for the sensing film, while the young's modulus is varied as 10 GPa, 50 GPa and 100 GPa and the effect of young's modulus is studied. In case three a soft film of young's modulus 10 MPa and three density values 1000 kg/m^3, 2500 kg/m^3 and 5000 kg/m^3 are assumed. In case of a soft film of density 1000 kg/m^3 is assumed for the thin film and young's modulus of the film is varied as 1 MPa, 10 MPa, and 50 MPa. In all case of simulation vertical displacement, horizontal displacement and electric potential of the SAW at the receiver electrode are recorded.

2.7.3. Results and discussion

The simulated propagation of SAW over the delay line is as shown in Figure 2.13 (a)-(d). For simplicity the generated standing waves over the transmitter is not shown. Figure 2.13 shows the SAW vertical displacement with amplitude in the order of 10^{-10} m and resultant deformation of the delay line in both x_1 and x_3 directions. It can be noted that first cycle of SAW has taken 30 ns to reach the receiver IDT. The recorded electric potentials for all the four cases discussed in the above section are shown in figure 2.14 2.15, 2.16 and 2.17. As shown in Figure 2.14 a time delay of 1 ns and 1.4 ns is observed for a film of young's modulus 10 GPa compared to a film with young's modulus 100 GPa and 50 GPa respectively. For the case 2 as shown in figure 2.15, a time delay of 0.3 ns and 0.9 ns is observed for film of density 2500 kg/m^3 and 5000 kg/m^3 compared to a film with density of 1000 kg/m^3. For case 3 and case 4, the observed delays are comparatively small as shown in Figure 2.16 and figure 2.17 respectively. A time delay of 0.033 ns and 0.04 ns is observed for a soft polymer film with density value of 2500 kg/m^3 and 5000 kg/m^3 compared with a film of 1000 kg/m^3. A time delay of 0.01 ns and 0.9 ns is observed for film with young's modulus 1 Mpa compared to a film with young's modulus of 10 MPa and 50 MPa. Thus it is verified that hard film

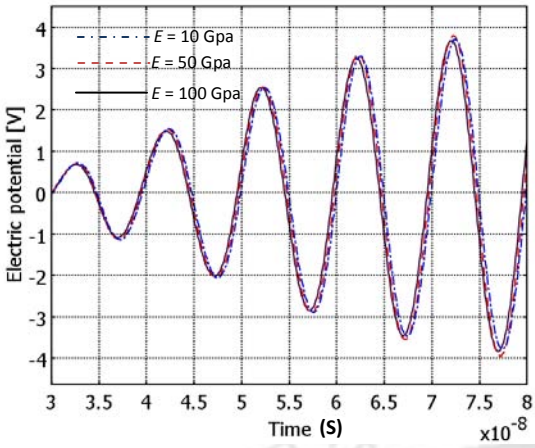

Figure 2.14. Delay observed for hard material of E = 10 GPa, 50 GPa, 100 GPa and ρ = 1000 kg/m^3 values respectively.

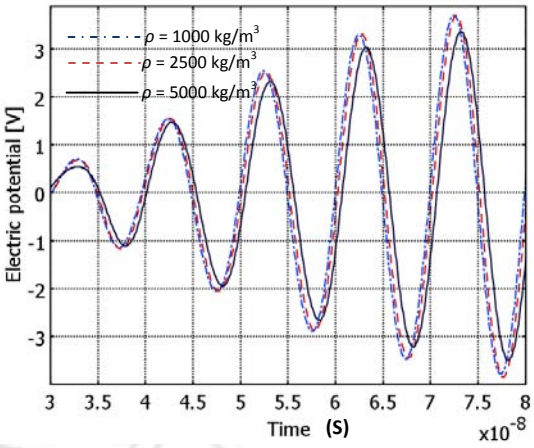

Figure 2.15. Delay observed for hard material of E = 10 GPa and ρ = 1000 kg/m^3, 2500 kg/m^3, 5000 kg/m^3 values respectively.

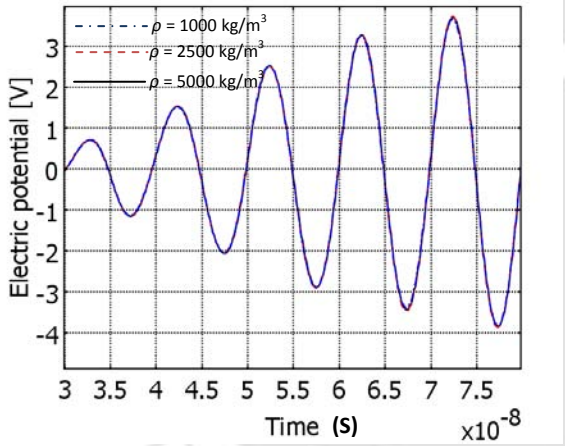

Figure 2.16. Delay observed for soft material of E = 10 MPa and ρ=1000 kg/m^3, 2500 kg/m^3, 5000 kg/m^3.As the delays are negligible, the waveforms are overlapping.

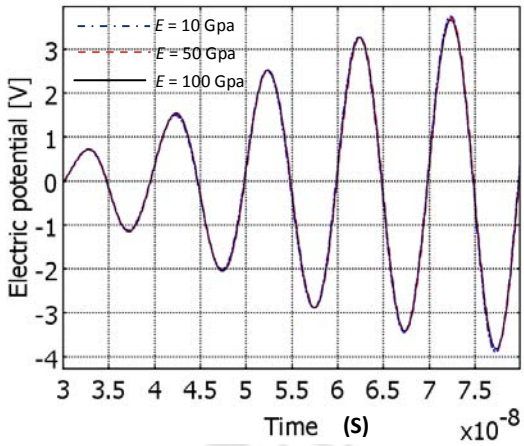

Figure 2.17. Delay observed for soft material of E = 1 MPa, 10 MPa and 50 MPa and ρ = 1000 kg/m^3. As the delays are negligible, the waveforms are overlapping.

produces more mass loading compared to soft films with same densities. In both soft film and hard film increase in young's modulus leads to increase in velocity of the SAW, however in any case the density of the thin film decreases the velocity of SAW. The velocity of SAW decreases for increase in film density. The velocity change for the case of soft films due to change in the young's modulus is comparatively less. Also it is shown that a transmitter IDT with appropriate periodic boundary conditions can be employed for generating SAW. A sensor sensitive to mass loading is modeled and

simulated using FEM based software COMSOL Multiphysics. A section of SAW sensor was considered in the 3D-simulation with absorbing boundaries and propagation of SAW over the delay line was studied. The number of DOF to solve for the FEM model is reduced by following reasons, Simulation of whole structure of SAW transmitter is avoided by employing a resonator type transmitting IDT to generate SAW and receiver IDT has two fingers to detect the SAW passing by, and also a section of SAW sensor is considered for the simulation. The mass sensitivity of SAW sensor model is studied by varying the young's modulus and density of the film coated over the delay line. It was observed that velocity of SAW decreases for increase in density of the thin film coated over the substrate and the velocity of SAW increases with increase in young's modulus of the thin film. The time delay observed for soft material is much smaller compared to hard material. The model can be further extended to study the various other aspects of SAW sensor.

2.8 FEM simulation of SAW hydrogen sensor

In this simulation a palladium film is coated over the delay line. The simulation of SAW sensor is performed by varying the density, youngs modulus and volume of the film assumed over the delay line.

2.8.1 Simulation methodology

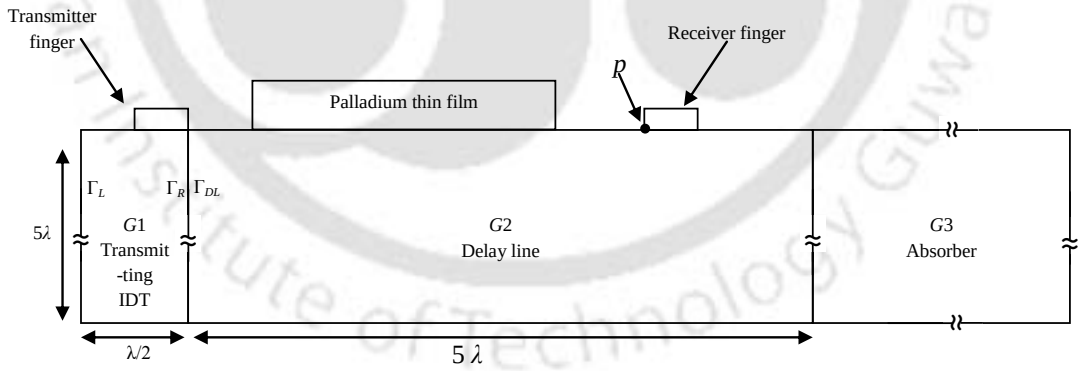

Figure 2. 18. Section of SAW sensor geometry considered for the simulation.

The total SAW hydrogen sensor as a 2D plain strain structure as shown in the figure 2.18. The SAW model considered in this simulation consists of 3 geometries, the transmitter IDT ($G1$) to generate the standing rayleigh waves, delay line with a receiving electrode as receiver IDT ($G2$). Further delay line is extended to two wavelengths and critical damping is assumed for the extended

substrate ($G3$) to avoid reflections at the end of the delay line. YZ lithium niobate is assumed for the substrate. A delay line of 120.8 μm in length and 174.4 μm in height is considered. A palladium thin film of density 12000 Kg/m^3 and young's modulus of 129 GPa with dimensions of 52.32 μm x 1μm is placed 8.75 μm from IDT over the delay line. Mass less electrodes are assumed for the transmitting and receiving finger to avoid mass loading due to these electrodes. As the fingers in IDTs are periodic, appropriate periodic boundary conditions are applied for the transmitting IDT using the equation (35). 2D mapped mesh is applied for the geometries ($G1$, $G2$, and $G3$). The mesh has total 26286 degrees of freedom. Time domain analyses of SAW hydrogen sensor are performed in two stages. In the first stage the absence of SAW hydrogen sensor is simulated. In the second stage 3 % absorption of hydrogen by palladium film to palladium hydride is simulated, where the palladium thin film density is decreased by 2 %, volume is increased by 10 % and young's modulus is reduced by 14 % [46][36] and time domain analysis of SAW delay line with modified properties of thin film is performed. Frequency response analysis is performed for the transmitting IDT and synchronous frequency of the transmitter found to be 98 MHz. Hence a 98 MHz, 20 V peak to peak sinusoidal signal is applied to the electrode of transmitting IDT and time domain analysis of $G1$ alone is performed for 70 ns. Further the simulated displacement and potential at the boundary Γ_R are stored and provided to Γ_{DL} boundary of the delay line for the further two stage of analysis of SAW hydrogen sensor.

2.8.2 Results and discussions

The displacement and electric potential at receiving point p (see figure 2.18) are recorded in both the stages. Total displacement of SAW is calculated by equation, Total displacement = $\sqrt{|u_1|^2+|u_2|^2+|u_3|^2}$, Figure 2.19 shows the profile of SAW total displacement over the delay line, for simplicity wave propagation over $G2$ and $G3$ alone is shown. Figure 2.20 shows the total displacement recorded at the receiver electrode for the presence and absence of hydrogen. It can be seen that SAW displacements amplitude are in the order of 10^{-10}. The recorded SAW electric potential, vertical displacement for the presence and absence of hydrogen as discussed in section 2.8.2 are shown in figure 2.21 and 2.22. It is evident that there is a significant attenuation and delay of SAW due to change in properties of the palladium film. It can be seen from figure 2.21 that SAW has taken 35 ns to reach the receiver electrode. From figure 2.22 it can be observed that the vertical displacement of SAW in presence of hydrogen is delayed by 0.45 ns when compared to absence of hydrogen.

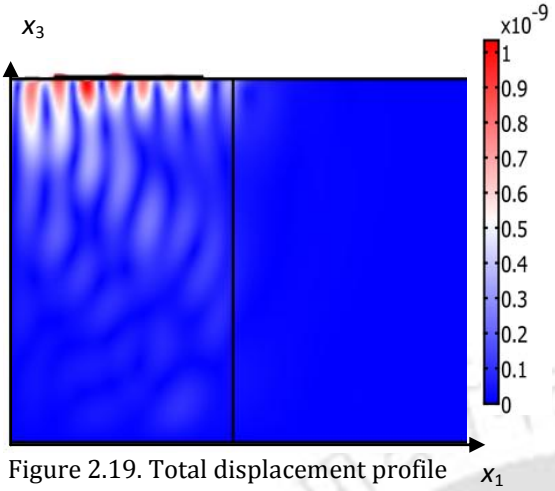

Figure 2.19. Total displacement profile of SAW in the delay line.

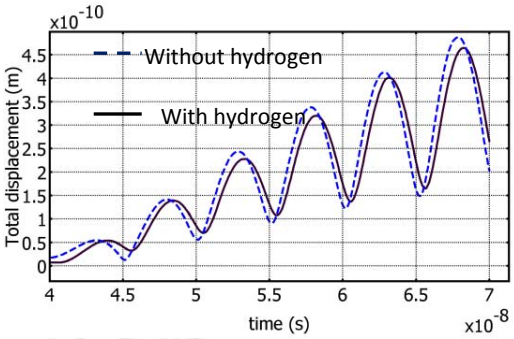

Figure 2.20. Total displacement of SAW recorded at the receiver point in the presence and absence of hydrogen.

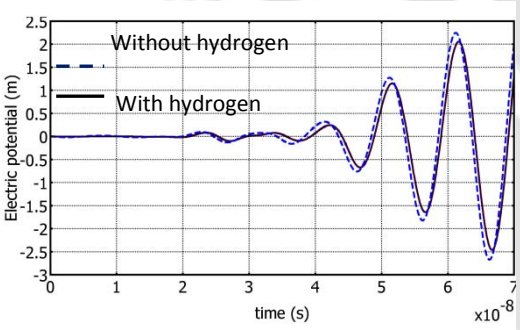

Figure 2.21. Electric potential of SAW recorded at the receiver point in presence and absence of hydrogen.

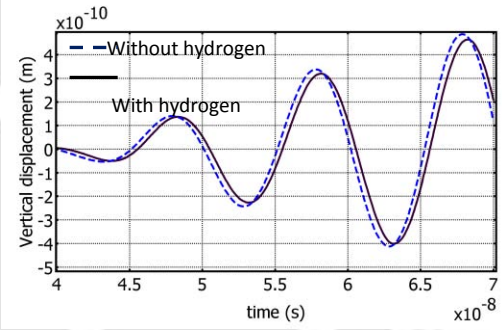

Figure 2.22. Vertical displacement of SAW recorded at the receiver point in presence and absence of hydrogen.

2.9 Summary

In this chapter a brief introduction on various SAW device modeling techniques such as equivalent circuit method, COM model, and simulation methods such as FEM were discussed. In summary,

FEM simulations of one port SAW resonator is performed using FEM based software, COMSOL Multiphysics. The effect of aperture length of resonator is examined. It is shown that COMSOL Multiphysics can be used to simulate SAW devices.

A sensor sensitive to mass loading is modeled and simulated using COMSOL Multiphysics. A section of SAW sensor is considered in the 3D-simulation with absorbing boundaries and propagation of SAW over the delay line is studied. The number of DOF to solve for the FEM model is reduced by

following reasons: simulation of whole structure of SAW transmitter is avoided by employing a resonator type transmitting IDT to generate SAW and receiver IDT has two fingers to detect the SAW passing by, and also a section of SAW sensor is considered for the simulation. The mass sensitivity of SAW sensor model is studied by varying the young's modulus and density of the film coated over the delay line. It is observed that velocity of SAW decreases for increase in density of the thin film coated over the substrate and the velocity of SAW increases with increase in young's modulus of the thin film. The time delay observed for soft material is much smaller compared to hard material. The model can be further extended to study the various other aspects of SAW sensor.

Furthere a simplified SAW delay line hydrogen sensor is modeled and simulated using COMSOL Multiphysics. The number of degrees of freedom (DOF) to solve for the FEM model of SAW hydrogen sensor is reduced by proposed method in section 2.6. A delay of 0.45 ns is observed for the 3 % absorption of hydrogen by the palladium film compared with absence of hydrogen.

3

Mass Loading Effects of High Aspect Ratio Structures and Thin Film in SAW Resonators

This chapter discusses the mass loading effect of high aspect ratio pillar, one kind of resonant structure attached to SAW device and their application towards SAW sensor. The results and discussions on FEM simulation of high aspect ratio pillar grown normal to the surface of a SAW resonator, FEM simulation of a SAW hydrogen sensor consisting of palladium nano-pillar as sensing medium and increase in sensitivity of SAW sensor with the use of high aspect ratio pillar as sensing medium are elaborated. Initially mass loading effect of thin film in SAW devices and design and development of relative humidity sensor using a thin film of nanogel sensing medium are discussed.

3.1 Mass loading effect in SAW devices

As described in chapter 1, SAW resonators are mainly classified into two types: one-port SAW resonator and two-port SAW resonators. One-port SAW resonator function is obtained by multiple reflections between fingers of a long Interdigital transducer (IDT) or by reflections from reflectors at either end of a short IDT.[2] The shift in the resonance frequency of a SAW resonator owing to the changes in mass loading, conductivity, permittivity, and viscosity over the SAW path can be employed in sensing applications.

Mass loading effect in SAW devices is extremely employed for sensing applications. Penza *et al* [47] developed an organic vapor sensor by coating a film of carbon nanotube composites over the surface of a SAW resonator. Nomura *et al* [48] reported mass loading effect of Langmuir-Blodgett film coated over the surface of a SAW resonator and demonstrated that an increase in mass loading decreases the resonance frequency. The density, elastic modulus, and dimensions of the thin film determine the amount of mass loading. The velocity change (Δv) due to mass loading of a thin film over the SAW path can be expressed as [2]

$$\Delta v = (k_1 + k_2) f v h \rho - k_2 f v h \left\{ \frac{4\mu'(\lambda' + \mu')}{v^2(\lambda' + 2\mu')} \right\} \tag{42}$$

where f is the operating frequency without the film, ρ is the density of the film, λ' and μ' are bulk and shear elastic modulii of the film, v is the velocity of SAW, and h is the film thickness. k_1 and k_2 are material constants of the substrate. For example, Y-Z lithium niobate has k_1 = -3.775×10^{-8} m^2skg^{-1} and k_2 = -1.73×10^{-8} m^2skg^{-1} [2]. The phenomenon of changes in dimension, density and elastic properties of a sensing medium coated over a SAW resonator or a delay line is widely used in developing sensors. An experimental study on SAW based relative humidity (RH) sensor based on massloading principle is elaborated in the following section.

3.2 Development of SAW based humidity sensor based on mass loading effect

In the following work, sensing film made of a specific nanogel is coated over SAW devices and relative humidity sensor based on the mass loading phenomenon is developed. In the following section detailed description of the sensing medium, experimental setup and results of experiment on the SAW humidity sensor are presented.

3.2.1 Humidity Sensor using NIPAAm nanogel as sensing medium in SAW devices

Humidity sensors find vital applications in the field of industrial processing, environmental control, semiconductor industry, automobiles, medical, agriculture and domestic applications [49]. As discussed in previous chapters the shift in the SAW velocity in a SAW device owing to the changes in mass loading, conductivity, permittivity, and viscosity over the SAW path can be employed in sensing applications. Following researchers have reported SAW humidity sensors. penza *et al.* [50] used polyvinyl-alcohol as sensing medium in SAW resonator and measured relative humidity (RH). Tashtoush *et al*. [51] used polyXIO film in SAW delay line and measured RH for a complete range of 0 % to 100 % of RH. Ippolito *et al*. [52] employed tungsten tri oxide as sensing medium and zinc oxide as intermediate layer in YX $LiTaO_3$ layered SAW device and sensed ethanol in dry and humid air. Wu *et al*. [53] developed high sensitive humidity sensor by using polyaniline (PANI) nanofibres as sensing medium in a SAW resonator. In this present work, we have investigated the relative humidity change response of *N*-isopropylacrylamide (NIPAAm) nanogel as sensing medium deposited on two types of SAW devices namely SAW Resonator and SAW delay line. The NIPAAm nanogel absorbs moisture and its particle size increases and offer mass loading to the SAW device for increase in relative humidity or moisture content. The experimental set up and RH measurement is elaborated below.

3.2.2 Experimental setup of SAW based relative humidity sensor

The experimental setup consists of humidity controlled chamber, SAW humidity sensor and network analyzer.

(a) Humidity control chamber

An air tight 25 cm × 25 cm transparent rectangular box made of polycarbonate material was used as the humidity control test chamber as shown in figure 3.1. Increase in humidity is achieved by feeding water vapours into the chamber. Water vapours are generated by bubbling atmospheric air

into a reaction wash glass which is filled with ultra pure water (Milli-Q Reagent Water System, Millipore). The maximum RH achieved in the test chamber was 94 %. The decrease of humidity was achieved by the using of silica gel as a desiccant inside the test chamber. In course of time, silica gel absorbs the water vapour inside the chamber. Hence use of inlet of water vapours and silica gel activity allowed varying RH from 15 % to 95 % inside the test chamber in a controlled fashion

(b) Humidity sensing material

NIPAAm nanogel is used as the sensing medium in this present study [54]. The nanogel was synthesized by single step surfactant free emulsion polymerization reaction method. The field emission scanning electron microscopy (FESEM) image of nanogel is shown in figure 3.2. The prepared nanogel particles have dimension less than 180 nm. It is reported that dynamic light scattering (DLS) analysis of these particles shows increase in size of the particles up to 100 % when dispersed in water at room temperature [54]. Stock solution of nanogels is prepared by dispersing 4 mg of nanogel in 0.5 ml of solvent.

(c) SAW resonator as humidity sensor

A commercial one port resonator by EPCOS (R 801) was used for this study. The center frequency of the ceramic packaged (QCCMA) resonator was 315 MHz with a typical Q factor of 17000. Package of two resonators were opened up carefully. An optimised quantity of 12 µl NIPAAm nanogel stock solution was dispersed over one of the resonators and NIPAAm nanogel film was coated by solvent evaporation method. The other resonator was left without any coating to serve as the reference device. Any change in resonance frequency of SAW resonator caused by the changes other than change in properties of NIPAAm can be eliminated by measuring change in resonance frequency of reference SAW resonator.

(d) Relative humidity measurement

Shielded copper wires were carefully soldered to the leads of the SAW resonator. Both the resonators were placed in close proximity inside the test chamber. The resonators were connected to a two port network analyser (Agilent HP8753). S_{11} and S_{22} parameters were measured and recorded simultaneously to obtain the resonance frequencies of the sensing resonator and the resonator respectively. Commercial RH sensor (DTH10, UEI) was placed close to both the resonators to record the RH and temperature inside the test chamber. The resonance frequency shift is calculated from difference between the resonance frequencies of the sensing resonator and

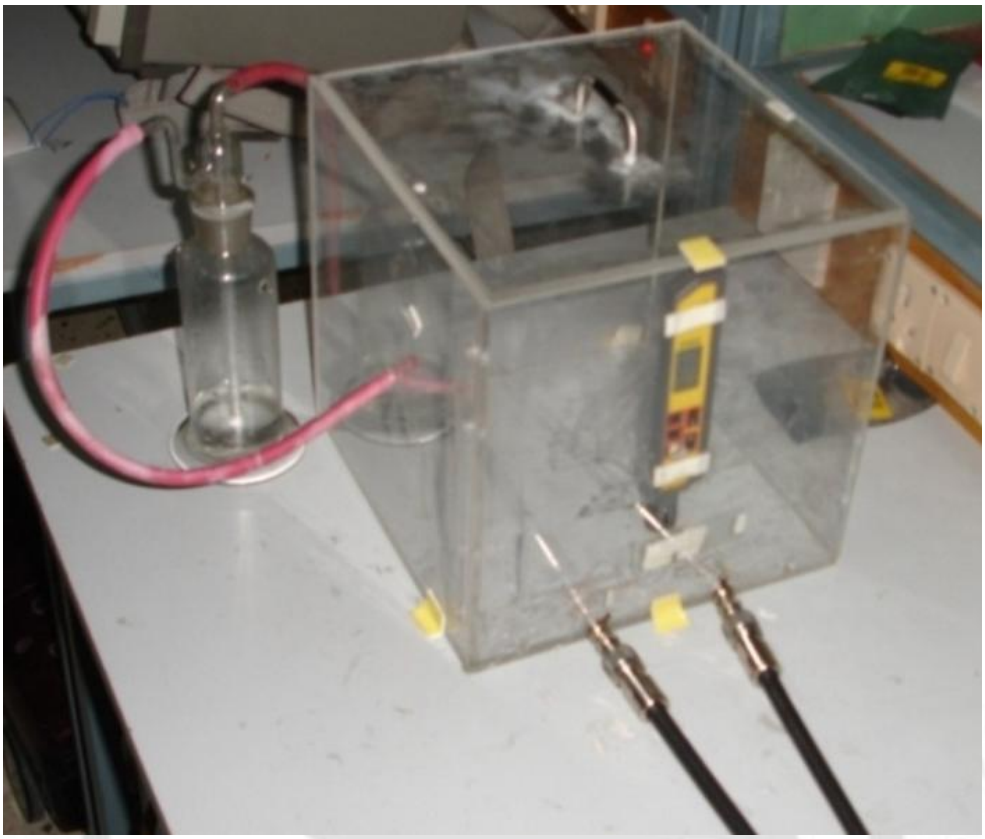

Figure 3.1. Experimental setup showing the RH test chamber.

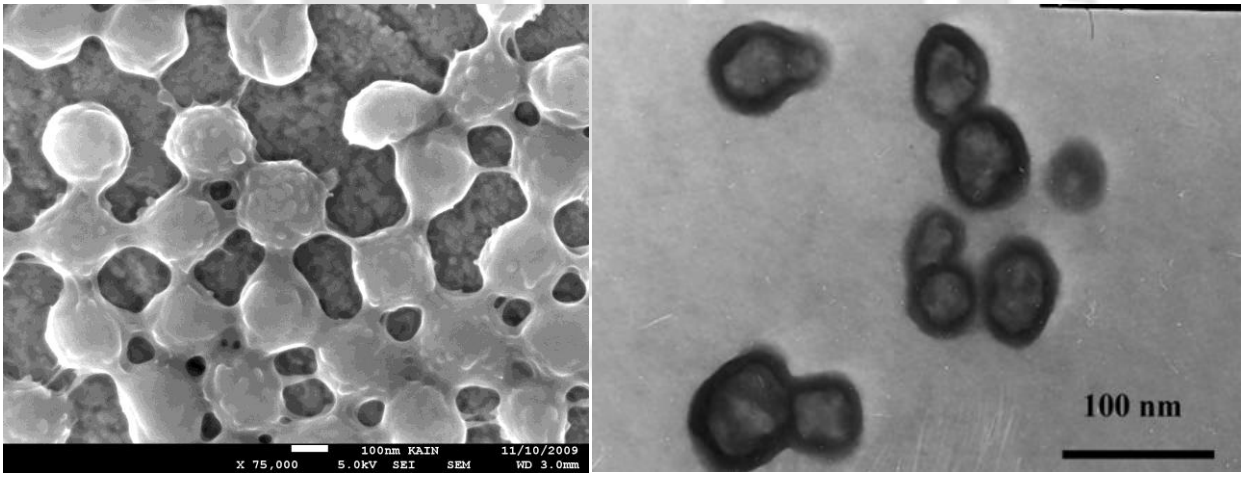

Figure 3.2. (a) and (b) FESEM and TEM image of the prepared NIPAAm nanogel respectively. It can be observed the size of the particles are in the range of 70 to 180 nm.

the reference resonator. All measurements were done at constant temperature of 28° C.

3.2.3 Results and discussions

The S_{11} parameter plot of reference SAW resonator and SAW resonator with nanogel coating are shown in figure 3.3(a) and figure 3.3(b), respectively. These measurements are done at room temperature of 28° C and RH of 72 %. The resonance frequency shift is calculated by subtracting resonance frequency of SAW resonator with sensing film from resonance frequency of SAW resonator without sensing medium. It can be seen from figure 3.3 (a) and 3.3 (b) that a resonance frequency shift with of 24 kHz is observed in presence of nanogel coating. The measured resonance frequency of the SAW resonator humidity sensor for RH of 20 % and 81 % is shown in figure 3.4. It can be observed from the S_{11} parameter plot that there is a resonance frequency shift of 25 kHz. The humidity inside the chamber was decreased from 80 % to 15 % and the resonance frequency of SAW resonators was recorded at regular intervals. Figure 3.5 shows the plot of resonance frequency shift of resonator humidity sensor with respect to the reference resonator. NIPAAm nanogel increase in size due to absorption of moisture inside the chamber and hence result in mass loading to the SAW resonator. As humidity is decreased the mass loading to the SAW resonator also

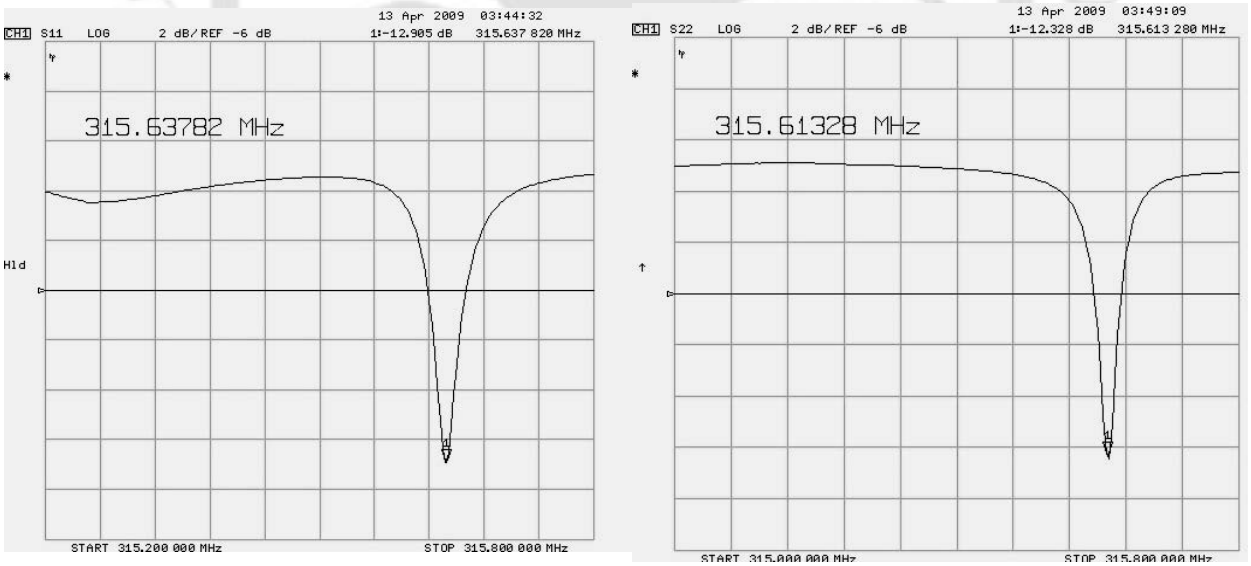

(a) (b)

Figure 3.3. (a) Plot of S_{11} parameter of SAW resonator, (b) Plot of S_{11} parameter of SAW resonator coated with sensing medium. A resonance frequency shift of 24 kHz is observed due to mass loading of the sensing film.

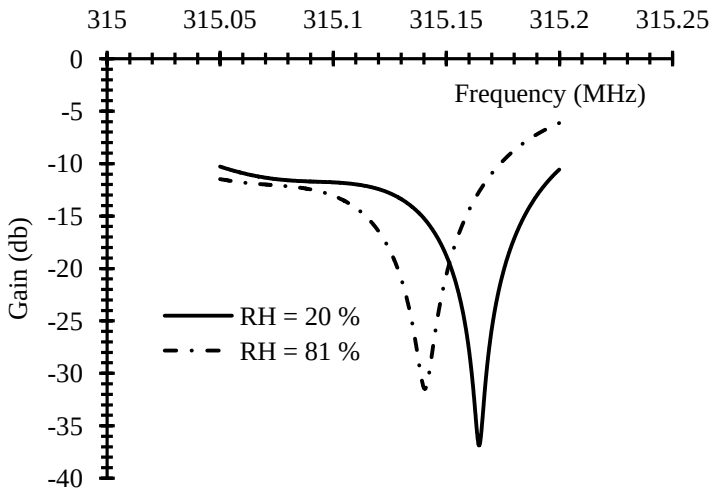

Figure 3.4. S_{11} parameter plot of SAW resonator humidity sensor recorded for RH= 20 % and 81 %.

decreases and results in decrease in resonance frequency shift. A shift of 32 kHz was observed for a humidity change of 77.5 % to 15. 1 %. Further to study the hysteresis characteristics of the sensor, RH inside the chamber was increased from 15 % to 81 % and corresponding resonance frequency of the sensor and the reference resonator were plotted in figure 3.5 and shown in table 3.1. It can be observed that change in RH from low to high shows similar characteristics as before. It can be noted that there is a resonance frequency shift of 19 kHz for an increase in humidity of 15 % to 81 %. The contribution of NIPAAm nanogel in sensing RH is further studied by coating 12 µl of nanogel stock solution over a SAW interdigital transducer (IDT) with the same experimental setup. SAW IDTs with operating frequency of 51. 3 MHz and 20 mS admittance were fabricated using standard photolithography techniques as explained in section 4.1 of chapter 4. The various parameters of the design of the SAW device are as follows: a periodic IDT (see figure 1.2 (d) in chapter 1) of period p = 34 µm, aperture w = 2000 µm and the number of finger pairs N = 28. The measure S_{11} parameter of the fabricated IDT is shown in figure 3.6. Optical microscope image of IDT coated with nanogel is shown in figure 3.7. One of the IDT is left without any coating of nanogel to serve the reference purpose. Resonance frequency of the IDT sensor and reference IDT were recorded at regular intervals for increase in RH. Figure 3.8 and table 3.2 shows the resonance frequency shift for increase in RH for the case of SAW IDT sensor. It can be observed that a resonance shift of 21 kHz was observed for a RH change of 17 % to 94 %.

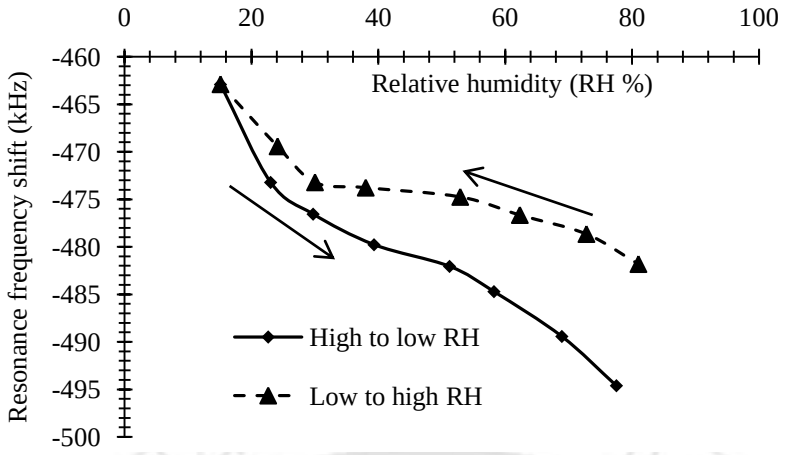

Figure 3.5. Plot of resonance frequency shift versus relative humidity for the case of SAW resonator humidity sensor. A resonance shift of 32 kHz was observed for a RH change of 15 % to 81 %.

Table 3.1. Resonance frequency shift observed for the case of resonator humidity sensor for different RH values

High to low RH		Low to high RH	
RH (%)	Resonance frequency shift (kHz)	RH (%)	Resonance frequency shift (kHz)
77	-494.62	15.1	-462.96
68.9	-489.44	24.1	-469.43
58.2	-484.72	30	-473.22
51.2	-482.06	38	-473.72
39.3	-479.28	52.9	-474.75
29.7	-476.56	62.3	-476.66
23	-473.22	72.8	-478.66
15.1	-462.96	81	-481.81

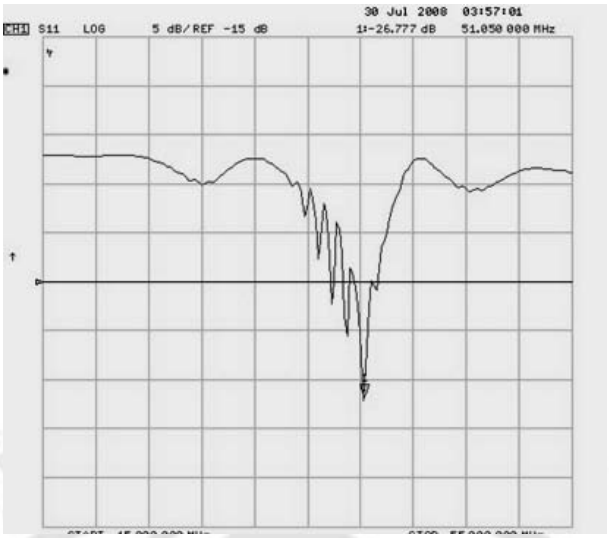

Figure 3.6. S_{11}parameter measurement of SAW IDT sensor without any sensing medium.

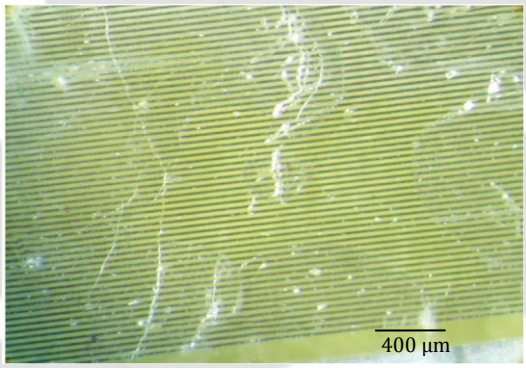

Figure 3.7. Optical microscope image showing the coating of NIPAAm nanogel over the SAW IDT.

Table 3.2. Resonance frequency shift observed for the case of SAW IDT humidity sensor for different RH values

RH (%)	Resonance frequency shift (kHz)
17	-272.81
19.9	-273.44
30	-275.69
37	-277.88
40	-280.75

44.5	-282.81
50	-282.25
60.1	-288.36
72	-290.25
81	-292.30
94	-293.25

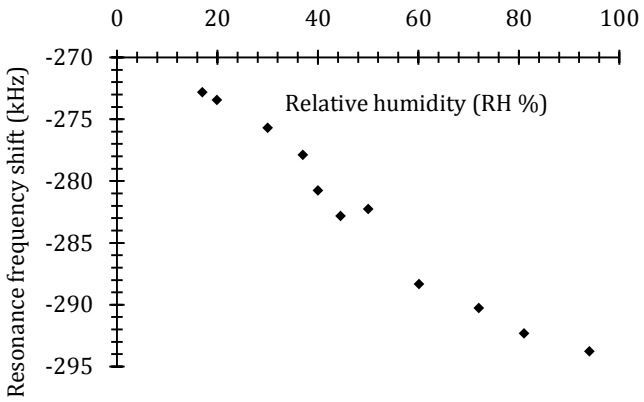

Figure 3.8. Plot of resonance frequency shift versus relative humidity for the case of SAW IDT sensor. A resonance shift of 21 kHz was observed for a RH change of 17 % to 94 %.

3.3 FEM simulation study on mass loading effect of a high aspect ratio structures on SAW devices

Laude *et al*. [55] analyzed a SAW device having IDT made of high aspect ratio fingers, and reported that the high aspect ratio electrodes act as mechanical resonators and their coherent oscillations are coupled by acoustic waves in the substrate. However, the effect of high aspect ratio structures as sensing medium for a SAW resonator sensor has not been reported to the best of our knowledge. We are motivated to study the mass loading effect of high aspect ratio pillars fabricated on SAW devices in place of sensing film. In the simulation, a one-port SAW resonator having a long IDT with infinite number of fingers is considered. It was decided to simulate the mass loading effect of a row of pillars between every adjacent electrodes. The figure 3.9 (a) shows top view of the resonator and figure 3.9 (b) shows the side view of the resonator.

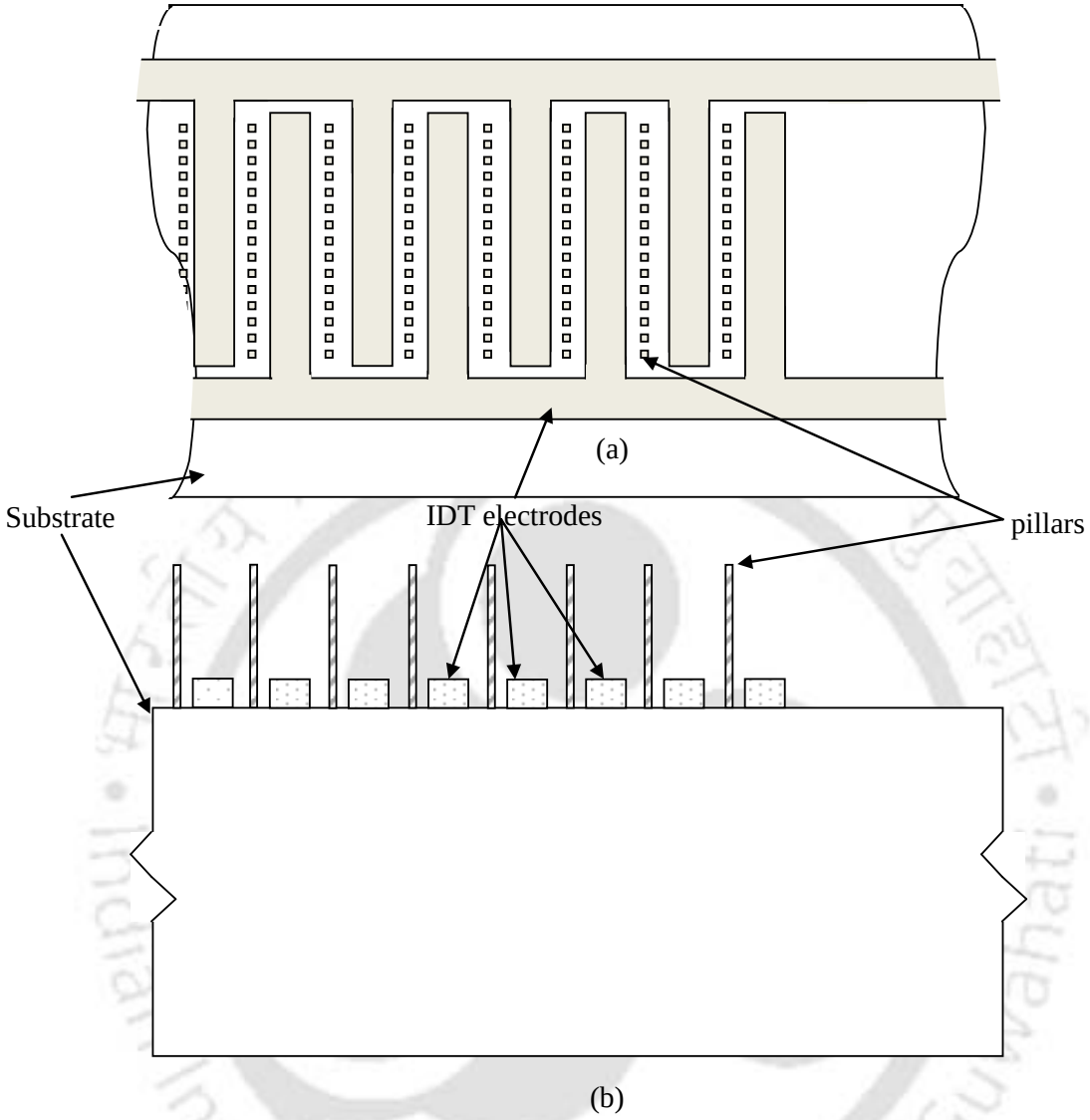

Figure 3.9 (a) Top view of IDT structure with pillars in between their electrodes, (b) A 2D layout showing the side view of (a).

3.3.1. Material and geometry used in simulation

As discussed section 2.5 in chapter 2, FEM simulation of one-port SAW resonator can be performed by considering a segment of SAW IDT structure and providing appropriate boundary conditions. In the simulation to study the mass loading effect of high aspect ratio structure, the geometry of the segment (Figure 3.10) considered for the simulation is chosen to simulate a 100 MHz SAW

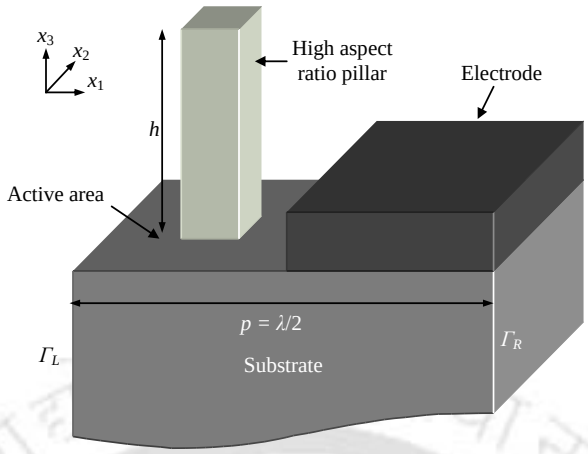

Figure 3.10. SAW resonator geometry considered for the simulation.

resonator. Its dimensions are as follows: electrode width 8.72 μm ($\lambda/4$), pitch (p) 17.44 μm ($\lambda/2$), height of the substrate 174.4 μm (5 λ), and thickness in x_2 direction (aperture) 400 nm, leading to an active area of 0.4 μm × 8.72 μm. Y cut Z lithium niobate substrate is used and its elastic constants, permittivity constants, stress constants are taken from Warner *et al.* [43]. The bottom surface is fixed. The degrees of freedom of the right periodic boundary (Γ_R) are set to be negative of those from the left periodic boundary (Γ_L) (see figure 3.10).[42]

3.3.2 Simulation procedure

The simulation of the SAW resonator is carried out using the piezoelectric module and SPOOLES solver of COMSOL Multiphysics [33]. The simulation is performed in two stages. In the first stage, the eigen frequency analysis is performed for the SAW resonator without the pillar structure and resonance frequency ($f_o|_{h=0}$) is found to be 97.5308 MHz. In the second stage, the eigen frequency analysis is performed for the SAW resonator with a high aspect ratio pillar placed in the middle of the active area as shown in figure 3.10. The pillar has the dimensions of 200 nm × 200 nm × 900 nm, Young's modulus of 99.4 GPa and density of 12020 kg/m^3. The height of the pillar is varied and the corresponding resonance frequency f_r of the SAW resonator with the pillar structure attached is recorded.

3.3.3 Effect of pillar resonance

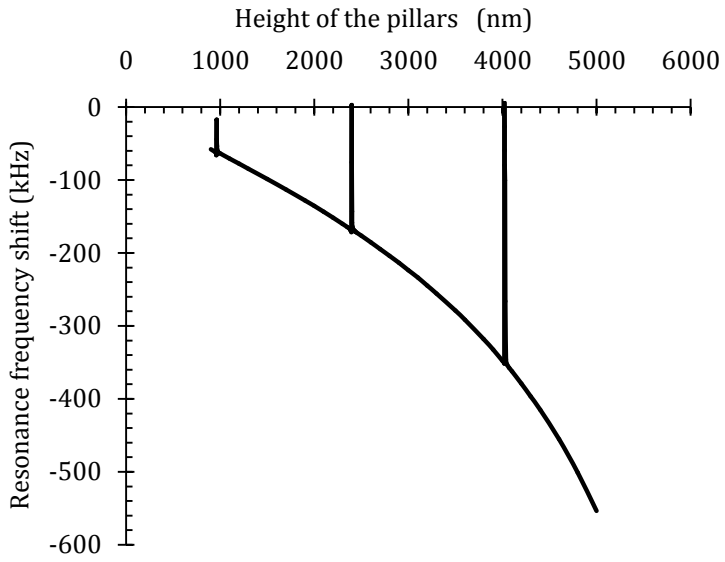

Figure 3.11. Resonance frequency shift of the SAW resonator versus height of the pillars with a cross-section of 200 nm × 200 nm. Plot for the first three resonance modes of the pillar structure is shown.

The simulation is performed for different heights of the pillar varying from 900 nm to 5000 nm and its effect on the resonance frequency f_0 of the SAW resonator with the pillar structure attached is recorded. Figure 3.11 shows the plot of the shift in resonance frequency versus height of the pillars. It is observed that in general the resonance frequency of the SAW resonator decreases for increase in height of the pillars due to increased mass loading. However at certain heights of the pillars, abrupt change in the resonance frequency of the SAW resonator is observed. For example, when the pillar height is 963 nm, 2396 nm, and 4021 nm, the shift in resonance frequency suddenly tends to zero, indicating that the mass loading to the SAW resonator is negligible.

In order to investigate the abrupt change in the resonance frequency observed in figure 3.11, eigen frequency analyses of a pillar for varying heights are performed. Figure 3.12 shows the plot of the resonance frequencies of the pillar versus the height of the pillar. If λ is the wavelength of the acoustic wave in pillar at the resonance frequency (f_r), the height of the pillar that occupies $\lambda/4$, $3\lambda/4$, and $5\lambda/4$ is found to be in the range of 800 nm to 1100 nm, 2000 nm to 2700 nm, and 2800 nm to 4600 nm, respectively. It can be noted from figure 3.11 and figure 3.12 that the extraordinary changes in the resonance frequency shift occur when the pillar height is such that its resonance frequency is close to the SAW resonator frequency (f_o) without pillar structure. For instance, when h = 963 nm, the resonance frequency f_r is approximately equal to f_o. The same phenomenon repeats

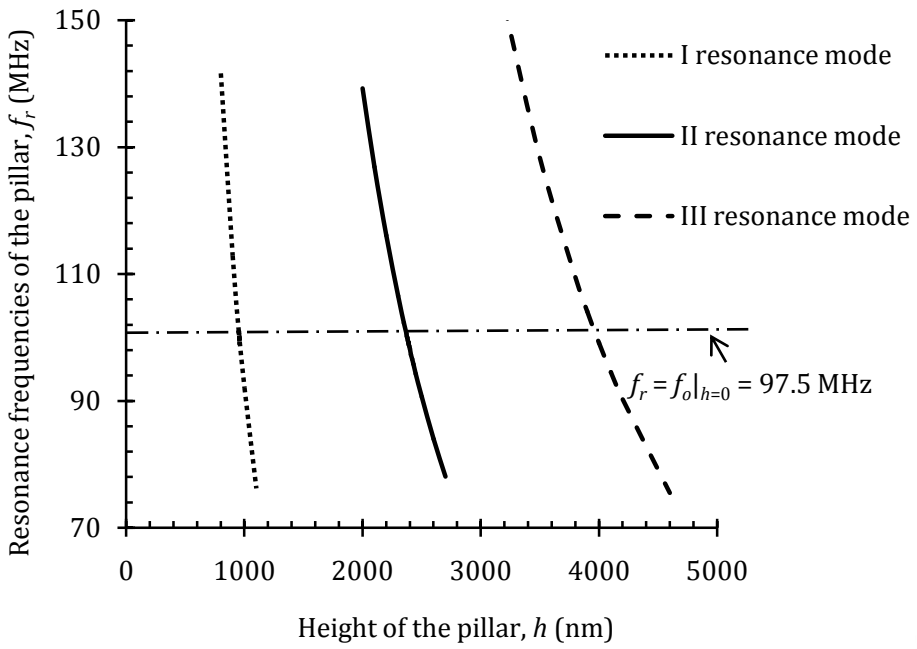

Figure 3. 12. Resonance frequencies of the pillar of cross-section 200 nm x 200 nm versus its height (h). The first resonance mode is shown for h = 800 nm to 1100 nm, the second resonance mode is shown for h = 2000 nm to 2700 nm and the third resonance mode is shown for h = 3200 nm to 4600 nm.

for the second resonance mode and the third resonance mode of the pillar when h = 2396 nm and h = 4021 nm, respectively. For other values of height in the considered range, the resonance frequency shift follows usual mass loading characteristics.

We have considered two more cases of pillar dimensions. The simulation is repeated for a pillar of palladium (E = 128 GPa, ρ = 12020 kg/m^3) with cross-section of 500 nm × 500 nm and 1000 nm × 1000 nm, and from the resonance frequency analysis of the pillar, it is found that the pillar height that occupies $\lambda/4$ (I resonance mode) is in the range of 900 nm to 1700 nm, and 900 nm to 2400 nm, respectively. The plot of the resonance frequency shift versus height of the pillars for the first resonance mode is shown in Figure 3.13. It can be observed that the characteristics are identical to that of the first resonance mode observed in Figure 3.11. It can be noted that at $f_r = f_o|_{h=0}$ the height of the pillar for the case of pillar with cross section 500 nm × 500 is 1545 nm and 1000 nm × 1000 nm is 1999 nm.

The pillars considered in the study have the shape of right square prism. The nth mode resonance frequency f_n of a clamped-free uniform beam is obtained from the simple beam theory as [56]

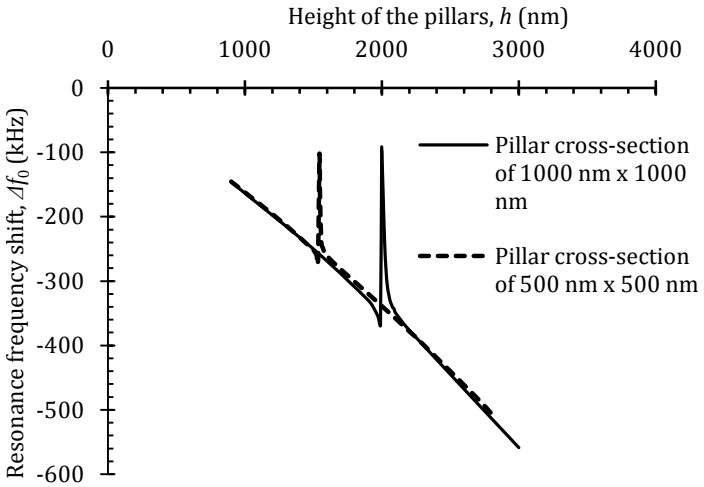

Figure 3.13 Resonance frequency shift of the SAW resonator versus height of the pillars with a cross- section of 1000 nm × 1000 nm and 500 nm × 500 nm. Plot for the first resonance mode of the pillars is shown.

$$f_n = \frac{\beta_n^2}{2\pi}\sqrt{\frac{E\,I}{m_p\,h^4}} \tag{43}$$

where β_n is the resonance mode constant, E is the Young's modulus of the pillar, and I is the cross-section moment of inertia, m_p is the mass per unit length and h is the height of the pillar. The values of β_n for the first four resonance modes are 1.875, 4.694, 7.855, and 10.996.

3.4. Mass loading effect of large number of high aspect ratio pillars attached to SAW resonator

We extended FEM simulation study of a SAW resonator with a large number of high aspect ratio pillars attached like cantilever between the fingers of the IDT to apply mass loading.

3.4.1. Simulation setup

The geometry of the segment (Figure 3.14) considered for the simulation is chosen to simulate a 871 MHz SAW resonator. Its dimensions are as follows: electrode width 1 μm, pitch (p) 2 μm, height of the substrate 10 μm, and thickness in x_2 direction (aperture) 16 nm, leading to an active area of 16 nm × 1 μm. Y cut Z lithium niobate substrate is used and its elastic constants, permittivity constants, stress constants are taken from Warner *et al*. [43]. The bottom surface is fixed. 3D simulations are performed with plane strain conditions. It is possible by modeling a thin strip of

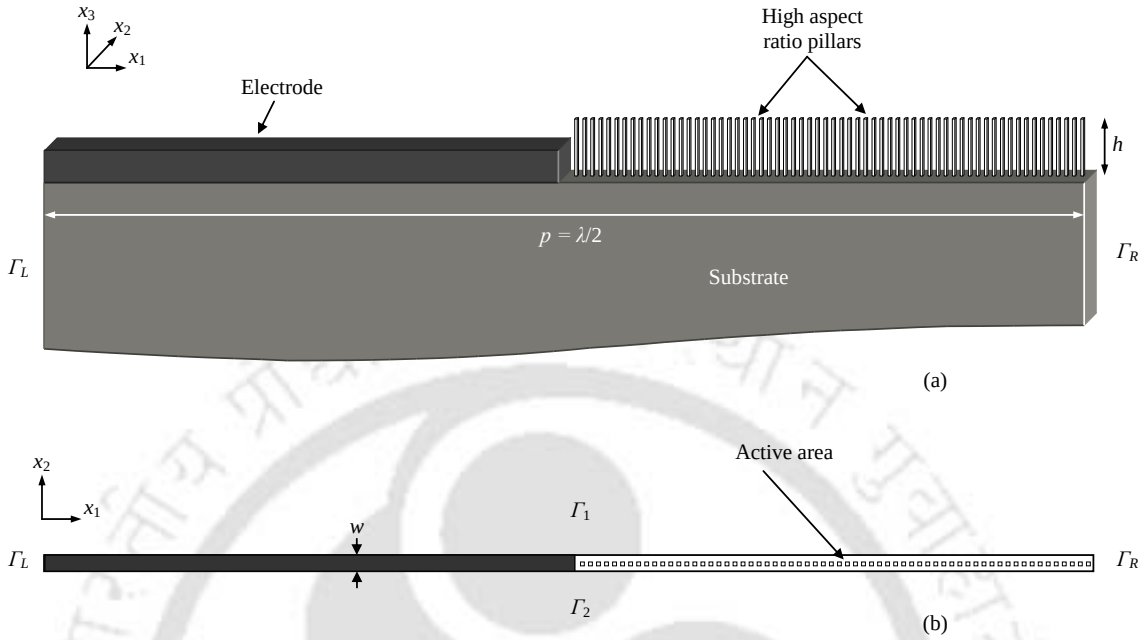

Figure 3.14. (a) SAW resonator geometry considered for the simulation, (b) Top view showing the boundaries.

thickness of w in x_2 direction, cut out from the SAW device, and applying zero displacement constraint in the x_2 direction on the boundaries Γ_1 and Γ_2 (see Figure 3.14). It is valid in the case of Rayleigh SAW as it has no variation and the displacement vectors have no component in x_2 direction.[15] The degrees of freedom of the right periodic boundary (Γ_R) are set to be negative of those from the left periodic boundary (Γ_L) [42](see Figure 3.14). The displacement constraints of the pillar boundaries are set 'free' except for the bottom surface which is attached to the active area of the substrate. Triangular mesh is applied for the pillars and the substrate near the top surface (See figure 3.15). Each mesh element has a minimum dimension of the order of 3 nm. The rest of the SAW resonator is meshed with rectangular mesh with dimension in the order of 0.5 μm × 0.25 μm. The number of degrees of freedom solved is of the order of 12×10^4. The mesh parameters have been chosen for satisfactory resolution within the capability of the software and computer.

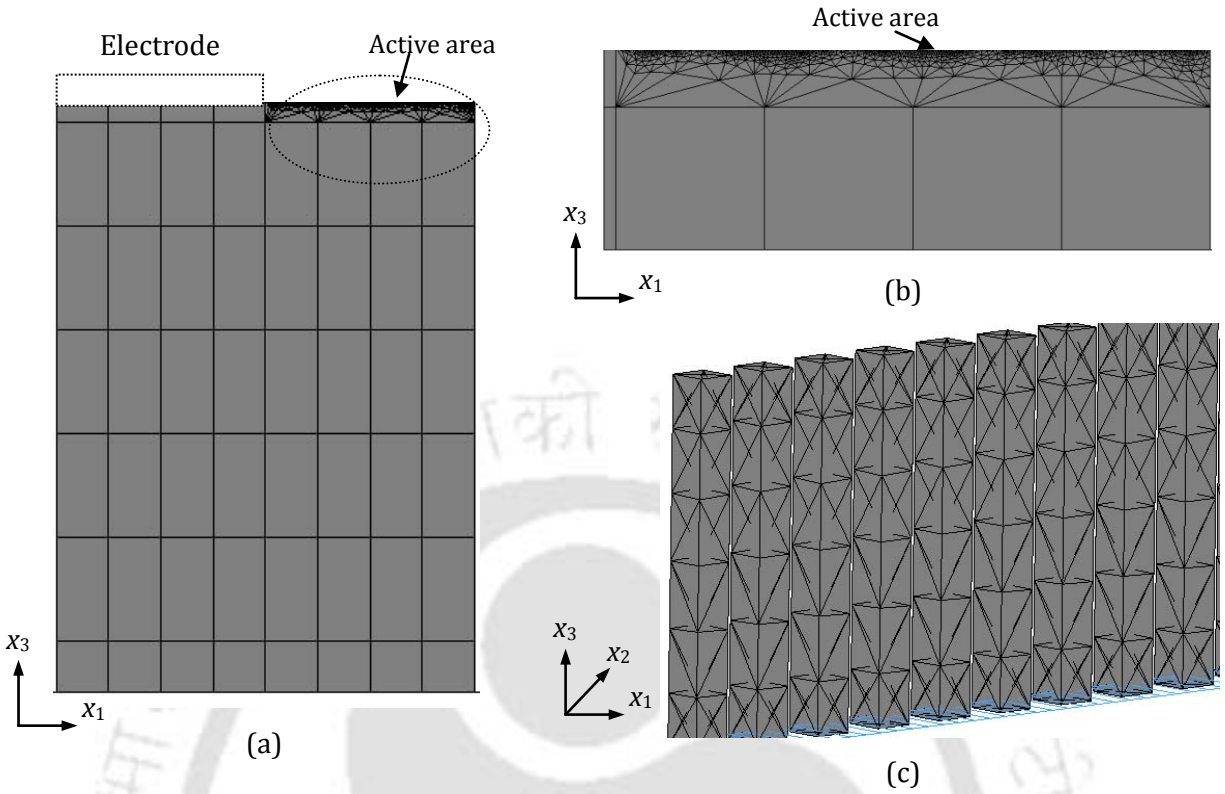

Figure 3.15. Mesh pictures of the structures employed in the simulation model (a) A portion of SAW resonator showing the quality of mesh, (b) A portion of active area showing dense mesh applied to its surface, and (c) A portion from array of pillars showing mesh applied to their surface.

3.4.2. Simulation procedure, results and discussions

The simulation is performed in two stages. In the first stage, the eigen frequency analysis is performed for the SAW resonator without the pillars and the resonance frequency ($f_0|_{h=0}$) is found to be 850 MHz. The total displacement profile of SAW resonator at $f_0|_{h=0}$ is shown in figure 3.16. For simplicity, substrate depth of 2.5 λ along x_3 direction is shown. Total displacements of SAW is calculated by equation, Total displacement $= \sqrt{|u_1|^2 + |u_2|^2 + |u_3|^2}$, where u_1, u_2, and u_3 are the particle displacement in x_1, x_2, and x_3 directions, respectively. In the second stage, the eigen frequency analysis and frequency response analysis are performed for the SAW resonator with 64 high aspect ratio pillars having suitable dimension placed in the middle of the active area as shown in figure 3.14. The pillars have the dimensions of 8 nm × 8 nm × h, Young's modulus of 128 GPa, and density of 12020 kg/m^3. In the simulation, h is varied from 10 nm to 350 nm. The eigen frequency analysis gives resonance frequency modes of the pillars coupled to the SAW device substrate in addition to f_o. Figure 3.17shows the plot of resonance frequencies of the pillars versus the height of the pillar. The figure shows three resonance modes for the range of 10 nm to 350 nm height. If λ is

the wavelength of the resonance frequency, the height of the pillar that occupies $\lambda/4$, $3\lambda/4$, and $5\lambda/4$ is found to be in the range of 60 nm – 100 nm, 150 nm – 200 nm, and 260 nm – 350 nm, respectively. The obtained curves are in agreement with the resonance mode curves observed by Laude *et al* [55] in their experimental study of a SAW device consisting of high aspect ratio IDT structures. However, in our simulation we noticed small variations in f_o, e.g. for the range of 10 nm to 350 nm height of the pillars, f_o decreases by about 40 MHz while the first resonance mode frequency of the pillar decreases by about 1100 MHz. It is apparent, as the height of the pillar increases the mass loading on the device also increases and leads to decrease in f_o.

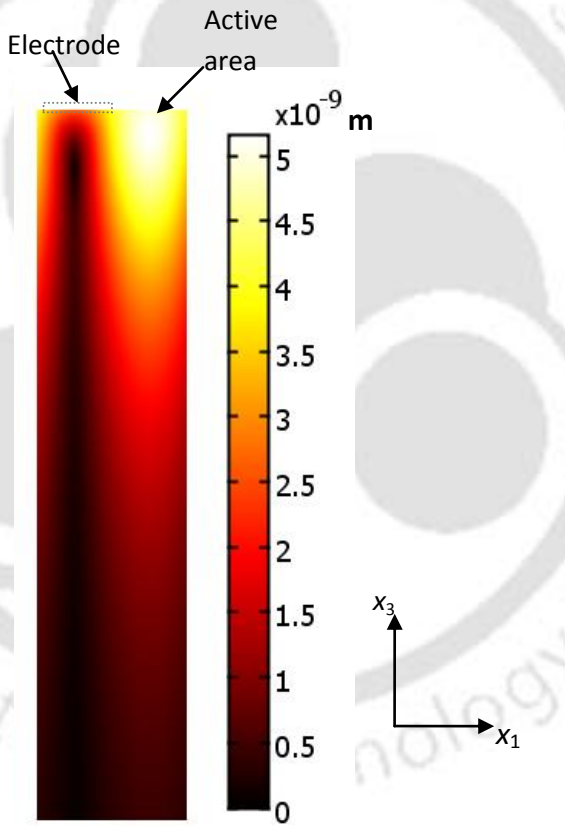

Figure 3.16. Total displacement in the substrate for the SAW resonator without the pillars observed at the resonance frequency.

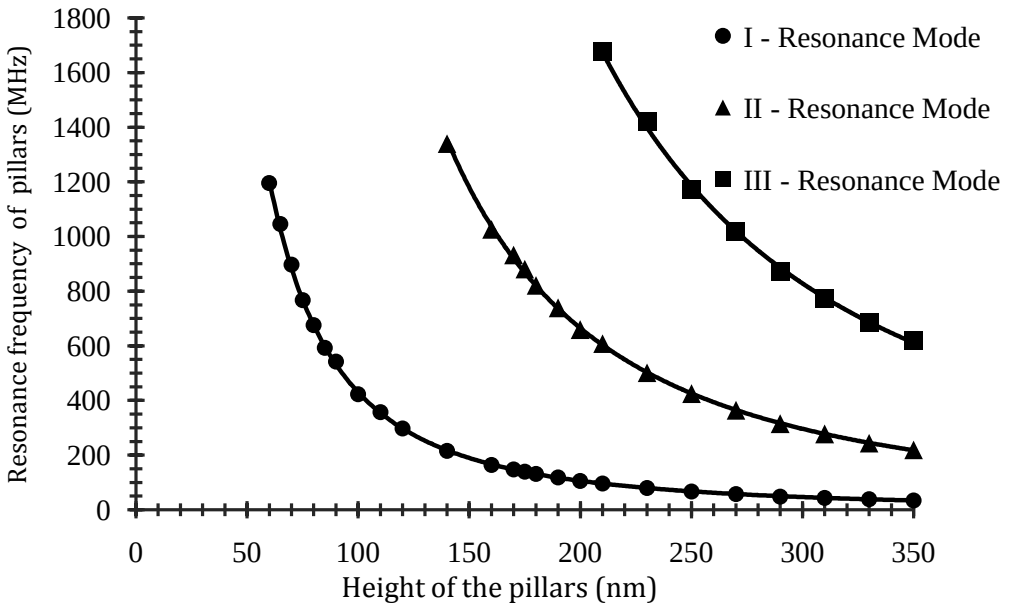

Figure 3.17. The plot of resonance frequency of pillars versus height (h) shows three resonance modes of the pillars for the cross-section of 8 nm × 8 nm. Note that the resonance frequency of the SAW resonator without the pillars is 850 MHz.

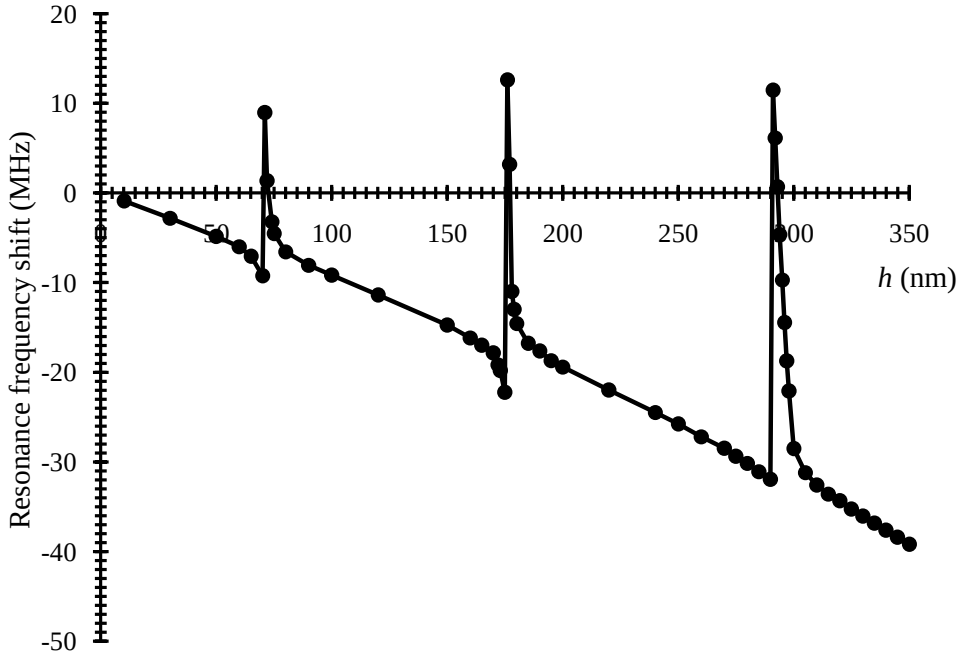

Figure 3.18. Shift in f_o from the reference of $f_o|_{h=0}$ versus height of the pillars. Plot for the first three resonance modes of the pillars is shown.

Figure 3.18 shows the plot of the shift in f_o from the reference of $f_o|_{h=0}$ versus height of the pillars (h). The plot on the whole shows decrease in f_o for increase in height of the pillars due to increasing mass loading. However at certain heights of the pillars, abrupt change in f_o is observed. For example, at the height of 71 nm, 177 nm, and 291 nm, the shift in f_o suddenly tends to zero which is equivalent to negligible mass loading to the SAW resonator. It can be noted from figure 3.17 and figure 3.18 that the extraordinary changes in the shift in f_o occur when the height of the pillars is such that their resonance frequency is close to the SAW resonator frequency without pillars ($f_0|_{h=0}$). For instance, when h = 71 nm, f_o is approximately equal to 850 MHz. The same phenomenon repeats for the second resonance mode and the third resonance mode of the pillar when h = 177 nm and h = 291 nm, respectively. The reason for the positive shift in f_o in figure 3.18 is discussed in chapter 5. For other values of height in the considered range, the shift in resonance frequency follows usual mass loading characteristics. The displacement contours at the active area of the substrate are shown in figure 3.19. The total displacement profiles for the pillar heights of 50 nm, 65 nm, 71 nm, and 120 nm at f_o are shown in Figure 3.19 a-d, respectively. The part of the active area shown consists of 3 pillars and the footprints of the pillars are shown in square boxes. The deformation of the surface due to the pillars can be calculated from the difference of the maximum and minimum displacements of the pillars over it. It can be observed that the deformation of the pillars of height 71 nm (resonance condition) is greater than 3 times that of other cases, which can be noted by distinct alternative occurrences of maximum and minimum displacements at the edges of the pillars.

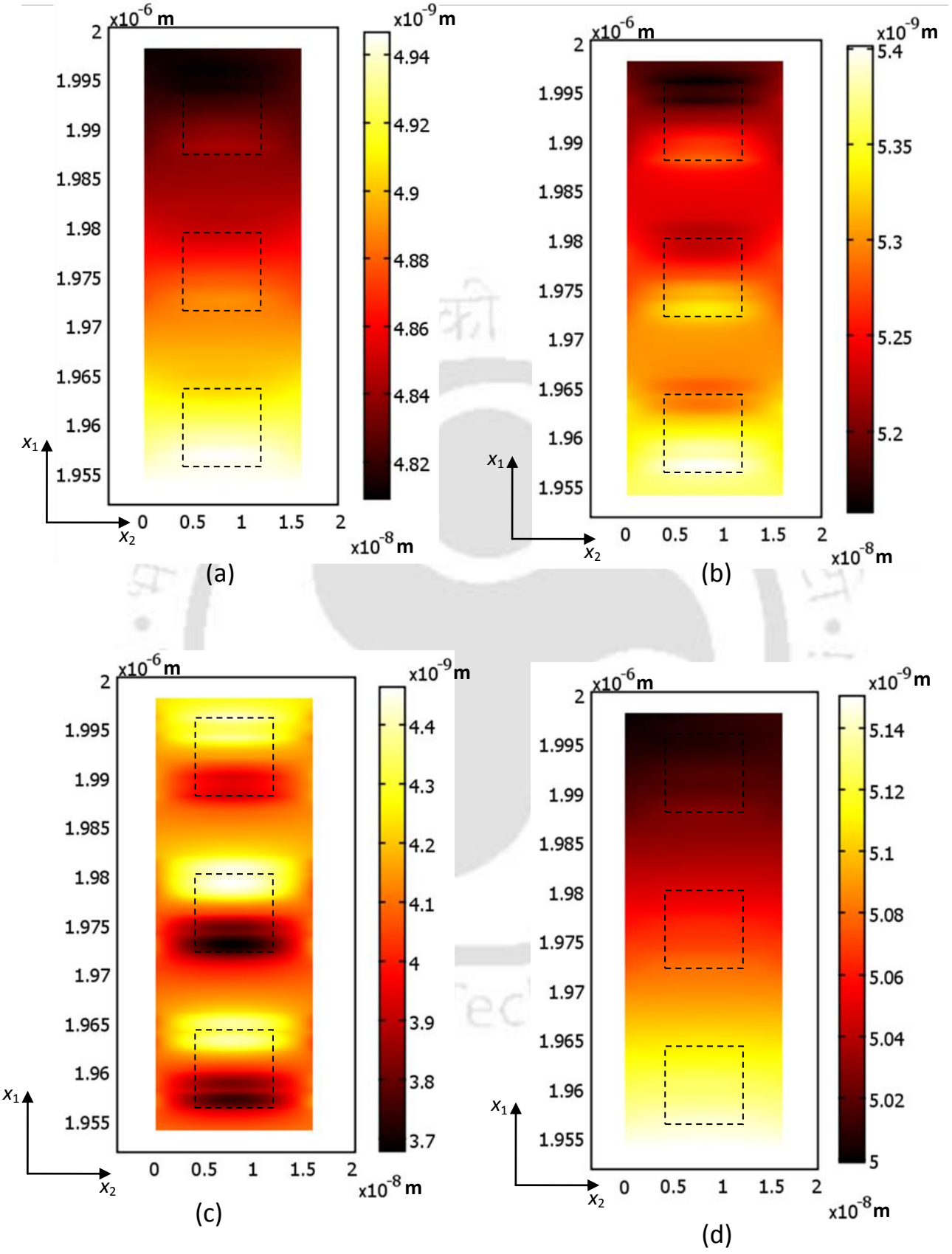

Figure 3.19. Total displacement at f_o at the surface of active area with the pillars of height (a) 50 nm (b) 65 nm (c) 71 nm and (d) 130 nm. The active area of length 44 nm consisting of 3 pillars is shown. The contact surfaces of the pillars are shown as square boxes.

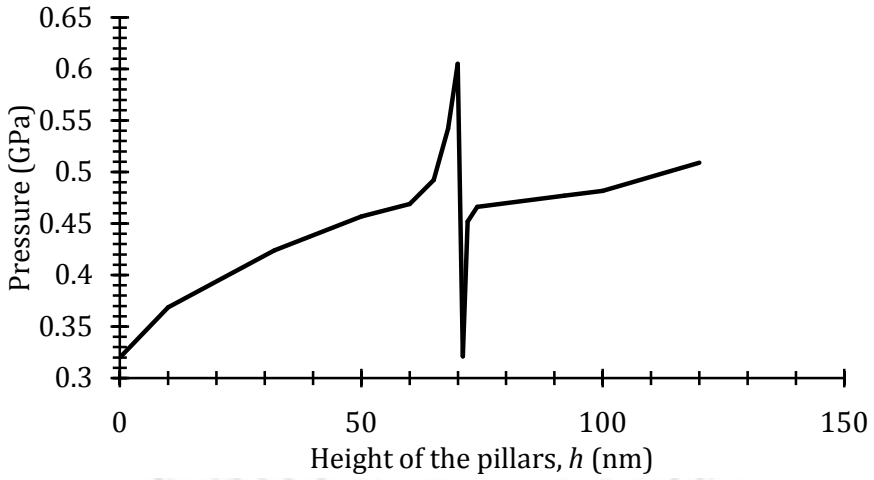

Figure 3. 20. The plot of average pressure at f_o, at the active area on the substrate, versus height of the pillars.

In order to investigate the effect of the resonating pillars on f_o, the average pressure along the surface of the active area is obtained. Figure 3.20 shows the plot of average pressure at f_o, at the active area on the substrate for different values of h. It can be observed that the average pressure increases as the height of the pillars increases. However at 71 nm, the pressure suddenly drops to about 0.35 GPa which is equal to that without pillars and consequently f_o approaches $f_o|_{h=0}$. The pressure alters the wavelength and velocity of the SAW, [57] resulting in shift in resonance frequency. The variations in average pressure in figure 3.20 explain the shift in f_o plotted in figure 3.18. In order to study the pressure wave at the active area of the SAW resonator when the pillars resonate with the SAW resonator, time domain analysis is performed for four cases of pillar heights viz., h = 0 nm, 72 nm, 74 nm and 120 nm. The pressure of at the active area is recorded at a single point under one of the pillar. Figure 3.21 shows the recorded pressure versus time. It can be seen from figure 3.21(a) that the envelope of the curve is showing resonating action of the resonator due to zero mass loading as there are no pillars attached to the substrate. While figure 3.21(b) shows pressure plot for pillars of height 71 nm which is a positive frequency shift condition, it can be observed that curve has a constant envelope indicating the resonance frequencies of the SAW resonator and the pillars are in unison. For the case of pillar height of 74 nm, the pillars exert a resonance frequency closer to SAW resonator frequency and their pressure plot as shown in figure 3.21(c) indicates existence of beat frequency. However for the case of pillar height of 120 nm, the pillars resonance frequency is far away from the SAW resonator frequency and their pressure plot as shown in figure 3.21(d) indicates there no significant effect of pillars to the SAW resonator substrate.

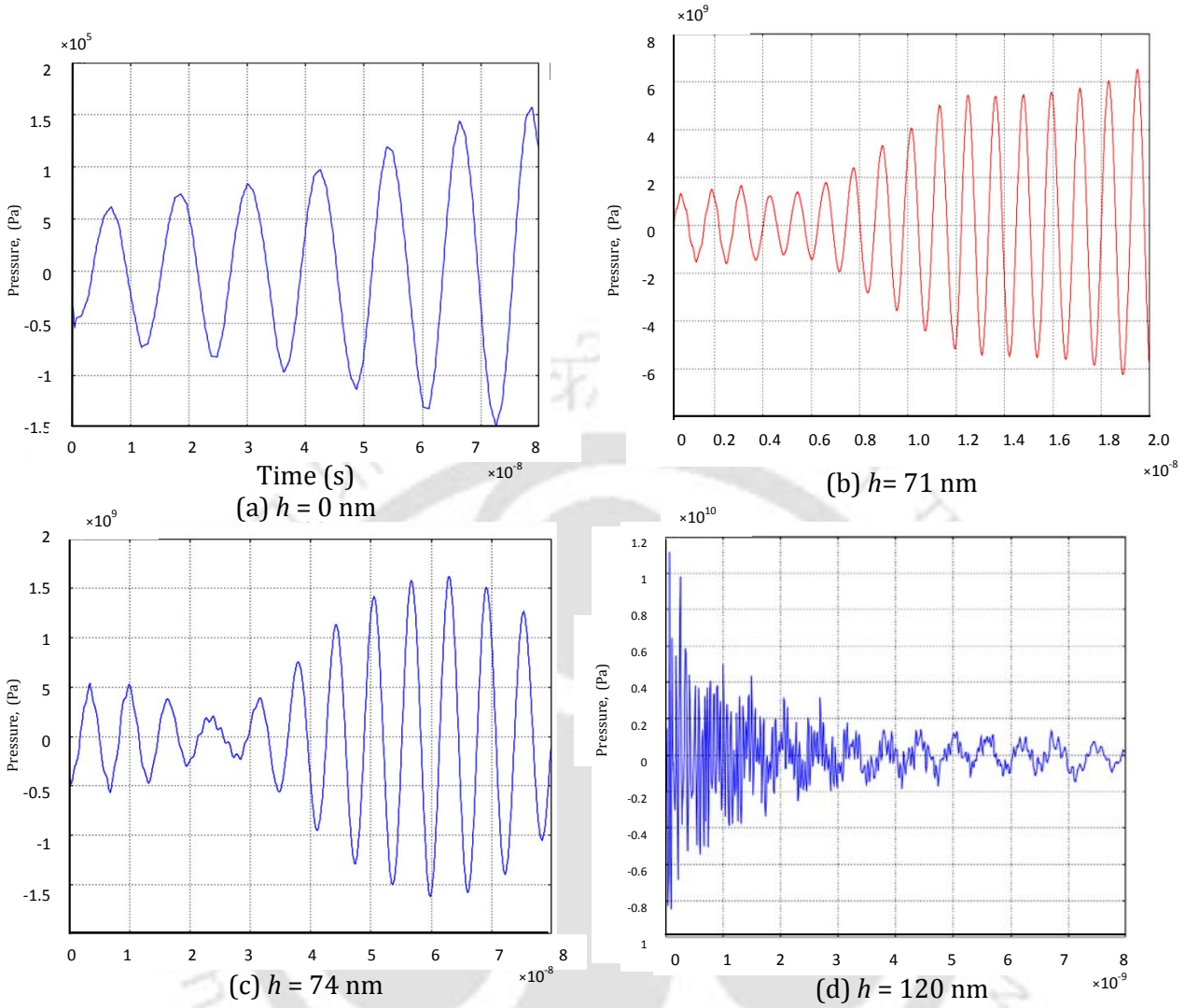

Figure 3.21. Plots of pressure versus time recorded at point on the active area of the substrate under a pillar for the pillar heights of (a) 0 nm (b) 71 nm (c) 74 nm and (d) 120 nm.

Further frequency response analysis is performed for pillars of height 70.6 nm, 72 nm, 73 nm and 74 nm which are closer to the resonant length of 71 nm. Figure 3.22 shows the plots of frequency versus admittance for the four cases of heights. It can be seen that there are additional resonance frequencies at 880 MHz, 820 MHz, 800 MHz and 780 MHz for the heights 70.6 nm, 72 nm, 73 nm and 74 nm, respectively, apart from the original SAW resonator frequency, which is a similar observation reported by Laude *et al*. [55].

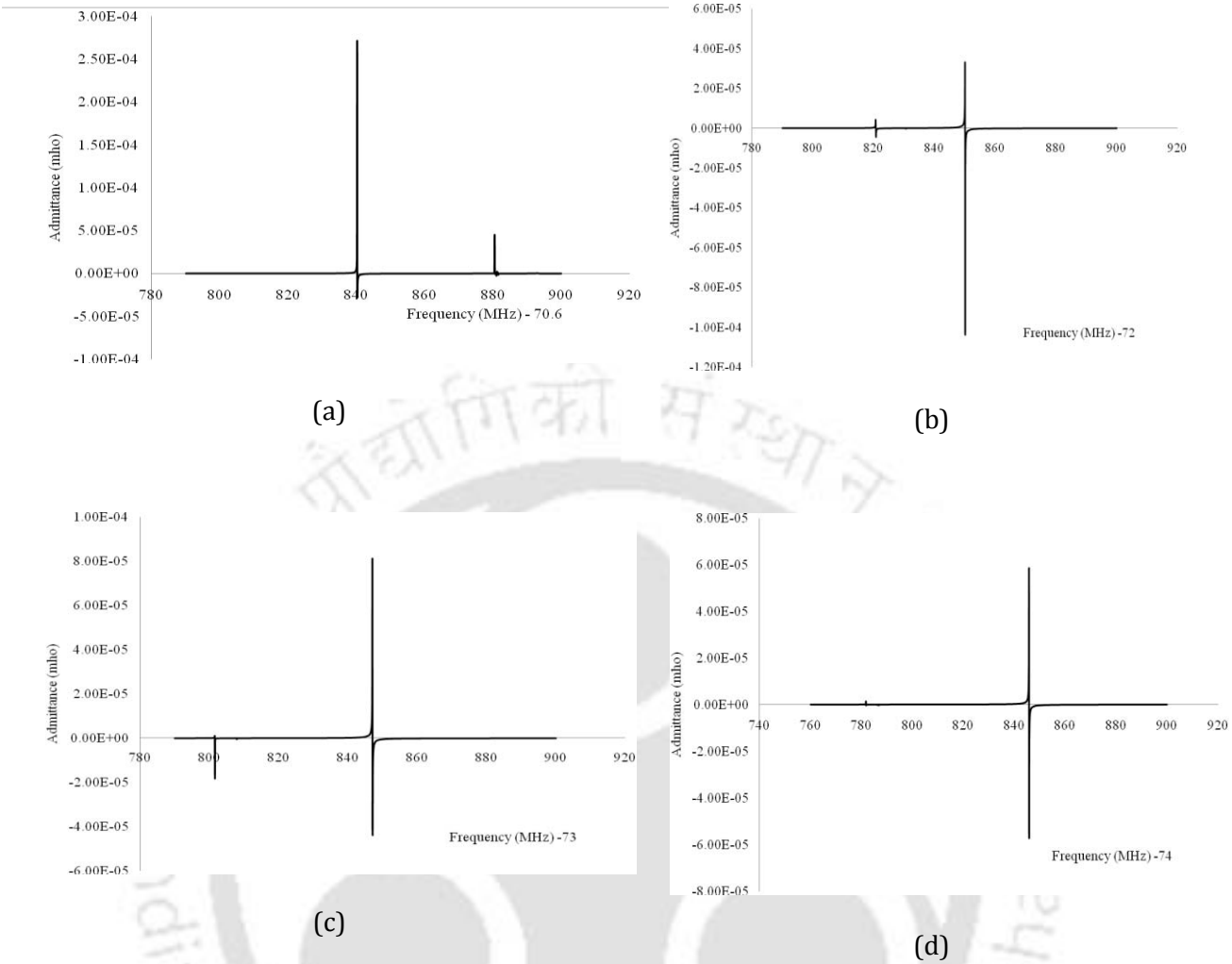

Figure 3.22 (a)-(d). Plot of frequency versus admittance for h = 70.6 nm, 72 nm, 73 nm and 74 nm of the pillars. It can be observed there are additional resonance frequencies at 880 MHz, 820 MHz, 800 MHz and 780 MHz respectively apart from the original SAW resonator frequency.

3.3. Finite element method simulation of a surface acoustic wave hydrogen sensor with palladium nano-pillars as sensing medium

Surface acoustic wave (SAW) devices with palladium thin films and palladium nanowires as sensing medium are reported in hydrogen sensing applications. Hydrogen absorption and desorption by the palladium sensing medium introduce change in mass loading to the acoustic path and cause change in velocity of the SAW. This change in velocity of the SAW is measured as a phase-shift in the electrical signal [4]. Bi-layer films consisting of nickel phthalocyanine and palladium are used in SAW delay line system to sense hydrogen [58]. Yamanaka *et al*. [59] used palladium thin film in spherical ball SAW device and claimed higher sensitivity in detecting

hydrogen. It has been reported that on formation of 'nanogaps' in palladium nano and meso wires in the presence of hydrogen changes resistance of the wire. Im *et al*. [60] worked on a single palladium nanowire of diameter between 70 nm to 85 nm and measured change in resistance of wire is measured for change in concentration of hydrogen. Arrays of palladium mesoscopic wires of diameter in the range of 150 nm are developed using electro-deposition method and employed for detecting hydrogen [61]. Hydrogen sensors and hydrogen activated switches using palladium meso wires are reported by Favier *et al*. [62]. Nanomechanical hydrogen sensors are developed based on resonance frequency shift of an AuPd alloy nano beams [63]. Most of the reports on hydrogen gas sensing are based on change in the conductivity of the sensing medium rather than mass, as the mass of hydrogen molecule is less than many other molecules. In practical and commercial sensors palladium is mostly used as a catalyst. Sadek *et al*. [64] fabricated SAW gas sensor based on change in conductivity of sensing medium made of ZnO nanorods for detecting hydrogen at 200 °C to 300 °C. Bhenthanabotla *et al*. [65] used palladium nanowires in SAW delay line sensor and detected hydrogen concentration of 6 %. Huang *et al*. [66] used platinum coated ZnO nanorods as sensing medium in SAW RFID tags and developed a wireless SAW hydrogen sensor. Finite element method (FEM) simulation of SAW hydrogen sensor is used to visualize the SAW sensor response and to optimize the performance of the sensor. Ippolito *et al*. [38] performed FEM simulation of a two-port delay line SAW device with ZnO guiding layer and investigated on electromagnetic feed-through in layered SAW devices. Researchers have demonstrated the 3D FEM simulation of SAW hydrogen sensors using ANSYS, and to reflect the presence of hydrogen, the change in material properties of palladium are provided to the selective coating of palladium over the SAW delay line [67],[36].

The proposed design differs from other SAW hydrogen sensors, and uses vertically grown palladium nano-pillar structures attached as sensing medium between the fingers of SAW resonators to produce change in mass loading in the presence of hydrogen. In general, mass loading due to the structures grown over the surface of the SAW resonator leads to shift in f_o. As described in section 3.2, when the resonance frequency of the pillars is close to the SAW resonator frequency without pillars, the shift in f_o tends to zero. When the dimensions of the pillars are chosen such that they resonate at the resonance frequency of the SAW resonator, the pillars offer negligible mass loading to SAW. Further any change in the dimension or material property of the pillars will alter their resonance frequency and introduce significant mass loading to the resonator. Thus we have been motivated to simulate a hydrogen sensor by considering palladium pillars grown normal to the surface of the SAW resonator such that their resonance frequency is close to the resonance

frequency of the SAW resonator. A small change in the resonance frequency of the attached structure will lead to great shift in f_o. Accordingly, high sensitivity SAW hydrogen sensors can be developed. The material properties of palladium pillar are varied equivalent to that of absorption and desorption of hydrogen. Eigen frequency analysis of the SAW resonator is observed for presence of 0 % to 3 % of hydrogen. The sensitivity of SAW sensor is examined for small concentration of hydrogen.

3.3.1. Geometry, material properties and boundary conditions

The geometry of the segment (figure 3.23) considered for the simulation has dimensions as follows: electrode width 1 μm, pitch (p) 2 μm, height of the substrate 20 μm, and thickness in x_2 direction (aperture) 125 nm, leading to an active area of 125 nm × 1000 nm from equation (1), the resonance frequency of SAW resonator is 872 MHz. Y cut Z lithium niobate substrate is used and its elastic constants, permittivity constants, stress constants are taken from Warner *et al*. [43]. 3D simulations are performed with plane strain conditions. The bottom surface is fixed. The degrees of freedom of

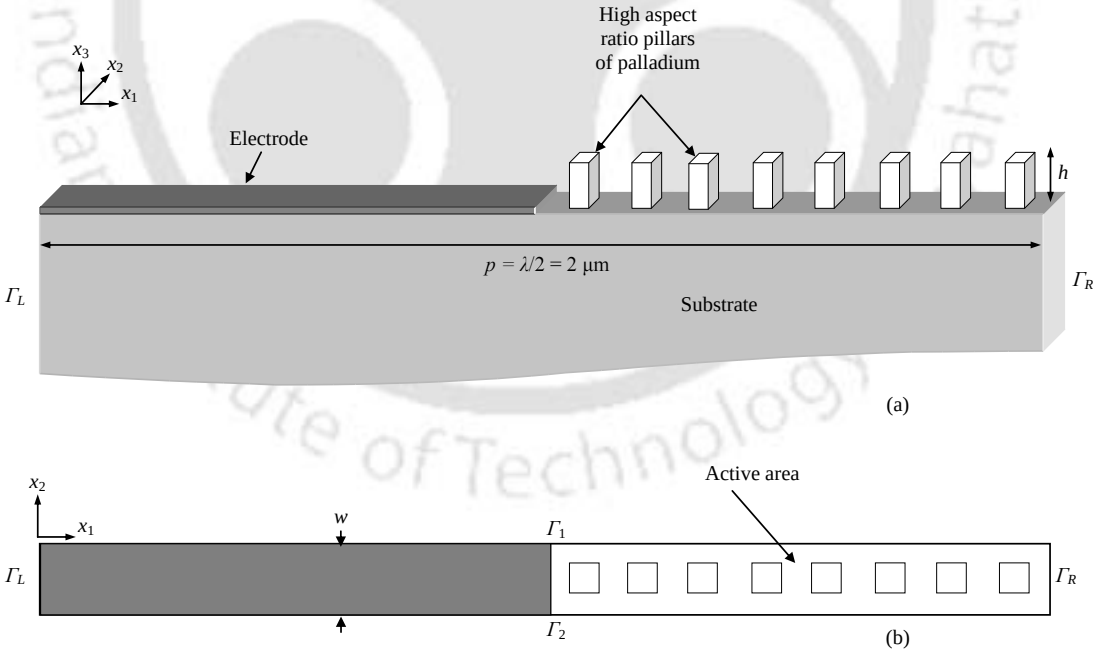

Figure 3.23 (a) SAW resonator geometry considered for the simulation of hydrogen sensor using palladium pillars with cross-section of 62 nm × 62 nm, (b) Top view showing the boundaries.

the right periodic boundary (Γ_R) are set to be negative of those from the left periodic boundary (Γ_L) (see figure 3.23).

3.3.2. Simulation procedure

High density mesh is applied to the surface of the resonator and pillars. Triangular mesh is applied to the upper part of the substrate and mesh size of the triangular mesh is 4 nm. Triangular mesh with maximum mesh size of 15 nm is applied for the pillars. The simulation is performed in three stages. The degrees of freedom (DOF) solved are displacements along x_1, x_2, and x_3 directions (see figure 3.23), and voltage. Over 200,000 DOF are solved in each iteration. In the first stage, the eigen frequency analysis is performed for the SAW resonator without the pillar structure and the resonance frequency (f_o) of the SAW resonator is found. In the second stage, the eigen frequency analysis is performed for the SAW resonator with a high aspect ratio nano-pillars of palladium placed in the middle of the active area as shown in figure 3.23. As a typical case, eight such nano-pillars are placed for every period of SAW resonator. The palladium pillars have the shape of right square prism and cross-section of 62 nm × 62 nm, Young's modulus of 128 GPa and density of 12020 kg/m^3. The displacement constraints are set 'free' as boundary conditions to the pillar except for the bottom surface of the pillar which is attached to the active area of the substrate. The height of the nano-pillars is varied from 0 nm to 300 nm and the corresponding resonance frequency of the SAW resonator with the pillars structure attached is recorded. In the third stage, the SAW resonator with the palladium pillar is considered and presence of various concentrations of hydrogen up to 3 % is simulated. Fabre *et al*. [46] have performed in situ study on change in material properties of palladium metal in the presence of hydrogen. Palladium lattice expands to the insertion of hydrogen and hardens the proton-palladium potential. This behavior induces linear change in young's modulus, density and volume of the palladium metal in the presence of hydrogen as a function of concentration. The material properties of the palladium nano-pillars are modified to simulate the presence of 0 % to 3 % of hydrogen. For example, in the presence of 3 % of hydrogen, the young's modulus of the palladium pillar decreases by 14 %, the density of the pillar decreases by 2.4 % and volume of the pillar increases by 10 %. The changes in material properties are within ± 20 % error limit [46]. The eigen frequency analysis of the SAW resonator is performed and the resonance frequency of the SAW resonator is recorded for varying concentration of hydrogen.

3.3.3. Results and discussions

The resonance frequency without pillars ($f_o|_{h=0}$) of the SAW resonator is found to be 850.43 MHz. Figure 3.24 shows the plot of the resonance frequency versus height of the nano-pillars. It is observed that in general for increase in height of the nano-pillar the resonance frequency of the SAW resonator decreases due to increasing mass loading. However at certain heights of the nano-pillars, abrupt change in the resonance frequency of the SAW resonator is observed. For example, at the height of 180 nm the shift in resonance frequency suddenly tends to zero, indicating that the mass loading to the SAW resonator is negligible. The extraordinary changes in the resonance

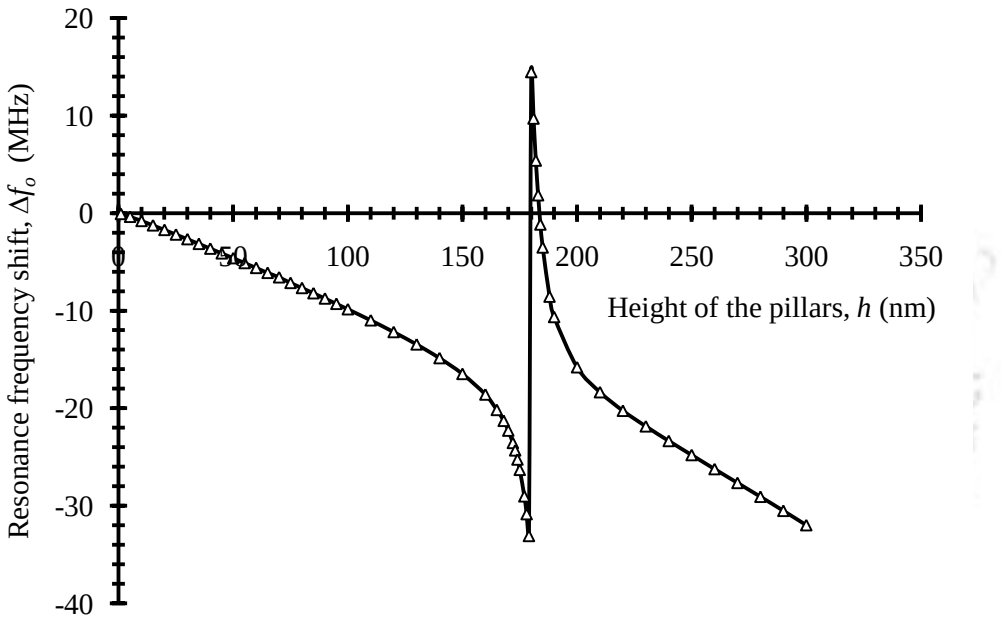

Figure 3.24. Resonance frequency shift in the SAW resonator for different pillar heights. Pillars have a cross-section of 62 nm × 62 nm. The first resonance mode is only shown.

frequency occur when the pillar height is such that its resonance frequency is close to the SAW resonator frequency without pillars ($f_o|_{h=0}$). When h = 180 nm, the resonance frequency f_o is approximately equal to ($f_o|_{h=0}$).

In order to realize hydrogen sensor, palladium nano-pillars of height of 180 nm are considered. As mentioned in the simulation procedure, resonance frequency is recorded for various concentrations of hydrogen. A voltage of 10 V is applied to the electrode in the frequency response analysis performed using parametric solver available in COMSOL Multiphysics. Figure 3.25 shows

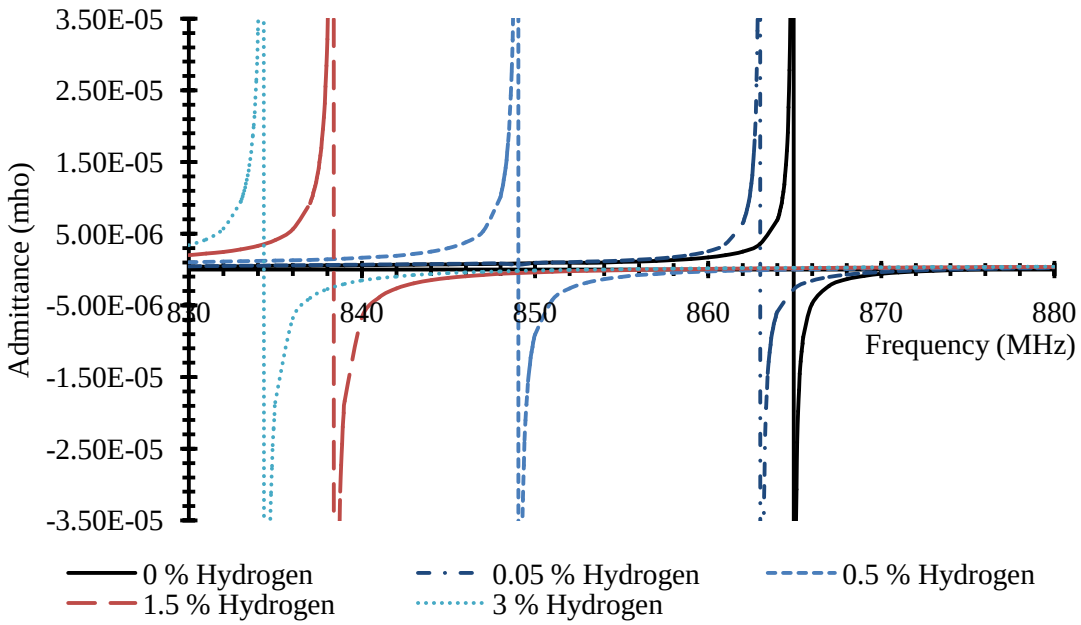

Figure 3.25. Admittance versus frequency plots of SAW resonator with nano-pillars in the presence of 0 %, 0.05 %, 1 %, and 1.5 % of hydrogen. The frequency value for which the admittance curve crosses zero is the resonance frequency.

the plot of admittance versus frequency of the SAW resonator for various concentration of hydrogen. The frequency value for which the admittance is zero is the resonance frequency of the SAW resonator. The resonance frequency of the SAW resonator is found to be 864.9 MHz for 0 % of hydrogen. It is observed that the resonance frequency decreases for increase in hydrogen concentration. For hydrogen concentrations of 0.05 %, 0.5 %, 1.5 %, and 3 %, the shift in resonance frequency (Δf_o) is found to be 1.27 MHz, 14.76 MHz, 25.57 MHz, and 29.83 MHz, respectively. Figure 3.26 shows the plot of resonance frequency shift of SAW resonator for the hydrogen concentration of 0 to 3 %. It can be seen the response shows a linear behavior up to 0.9 % of hydrogen concentration. The sensitivity of the proposed SAW hydrogen sensor consisting of nano-pillars is compared with a similar sensor consisting of a thin film in place of nano-pillars. The frequency response analysis is performed for a SAW hydrogen sensor using palladium thin film as sensing medium for varying concentration of hydrogen. A palladium thin film of dimension 124 nm × 1 μm × 44.64 nm is placed in the active area of the SAW resonator. The dimension of the film is chosen such that it produces equivalent mass loading as 8 pillars of dimension 62 nm × 62 nm × 180 nm. Figure 3.27 shows the plot of resonance frequency shift of SAW resonator for the hydrogen concentration of 0 to 3 % for the case of SAW sensor consisting of palladium thin film. It can be

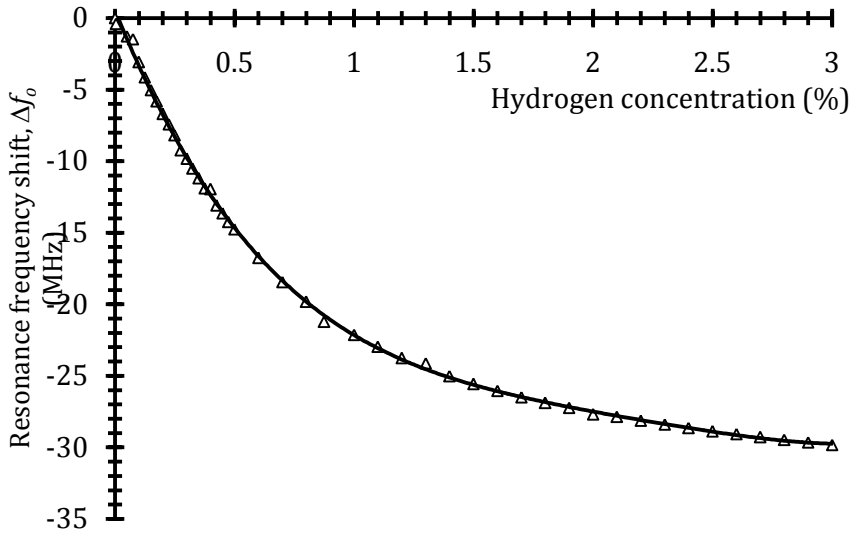

Figure 3.26. Resonance frequency shift versus concentration of hydrogen obtained for the case of SAW sensor consisting of nano-pillars as sensing medium.

observed that for the presence of hydrogen, Δf_o obtained for the case of nano-pillars is at least 10 times greater than Δf_o obtained for the case of thin film. Hence with the proposed design, high sensitive SAW hydrogen sensors can be developed which are suitable for the measurement of small concentration of hydrogen.

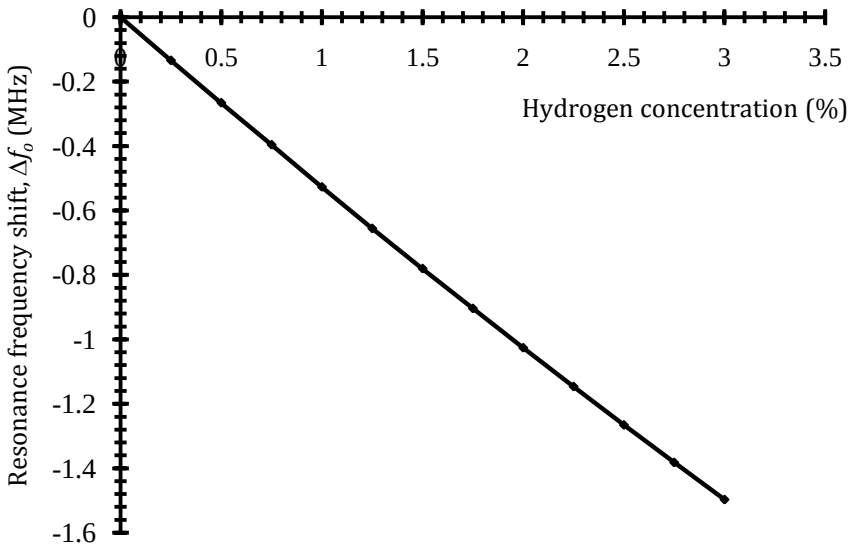

Figure 3.27. Resonance frequency shift versus concentration of hydrogen obtained for the case of SAW sensor consisting of palladium thin film as sensing medium.

3.4. FEM simulation to study sensitivity and significance of size of high aspect ratio pillar sensing medium in SAW sensors

The FEM simulation study of mass loading characteristics of high aspect ratio pillars on SAW resonator is extended to study the significance of cross-section of pillars on sensitivity.

3.4.1. Simulation setup

Similar SAW resonator geometry and boundary conditions explained in section are used for the present simulation study. The mass loading effect due to multiple high aspect ratio structures are

Table 3.3. Different case of pillar dimensions considered for sensitivity study

Case	Cross section of the pillar (nm²)	Active area (nm²) ($x_2 \times x_3$)	Number of pillar	Top view of active area
				x_2, x_1
1	250 × 250	500 × 1000	2	Pillars, w
2	125 ×125	250 × 1000	4	w
3	62 ×62	125 × 1000	8	w
4	31 × 31	62 × 1000	16	w
5	16 × 16	31 × 1000	32	w
6	8 × 8	16 × 1000	64	w

studied in six different cases of cross sections, active area dimension and number of pillars as tabulated in Table 3.3. It was decided to maintain same mass per area and hence the significance of cross-section can be identified accordingly. For example in typical case – 1, two pillars of cross-section 250 × 250 is placed in middle of the active area, hence to simulate the same mass per area of

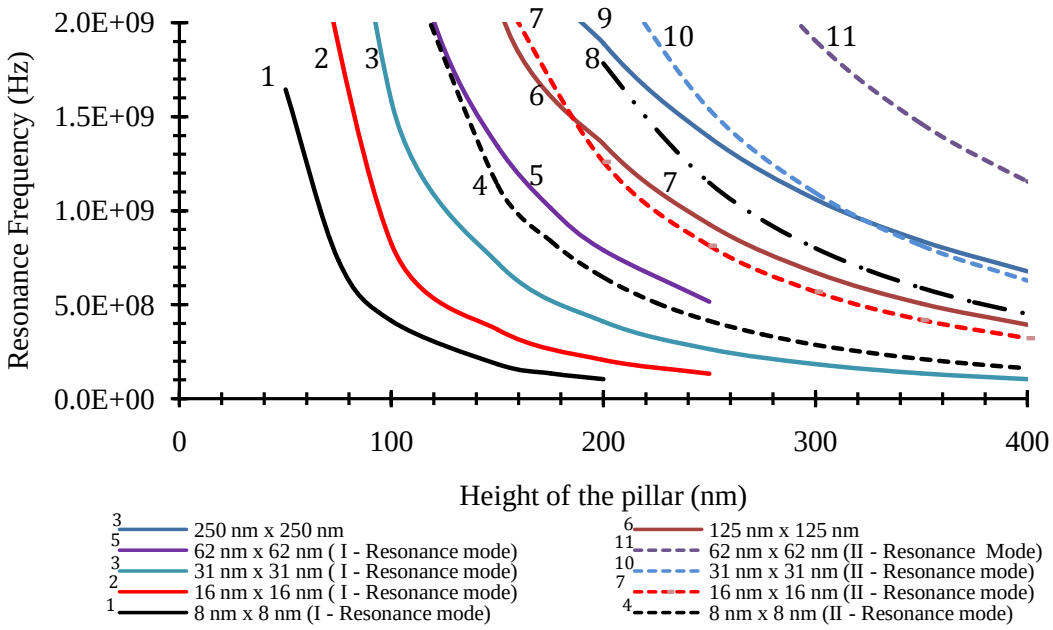

Figure 3.28. Resonance frequencies of the pillar of cross-section consider for the study.

the pillars with cross-section 8 nm × 8 nm, 4096 such pillars are to be placed within the active area of 500 nm × 1000 nm and this increases the mesh elements and subsequently the number of DOF will be beyond the capacity of the computer to solve. Hence it was decided to reduce the size of *w* proportionally with respect to the cross-section of the pillar in each case of study. Initially the resonance frequency of the pillar is identified through FEM simulation. The pillar in each case is considered as a cantilever beam, and resonance frequency is recorded for different heights. Figure 3.28 shows the plot of resonance frequency versus height of the pillar.

3.4.2. Results and discussions

The simulation of SAW resonator with the pillar is performed in two stages. In the first stage, the eigen frequency analysis is performed for the SAW resonator without pillars. In the second stage, the eigen frequency analysis is performed for the SAW resonator with a high aspect ratio palladium pillars placed in the middle of the active area as shown in figure 3.23. Each pillar has Young's modulus of 128 GPa and density of 12020 kg/m^3. The height of the nano-pillars is varied and the corresponding resonance frequency f_r of the SAW resonator with the pillar structure attached is recorded for each case. Figure 3.29(a), (b), (c), (d), (e) and (f) shows the plot of Δf_o versus height, h of pillars for the case 1, case 2, case 3, case 4, case 5, and case 6 respectively. As expected for every case, for increase in mass loading (increase in h) the resonance frequency shift decreases. However

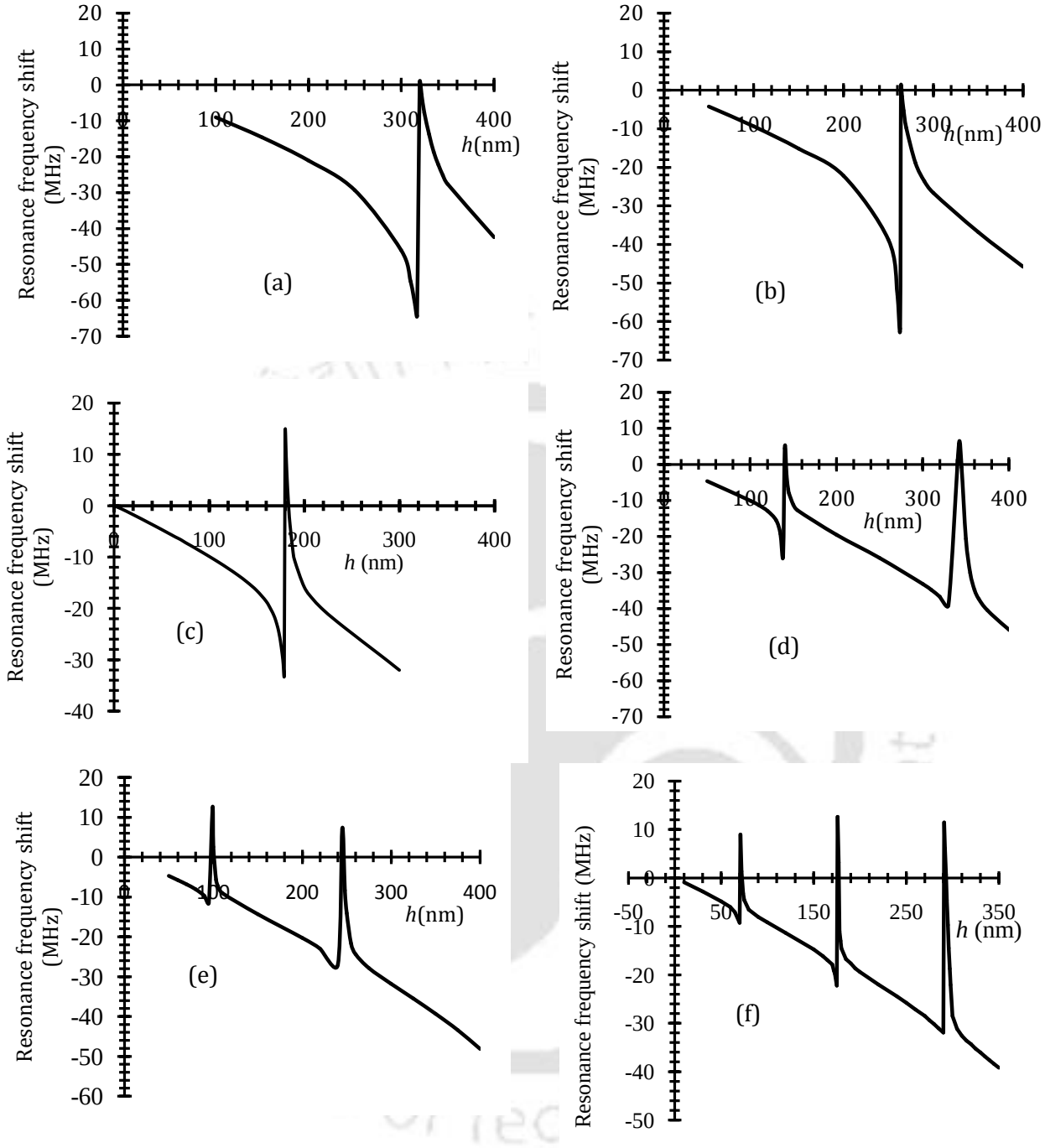

Figure 3.29. Plot of resonance frequency shift versus height of the pillars for (a) case – 1, (b) case – 2, (c) case – 3 , (d) case – 4, (e) case – 5and (d) case – 6 of table 3.1

at resonance heights h = 320 nm , h = 264 nm , h = 180 nm , h = 140 nm , h = 99 nm , and h = 72 nm of the pillar for the case 1, case 2, case 3, case 4, case 5, and case 6 respectively , Δf_0 tends to zero. It can be seen from figure 3.28 that in these heights the resonance frequency of the pillar is close to $f_o|_{h=0}$. Thus if the sensing medium is made of pillars that resonate at $f_o|_{h=0}$, it will offer negligible

mass loading and further small change in properties of material will offer significant change in mass loading to the SAW device and hence high sensitive SAW sensor can be developed. Figure 3.30 shows the maximum sensitivity that can be obtained by using the pillars as sensing medium. The maximum sensitivity is defined as change in f_o for 1 nm increases in height of the pillars at the maximum of the curve in figure 3.29(a)-(e). It can be seen from figure 3.21 that there is a gradual increase in sensitivity for smaller cross-section of the pillar. It was also evident if the pillars are in nano scale cross section has more chance of positive resonance shift at smaller heights. Sensitivity is high at small concentration because slope in figure 3.29 is greater at small concentration.

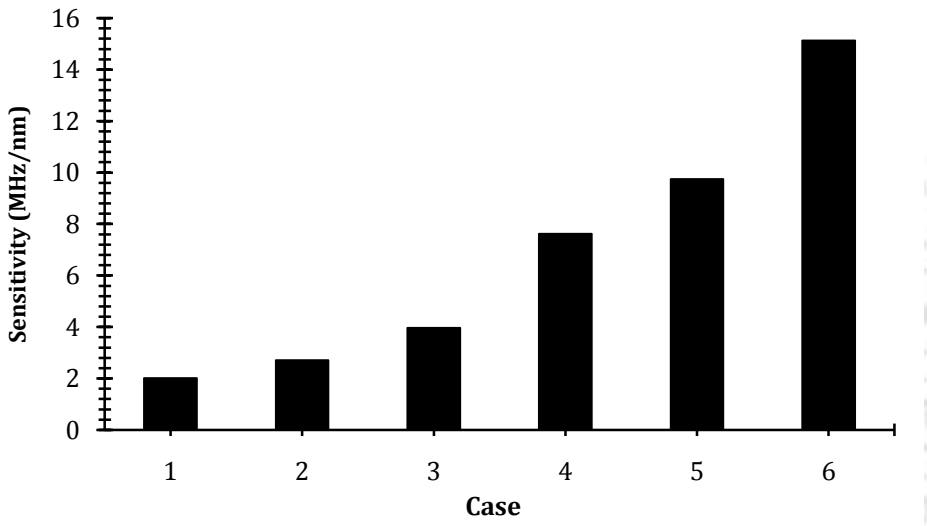

Figure 3.30. Bar graph showing sensitivity obtained for different case mentioned in table 3.1.

3.5. Summary

In this chapter FEM simulation study of mass loading characteristics of high aspect ratio structure attached normal to SAW resonator is discussed. In summary,

An FEM simulation of SAW resonator with high aspect ratio pillars attached between IDT fingers is performed. The effect of mass loading on the resonator frequency due to the varying height of the pillars is studied. It can be concluded that when the resonance frequencies of the pillars are close to $f_0|_{h=0}$ of the SAW resonator, the shift in f_o abruptly tends to zero which is equivalent to negligible mass loading to the SAW resonator. Thus if nano or meso wires are grown normal to the surface of the SAW resonator such that their resonance frequency is equal to $f_o|_{h=0}$, a small change in the resonance frequency of the attached structure will lead to great shift in the resonance frequency of

the resonator. Accordingly, high sensitivity SAW sensors such as gas sensors can be developed, where the absorption of the gas changes the dimensions of the pillars.

A hydrogen sensor has been proposed with palladium nano-pillars as sensing medium grown normal to the substrate of the SAW resonator. The dimensions of the palladium nano-pillars are chosen such that the pillar resonance frequency is equal to the resonance frequency of the SAW resonator. It is observed that the resonance frequency decreases for increase in concentration of hydrogen and the sensitivity is relatively higher for smaller concentration of hydrogen. The proposed SAW resonator with palladium nano-pillar resonant structure can be employed as a high sensitive sensor to detect small concentration of hydrogen.

In the initial part of the chapter mass loading effect of thin film on SAW devices introduced. SAW based relative humidity sensor using thin film made of NIPAam nanogel as sensing medium is developed. The sensor works on principle of mass loading effect, the particles in the film expands in presence of moisture and offer mass loading and it leads in resonance frequency shift of the SAW device. A resonance frequency shift of 32 kHz and 19 kHz was observed for a RH change of 15 % to 81 % for SAW resonator sensor and SAW IDT sensor respectively.

4

Micro Fabrication of SAW Devices and Resonant Structures

In the initial chapters we had discussed the theory and simulation of SAW devices. This chapter deals with the design and fabrication of SAW devices and resonant structures.

4.1 Fabrication of SAW devices

SAW devices can be predominantly built using photolithographic patterning techniques used in the semiconductor industry. There are two processes that are commonly used to pattern IDTs: etching and lift-off. Though both are used for fabricating SAW devices, the Lift-off is more suitable to develop IDT structure of feature size < 5 μm. However the etching process is simpler and easy to realize IDT patterns. In this work etching processes is adopted and the minimum dimension of IDT pattern is of the order of 17 μm. The basic steps involved in fabricating SAW devices are layout design, mask generation, metal deposition over the wafer, photolithography, etching, and wafer dicing.

4.1.1 Design of SAW devices

Important substrate materials used in SAW sensor application and their properties such as k^2 and velocity is listed out in appendix A. The delay line SAW devices and one port SAW resonator are fabricated on lithium niobate substrates. Y-Z lithium niobate wafers and 128 ° Y- X lithium niobate wafers of thickness of 0.5 mm and diameter of 4 inch are procured from Roditi International, U.K. One face of the wafer was mirror polished while the other surface is lapped with #GC1000 [68]. Some of the important criteria to be considered in fabricating the SAW devices for our experiment are as follows,

1. The IDT and reflector structures are designed for the specified resonance frequency and 20 mS admittance. SAW one port resonators with resonance frequency 39 MHz are designed to study the mass loading effects of resonant structures. The desired resonance frequency of the SAW resonator has chosen such that pillars of required resonance frequency can be easily fabricated over it. The parameters of the SAW resonator are designed from P- Matrix model described in chapter 2. Figure 4.1 shows the SAW resonator with its design parameters.

2. The size of the entire device has to be minimum. In the case of study on mass loading study of resonant structures on SAW resonators, at least one resonance mode of the structure should be closer to the SAW resonator frequency. More the number of devices in a wafer will increase the probability of tracing out the effect of resonant structures. Therefore at least 50 SAW devices are targeted on a complete wafer.

3. Bond pad size, bond pad separation, and bond pad are to be designed compatible with the RF-probe station. In some cases, large size bond pads are kept such that wires can be bonded over them using silver paste.

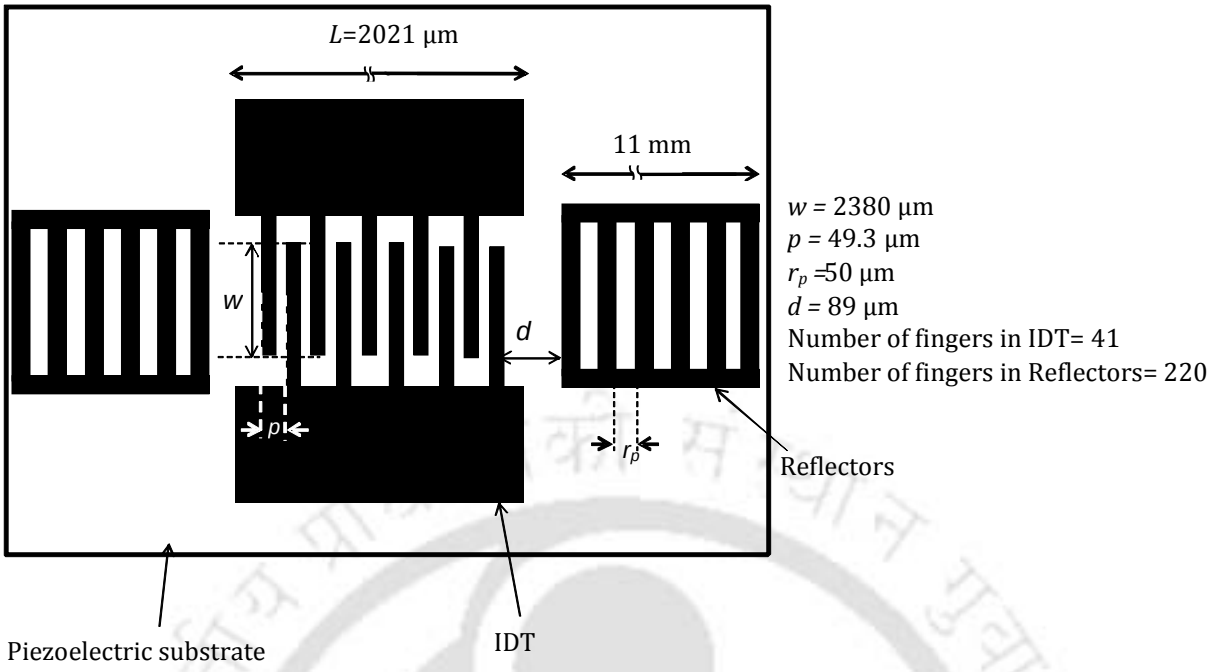

Figure 4.1. Typical dimensions of SAW resonator designed for studying the mass loading effect of resonant structures attached to their surface.

4. Devices are to be placed on wafer to use maximum area of the wafer.

5. Dimensions of delay line are decided such that it offers minimum attenuation to SAW and sufficient space should be left to apply absorbers at the edge of the device.

4.1.2 Fabrication of SAW resonator

The procedure for fabricating SAW devices mentioned in [69] is closely followed in this work. IDTs made of aluminium electrodes are fabricated over the lithium niobate piezoelectric substrate. The following fabrication steps are carried out 4 inch lithium niobate substrate,

(a) Layout design and mask writing

Direct laser writing over photoresist coated wafer can make IDT patterns with high accuracy. As the devices are to be fabricated in a whole 4 inch wafer, direct laser writing will consume lot of time. Hence it's decided to make UV lithography mask using laser writer. The design for the mask is designed using CleWin software. The layout for the mask is designed in such a way that maximum number devices can be occupied in a 4 inch wafer. Ten alignment markers are included in the layout to facilitate second layer lithography for mass loading study of resonant structures. Bond

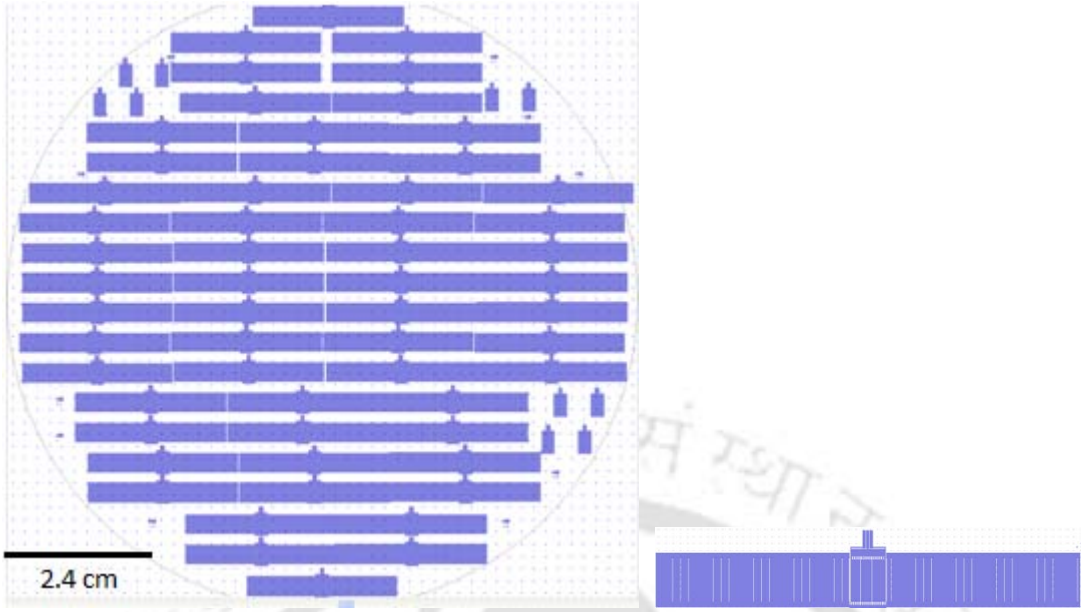

(a) (b)

Figure 4.2.(a) Snap shot of layout for SAW resonators to be fabricated over complete 4 inch wafer designed using CleWin software, (b) Magnified view of IDT and reflectors.

pads are designed to compatible with a 200 μm pitch RF- probe. A snap shot of layout of a device and alignment marker drawn using CleWin software is shown in Figure 4.2.

Chrome plate masks for fabricating the SAW resonator patterns are written using laser writer (Microtech LW – 405). As the minimum dimensions of the pattern to be written is of 24.65 μm, lens 3 of the laser writer is employed for making the mask patterns over the chrome plates. The laser writing process took 14 hours, the chrome plates are developed using MF 26A developer (MicroChem, USA). The exposed chromium is etched using chromium etchant solution. The remaining positive photoresist is removed using acetone, followed by pirrana solution. Figure 4.3 shows an optical image of a portion of mask, it can be seen that mask has turned out properly and dimensions are appropriate. Further fabrications steps are summarized in figure 4.4 (a) – (e).

(b) Cleaning of wafer

A 4 inch lithium niobate wafer is placed inside a beaker containing acetone bath and wafer is cleaned by placing the beaker inside ultrasonic bath for 5 minutes. Further, the wafers are placed in methanol for 5 minutes to remove the residual acetone. Finally, wafers are placed in de-ionized (DI) water and dried using filtered nitrogen gas.

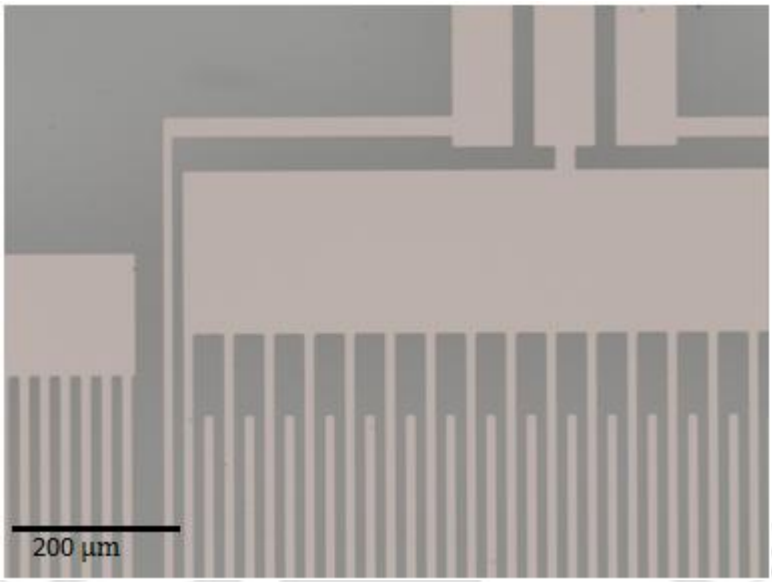

Figure 4.3. Optical microscope picture of the IDT pattern over the chrome mask plates.

(c) Metallization

After cleaning, using thermal evaporator coating system an aluminium metal of thickness of 100 nm to 200 nm is coated over the wafer. The aluminium pellets are cleaned using acetone and trichloro ethylene (TCE). The pellets are etched with aluminium etchant for 5 minutes to remove the native oxides. Further, the pellets are dropped in DI water. Finally the pellets are dried and dehydrated by heating them to a temperature of 120°C. This pellet cleaning method improved the adhesion of aluminium on the wafer surface.

(d) Photoresist coating

The wafer is then placed inside the spin coater. It is ensured that the wafer centre is exactly aligned with the spinner. AZ2514E photoresist (Microchemicals, GmBH) is dispensed from the bottle and spread all over the wafer. The wafer is spun for a speed of 500 rpm for 5 s and followed by 2500 rpm for 35 s. An acceleration of 300 rpm/s is maintained throughout the spinning processes. By this method a photoresist coating of 1.5 µm thickness is achieved over the wafer.

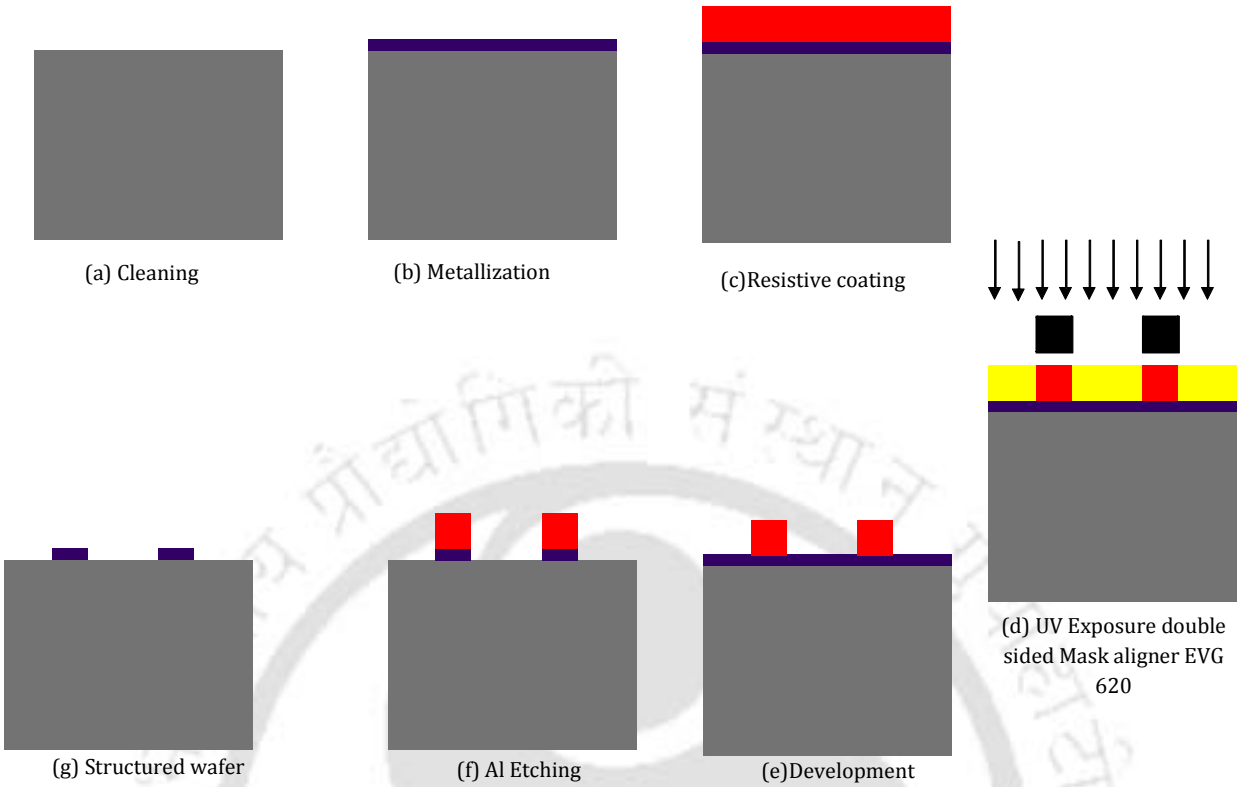

Figure 4.4. Fabrication process flow employed in fabricating SAW devices.

(e) Soft baking

The wafer with the photoresist coating is then soft baked by placing it in a hot plate at a temperature of 110°C for 50 s. To avoid wafer getting stuck to the hotplate surface, wipes are placed between wafer and hot plate.

(f) Exposure and development

The wafer is placed in UV mask aligner (EVG 620) substrate chuck. The mask aligner is mechanically set to handle a 5 inch mask plate and a 4 inch wafer. The exposure parameters such as wafer thickness, separation between the wafer and mask, exposure UV dosage of 75 mJ are set using the software program. The patterns in the mask are transferred to the wafer by UV exposure. The wafer is then rinsed in MF 26 A developer (Shilpey Europe, U.K.) solution for 40 s. The wafer is taken out from the developer solution once the patterns are identified in the wafer. If the wafer is placed for excess time it will lead to over development and finally ends with poor features on the wafer. The exposure and development are optimized after three trials.

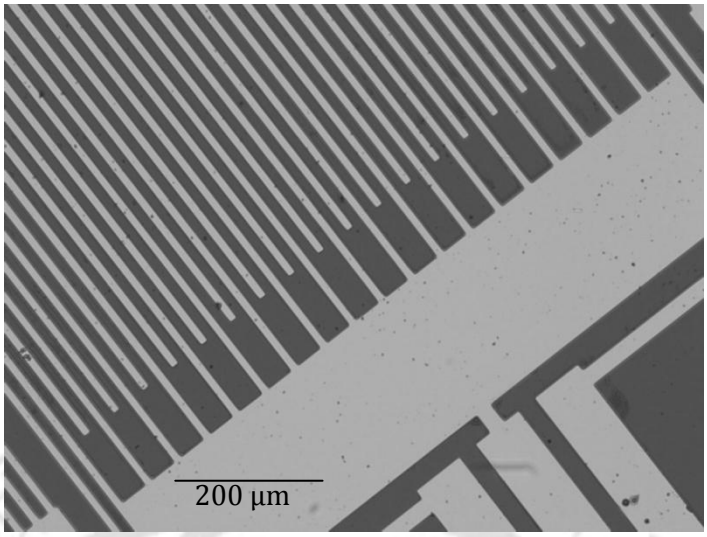

Figure 4.5. A optical microscopic image of a portion of fabricated electrode patterns of an IDT.

(g) Post baking

The developed patterns are cross checked with optical microscope. The wafer is then hard baked by placing them in hot plate at a temperature of 120°C for 2.5 minutes.

(h) Aluminium etching

Aluminium etchant is prepared by mixing 19 ml of orthophosphoric acid with 1 ml of nitric acid and 4 ml of DI water. The etchant is prepared in bulk and stored in a bottle. The post baked wafer is then placed in etchant solution for 1 to 2 minutes. Once the aluminium is etched out the wafer is immediately taken out from the etchant solution and placed in DI water. Excessive time in etching will lead to undercut in the IDT or reflector electrodes. Therefore the wafer is continuously monitored under microscope for every 30 s during the etching process. The wafers are then dried using nitrogen gas.

(i) Removal of photoresist

The wafer is placed in acetone bath for 2 minutes, followed by methanol and DI water and subsequently dried with nitrogen gas. The fabricated SAW resonator patterns are shown in the Figure 4.5. The final process is decided after three trial runs of spinning and development parameters for a 4 inch wafer. The wafers are recovered after each trial using piranna solution (One part of H_2O_2 and 3 parts of H_2SO_4). Figure 4.6 shows optical image of a fabricated SAW delay line device with bond pads suitable to perform humidity sensor experiments explained in section 3.2.

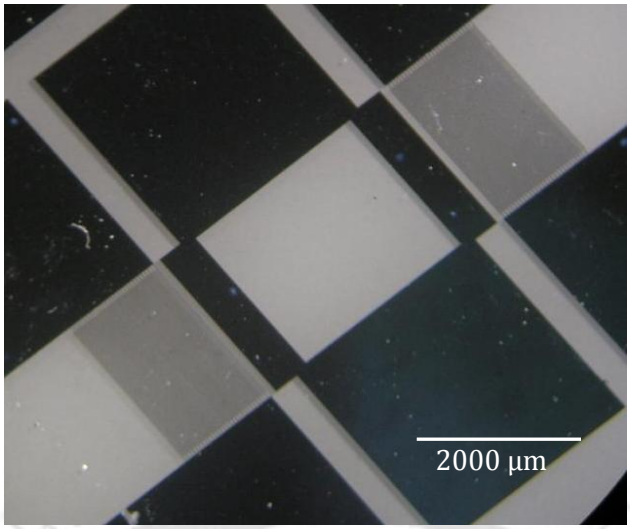

Figure 4.6. Optical imagae showing a complete SAW delay line device with bondpads suitable to bond external wires using silver paste.

4.2 Material selection for resonant structures

As the intention is to study the mass loading effect of resonant structures fabricated on SAW resonators, it was decided to fabricate high aspect ratio pillars on SAW resonators which is one kind of resonant structures. Initially palladium metal nano-pillars of high aspect ratio are considered for fabrication on a GHz resonator. After studying limitations of e-beam lithography and the number of pillars to be made on resonators, it was concluded that it would be practically impossible at present technology to make several resonant structures on a complete wafer. With the present technology of micro fabrication, we have finalized the dimension of pillars to micro metre range such that usual UV photo lithography could be used to fabricate the pillars.

In a SAW sensor working on principle of mass loading, the volume or density or elastic properties of sensing medium changes in the presence of the measurand leading to a change in mass loading to the acoustic path of the SAW device. Thus to mimic mass loading change in a SAW sensor, it was decided to fabricate pillars of different dimensions by varying height or width in small intervals, and set of pillars having unique dimension on every SAW resonator. By this the thesis work is not restricted to any specific sensor; rather explain novel class of SAW resonant sensors. SU-8 which is a negative photo resist is found to be suitable material for resonant structures because of its properties mentioned below

SU-8 is a commonly used epoxy-based negative photoresist. It is a very viscous polymer that can be spun or spread over a uniform thickness ranging from 1 μm up to 2 mm and still be processed with standard contact lithography. It can be used to pattern high aspect ratio (>20) structures. Its maximum absorption is for ultraviolet light with a wavelength of 365 nm. When exposed, SU-8's long molecular chains cross-link causes solidification of the material. The mechanical properties such as the young's modulus (E = 4.02 GPa) and density (ρ = 1190 kg/m^3) of SU8 are promising to perform high aspect ratio structure experiment over the fabricated SAW resonators. Various other mechanical properties of SU-8 are given in the appendix E.

The following reasons made to choose SU-8 as suitable candidate for mass loading study on resonant structures.

1. High aspect ratio (HAR) structures made of SU-8 photoresist are used as moulds in fabricating various metals and polymer HAR structures [70].

2. Methodologies to fabricate HAR structures made of SU-8 are reported elsewhere. SU-8 microstructures with aspect ratio larger than 50 were fabricated using soft bake methodology [71]. A number of densely packed SU-8 HAR structures were fabricated and a methodology to prevent pattern collapse is reported [72].

3. SU-8 structures are also used in piezoelectric devices. SU-8 micro channels are used in surface acoustic wave (SAW) micro fluidic device [73]. SU-8 HAR moulds are used in fabricating components in a piezoelectric motor [74].

Generally the fabrication process of the photo resist is provided in the data sheet of the manufacturer. However these processes vary for various substrates. Experiments, results and optimized recipe to develop SU-8 structures over SAW resonators are elaborated in the following section.

Generally the fabrication process of the photo resist is provided in the data sheet of the manufacturer. However these processes vary for various substrates. The optimized recipe to develop SU-8 structures over SAW resonators are described in the following section.

4.3 Development of high aspect ratio (HAR) structures

The process to develop high aspect ratio (HAR) structures of SU-8 over a SAW resonator is challenging. The major questions that arise in making high aspect ratio structure over SAW devices are as follows

1. Will the SU8 adhere to lithium niobate substrate? Will the SU8 adhere to metal surface?
2. Which SU8 to choose?
3. What is the recipe?

4.3.1 HAR structures with SU-8 process: Initial setup

The basic process steps used in the fabrication of HAR structures with SU-8 are shown in the flow diagram in figure 4.7. Several trials are carried out to optimize the recipe to fabricate HAR SU-8 pillars on Lithium niobate and aluminium substrates. Lithium niobate wafers of size 2 cm × 2 cm are cleaned with acetone in an ultrasonic bath for 5 minutes. The residual acetone was removed using methanol.. Finally wafers are rinsed in DI water and dried using nitrogen. In some samples aluminium of thickness of 100 nm is coated using thermal evaporation. After cleaning process, the samples are dehydrated at 120 °C for 15 minutes. SU-8 is directly poured on to the wafer sample and thin film of SU-8 is coated over the samples. The samples are pre-baked by placing them over the hot plate. Optical mask containing features of size 5 μm × 5 μm is used during UV exposure to realize high aspect ratio SU-8 pillar structures. UV mask aligner (EVG 620) is used for UV exposure, followed by post baking processes. The samples are then developed by placing them in SU-8 developer (Microchem, USA) solution for 20 to 30 minutes. The spin parameters, baking temperatures and UV dosage are varied in every trial of SU-8 fabrication. Optical microscope is used to characterize the fabricated SU-8 microstructures and images are directly recorded to a computer. The dimensions of the fabricated pillars are measured by forcing them to topple on the substrate. The recipe and corresponding images of SU-8 structures obtained in each trials are discussed in the following section.

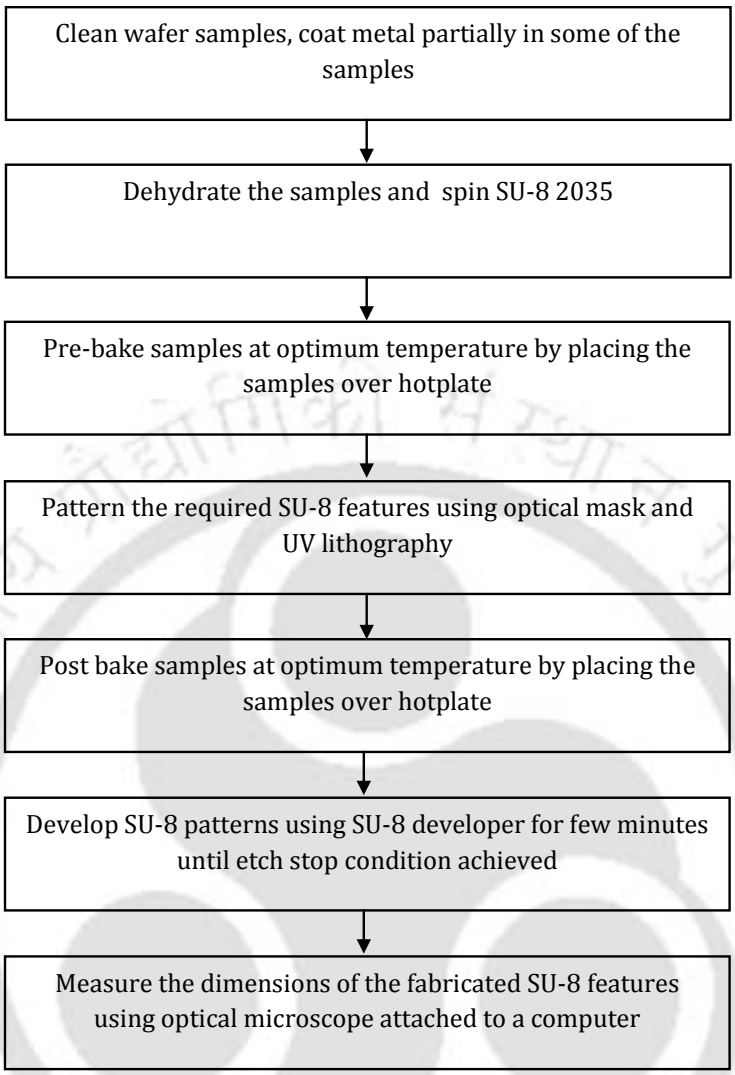

Figure 4.7. Flow chart showing the general SU-8 processes flow used in the trials.

4.3.2 HAR structures with SU-8 process: Trial 1

SU-8 2035 (Microchem, USA) is poured directly over the samples and spun using a spin coater. According to the data sheet of SU-8 2035 [75], the spin parameters to produce SU-8 film thickness of 35 µm are as follows. An initial speed of 500 rpm for 5 s and a final speed of 4000 rpm for 30 s with a ramp of 300 rpm/s. After spin coating SU-8, the samples are exposed to UV of constant dose of 100 mJ/s for 30 s. Optical mask containing features of size 5 µm × 5 µm is used during UV exposure to realize SU-8 pillar structures. The fabricated SU-8 structures at the end of trial 1 is shown in figure 4.8, it can be observed that the adhesion of SU-8 pillars over the substrate was poor

and the applied UV exposure dose of 100 mJ/s seems to be insufficient for patterning the structures.

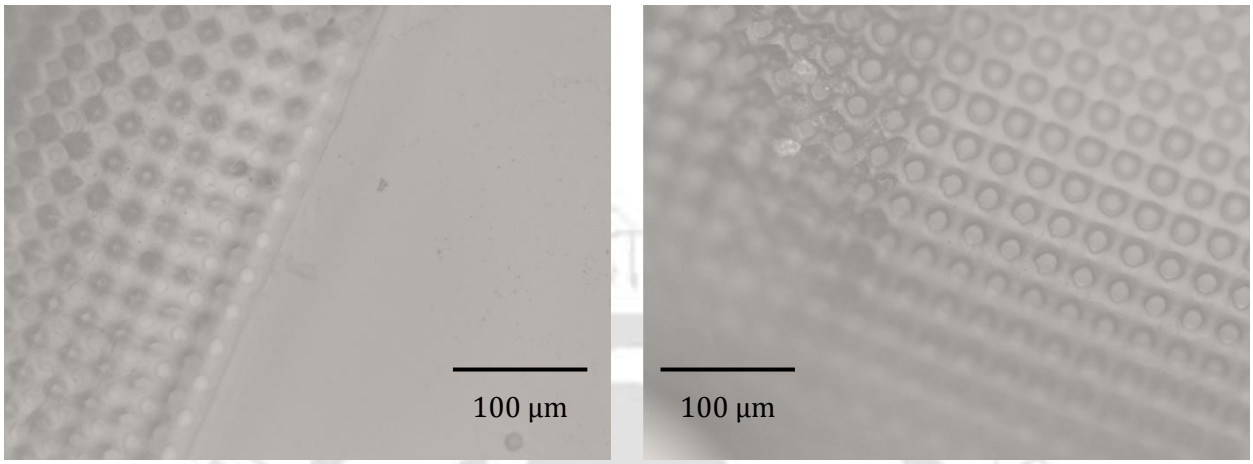

(a) (b)

Figure 4.8 (a) and (b). SU-8 layers on lithium niobate substrate at the end of trial 1.

4.3.3 HAR structures with SU-8 process: Trial 2

In second trial the surface of the substrate is made hydro-phobic by coating hexamethyldisilazane (HDMS) on to it. HDMS is spun over the sample at 3000 rpm for 30 s. Further SU-8 2035 is coated over the sample with trial 1 spin parameters. Samples are exposed for 30 s to UV with constant dose of 150 mJ/s. Figure 4.9 shows the result of trial 2 and it can be seen that pillars peel out from the substrate.

4.3.4 HAR structures with SU-8 process: Trial 3

Another experiment for inspecting the adhesion of pillar structure is conducted in trial 3. Nine samples are processed each having different spin parameters and UV exposure dosage. Two samples are coated with aluminium to examine the adhesion of pillars over the metal surface. The samples are baked at 120°C for 15 minutes to remove moisture content. Further HDMS is spun over the samples at 3000 rpm for 30 s. SU-8 is coated using spinner with the following spin parameters

Table 4.1 Spin parameters for trial 3

Initial speed	500 rpm for 5 s
Ramp (rpm /s)	300
Different final speed (rpm) considered	3500, 3800, 4000, 4200, 4500, 5000
Different dose (mJ/s) considered	120, 150, 180, 200, 230

The SU-8 pillar patterns realized during trial 3 are shown in figure 4.10(a)-(f). The particular spin speed and dosage employed are indicated under each image. It was observed that the adhesion of high aspect ratio SU-8 pillars with the lithium niobate substrate was not adequate. However it was observed that pillar stick moderately to aluminium surface. Pillars of height ranging from 56 μm to 106 μm are obtained. The height of the pillars is determined by measuring the length of the broken or fallen pillars on the substrate.

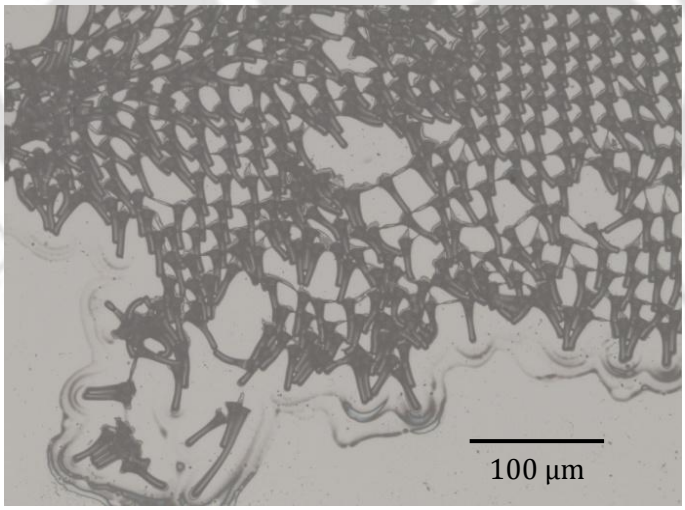

Figure 4.9. Peeled of SU-8 features from substrate at the end of trial 2.

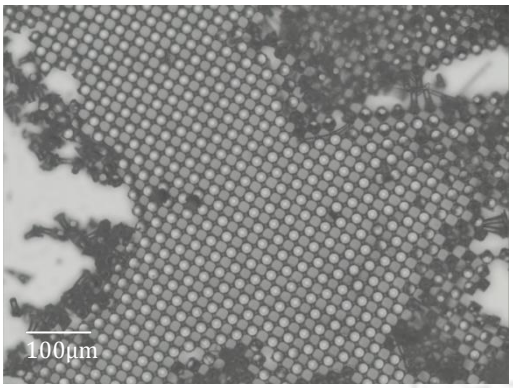

(a) Spin speed: 3500 rpm, and UV dose: 150 mJ/s

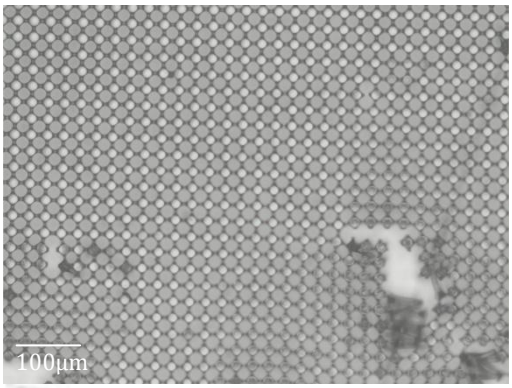

(b) Spin speed: 3800 rpm, and UV dose: 150 mJ/s

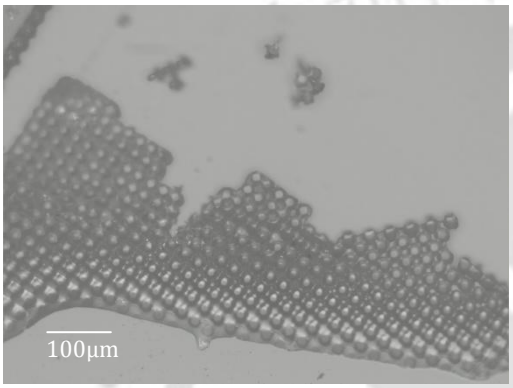

(c) Spin speed: 4000 rpm, and UV dose: 150 mJ/s

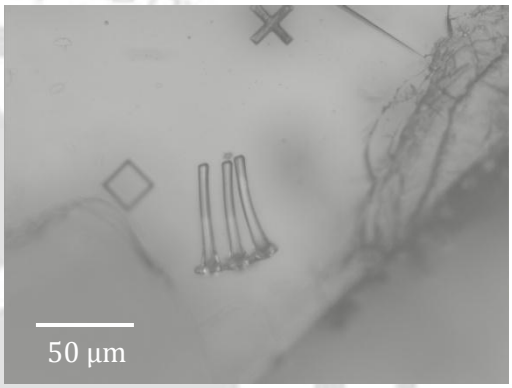

(d) Spin speed: 4200 rpm, and UV dose: 150 mJ/s

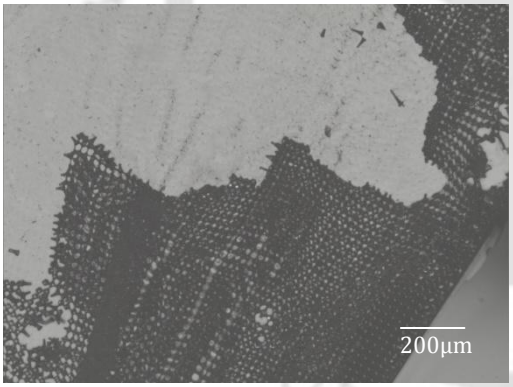

(e) Spin speed: 4500 rpm, and UV dose: 150 mJ/s

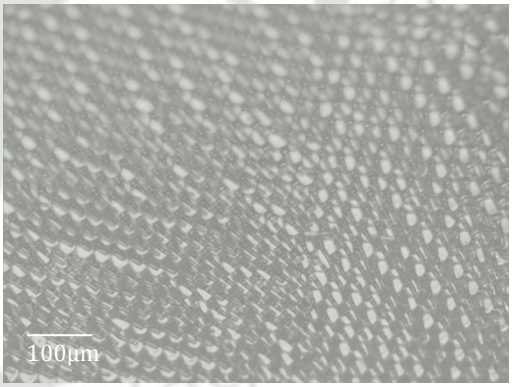

(f) Spin speed: 5000 rpm, and UV dose: 150 mJ/s

Figure 4. 10 (a)-(f). SU-8 pillar structures over lithium niobate samples developed during the trial 3. The spin speed and UV dosage are mentioned under the figure.

4.3.5 HAR structures with SU-8 process: Trial 4

In this trial, an attempt is made to bond the SU-8 structures using OmniCoat (Microchem, USA) [76]. The steps involved in fabrication of pillars of SU-8 in this trial are illustrated in figure 4.11 (a) – (h).

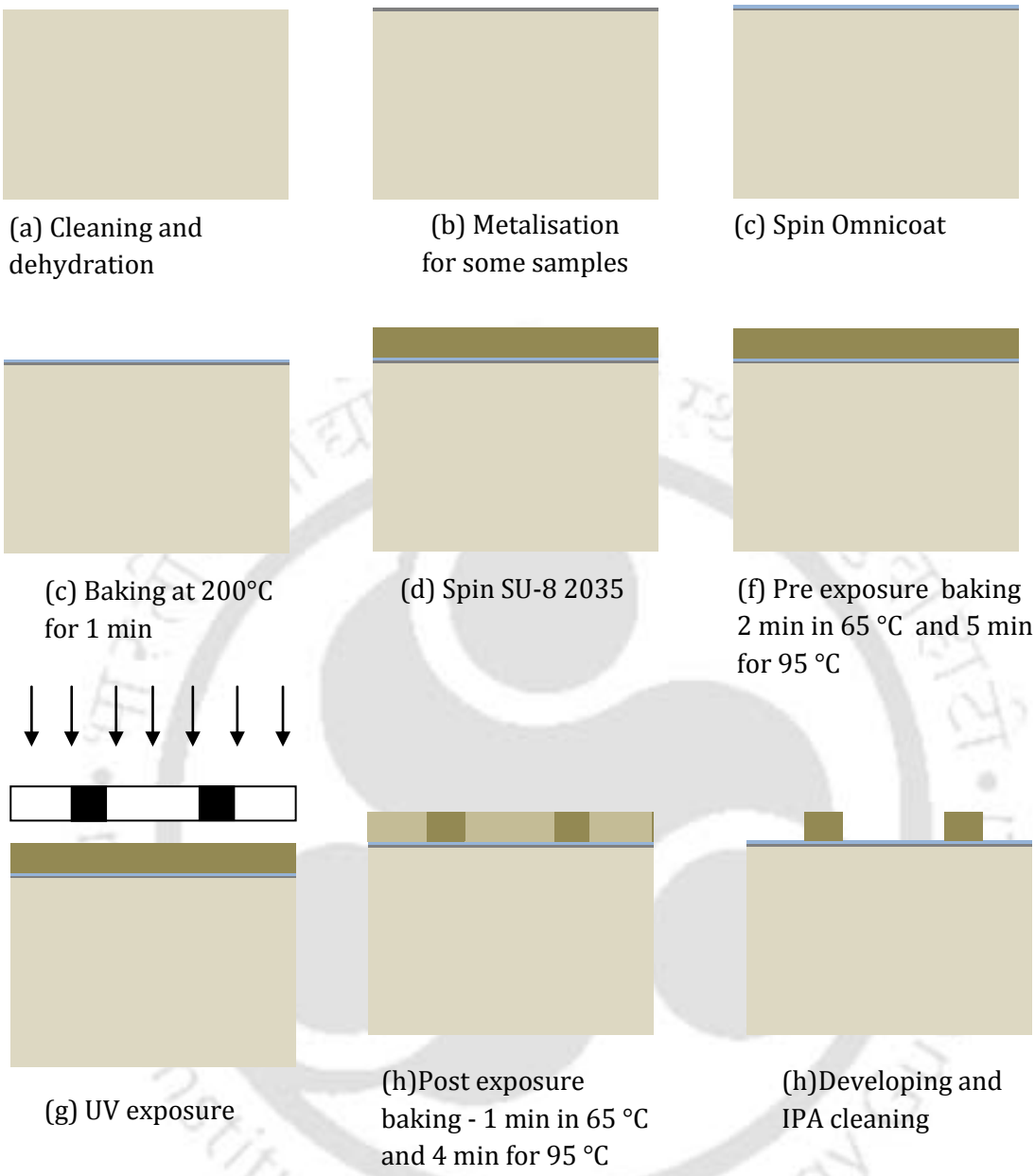

Figure 4.11. SU-8 fabrication steps employed during trail 4 of the experiment.

After cleaning and dehydration processes, a thin film of OmniCoat (Microchem, USA) is coated over the samples. OmniCoat solution is gently dispensed on the sample and spunned using spin coaterwith a final speed of 4000 rpm for 30 s and an OmniCoat film thickness of 17 nm is obtained. The samples are then baked at 200 °C in hotplate for 1 minute. SU-8 2035 is spun on 7 samples. An initial spin speed of 500 rpm for 5 s and ramp of 300 rpm/s is set as spin parameters for the spin coater. The final speed is varied from 2000 rpm to 7000 rpm for 45 s for different samples. The sa-

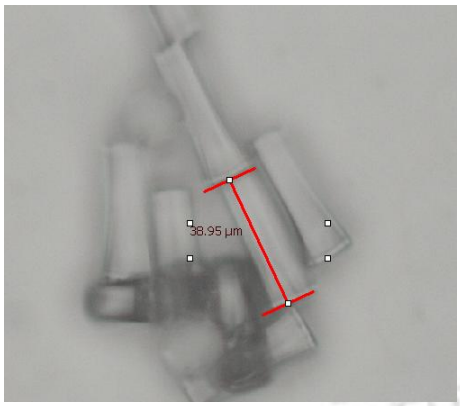

(a) Spin speed: 6000 rpm and UV dosage: 350 mJ/s

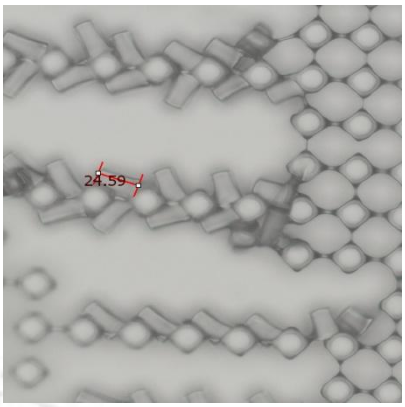

(b) Spin speed:5000 rpm, and UV dosage: 400 mJ/s

(c) Spin speed: 4000 rpm and UV dosage: 300 mJ/s

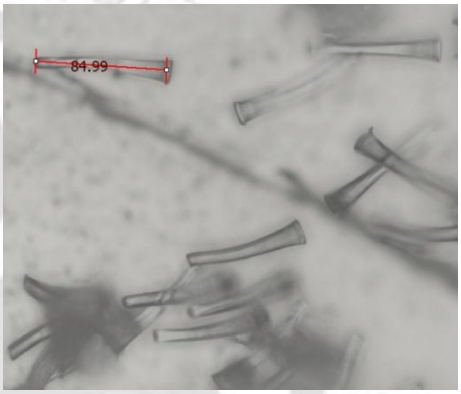

(d) Spin speed: 3000 rpm, and UV dosage: 200 mJ/s

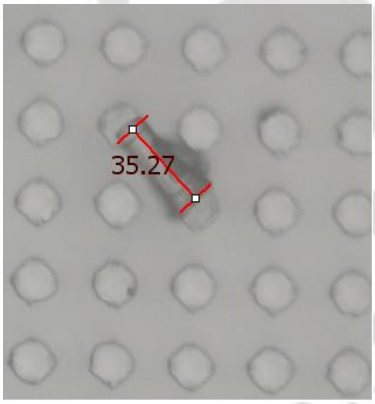

(e) Spin speed: 6500 rpm and UV dosage: 350 mJ/s

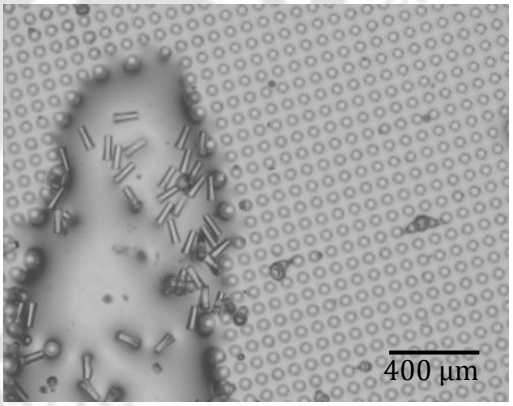

(f) Spin speed: 5000 rpm and UV dosage: 400 mJ/s

Figure 4. 12 (a)-(f). Fabricated SU-8 pillars at the end of trial 4. The spin speed and the UV dosage used for the particular sample are mentioned under the figure. In particular 4.12 (f) shows an optical microscope image a strongly adhered SU-8 micropillars on the substrate, manualy peeled off pillars from the substrate using tweezer to measure the height of the pillar. A spin speed of 5000 rpm and UV dosage of 400 mJ/s is finalised make the pillars.

-mples are then pre-baked at 65 °C for 2 minutes and at 95 °C for 5 minutes. The samples are exposed to UV for 30 s using EVG mask aligner (EVG 620), with constant UV dose varying from 200 to 450 mJ/s. Optical mask containing features of size 5 µm × 5 µm is used during UV exposure to realize SU-8 pillar structures. The samples are then post baked at 65 °C for 1 minute and 95 °C for 3 minutes. The structures are developed by placing the samples in SU-8 developer bath for 10 minutes. The duration of developing varies from sample to sample depending on the size and features of SU-8 structures. In general, the samples are kept in developer solution until the sample stop precipitating white fluid and subsequently rinsed in Iso propyl alcohol (IPA) solution.

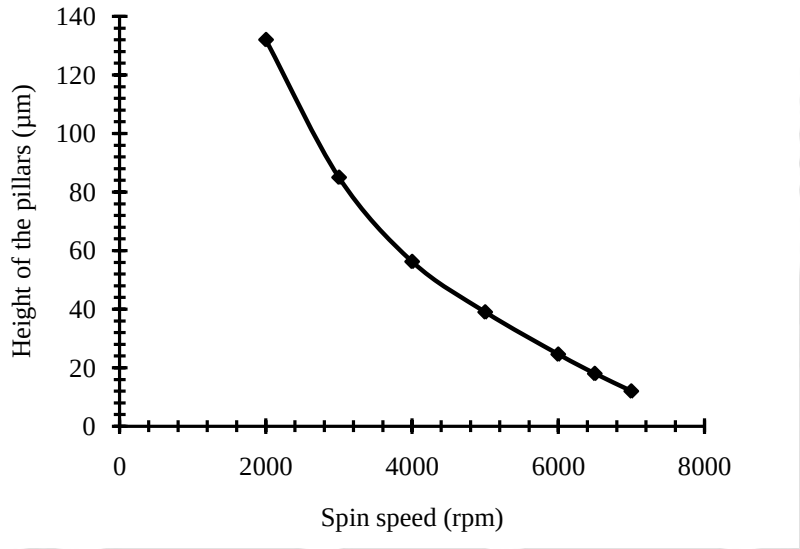

Figure 4. 13. Plot of spin speed versus height of the SU-8 pillars

Figure 4.12 (a) – (f) shows the SU-8 patterns formed during trial 4. It can be observed that there is a great variation in pillar heights for different spin speed. The optimum spin speed required to create a resonant structure on a a 2 cm × 2 cm sample is ranging from 5100 to 5200 rpm, with a constant UV exposure dose of 375 mJ/s**.** Figure 4.12 (f) shows the optical microscope image of a top view of a sample substrate with SU-8 high aspect ratio pillars attached to it. It can be seen from the right hand side section of the image that the pillars are well adhered with the substrate. The surface of the substrate is gently scratched with a metal tweezers such that the vertical pillars will fall off on the substrate and hence is height can be calculated by measuring the length of the pillar. The height of the pillar is measured using optical microscope and camera. Thin film coating of OmniCoat has highly improved the adhesion of these high aspect ratio SU-8 pillars. Spin parameters and UV exposure dosage are given by the manufacturer in SU-8 datasheet; however these parameters are

modified for the piezoelectric substrate such as the lithium niobate. Figure 4.13 shows the plot of the spin speed versus height of the micro-pillars obtained during the trial 3 and it may be noted that the spin parameters slightly deviate from SU-8 2035 data sheet [75]. The following settings are found to be optimum. UV exposure dosage of 350 mJ/s to 400 mJ/s for a film thickness of 35 µm to 40 µm; spin speed of 5000 rpm for 45 s; UV exposure constant dose of 400 mJ/s for 30 s.

4.4 Fabrication of resonant structures SAW resonator

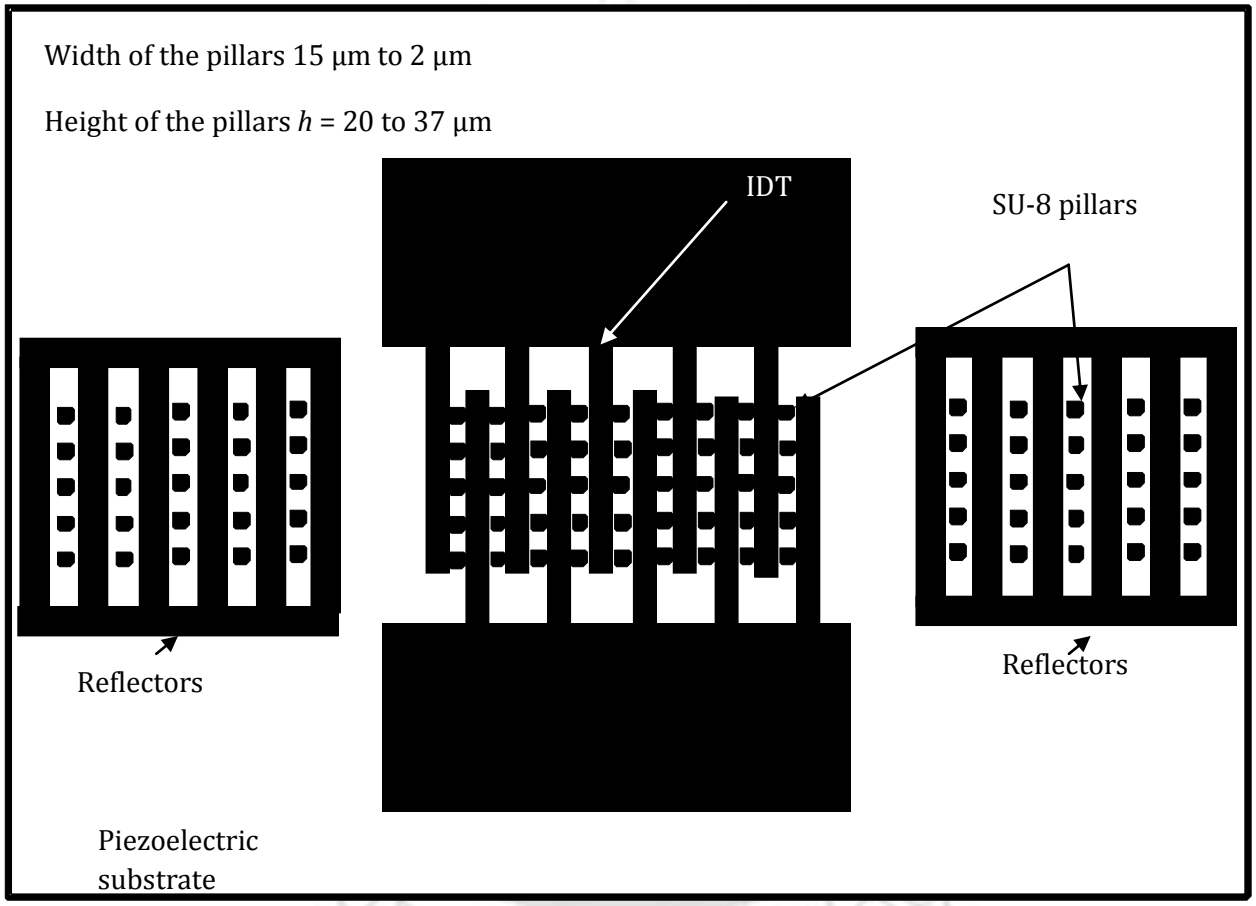

Figure 4. 14. Typical dimensions and arrangement of SU-8 pillars fabrication over SAW resonator

As the aim of this thesis is to study the mass loading effect of SU-8 pillars of different resonance frequency on SAW resonator and it was decided to fabricate pillars with different cross-section (width). Fabricating pillars with different height is desirable for studying their mass loading effect as discussed in the simulation of mass loading effect of high aspect ratio pillars in chapter 3, however micro fabrication of pillars with different width and same height is simple than fabricating pillars with same width and different heights. Initially the processes to fabricate SU-8 pillar over

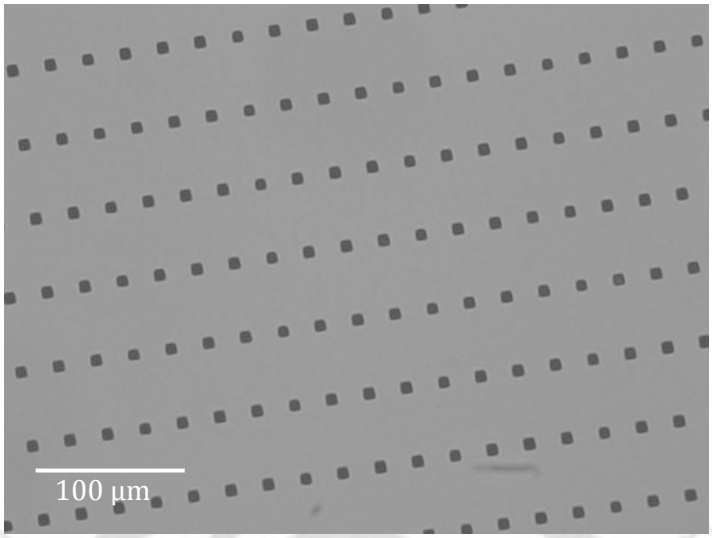

Figure 4.15. Optical microscopic image showing a portion of second layer mask.

lithium niobate and metal substrate is optimized as described early. In order to fabricate resonant structures constituting SU-8 micro pillars, a second layer mask layout is prepared using Clewin software. The mask consists of square boxes of varying size. The square box are drawn in the second layer layout such that they can form one SU-8 pillar per period along the propagation path of the SAW and one per wavelength along the aperture of the resonator device. The schematic in figure 4.14 shows position of SU-8 square pillars in the SAW resonator. The theoretical aspects of fabricated resonant structure will be discussed in the next chapter, while the fabrication procedure of these pillars on SAW resonator will be discussed in the following section of this chapter.

4.4.1 Fabrication of SU-8 pillars over SAW resonator

A 5 inch mask is written using the laser writer. Lens 4 of the laser writer is used to draw the patterns over the mask plate. Figure 4.15 shows a portion the layer 2 mask.. The steps involved in the second layer are shown in figure 4.16 (a) - (c). The optimized fabrication processes discussed in trial 4 are used for fabricating SU-8 pillars on the fabricated SAW resonator. Initially Omnicoat poured on the wafer containing SAW resonators patterns. After post baking the wafer up to 200° C for 1 minute in hotplate, SU-8 2035 is poured on the wafer and thin film of SU-8 is coated using spin coater with the spin speed of 5200 rpm. A constant UV dosage of 375 mJ/s for 30 s is used to make patterns on SU-8 square prism pillars**.** Care is taken to match the alignment markers present in the mask and the layer 1 mask patterns fabricated on the wafer. Fine adjustments are carried out in the EVG 620 mask aligner system to confirm the pillars are fabricated exactly in the required place in

the wafers. Finally the baking and development process mentioned in the trial 4 are performed to finish the fabrication of SU-8 pillars (resonant structures) over the SAW resonators. The microscopic images of SAW resonators with SU-8 pillars structures are shown in Figure 4.17 (a) – (d). Figure 4.17 (a), (c) and (d) shows the closely packed pillars on the IDT and reflector electrodes. It can be seen that the pillars are arranged in a regular fashion. However in some cases as shown in figure 4.17 (b) the pillars have fallen on the substrate or slightly bent from their positions during fabrication. Figure 4.18(a) and (b) shows the scanning electron microscope (SEM) image of the pillars attached to SAW resonator. It is observed the pillars have height of approximately 20 µm.

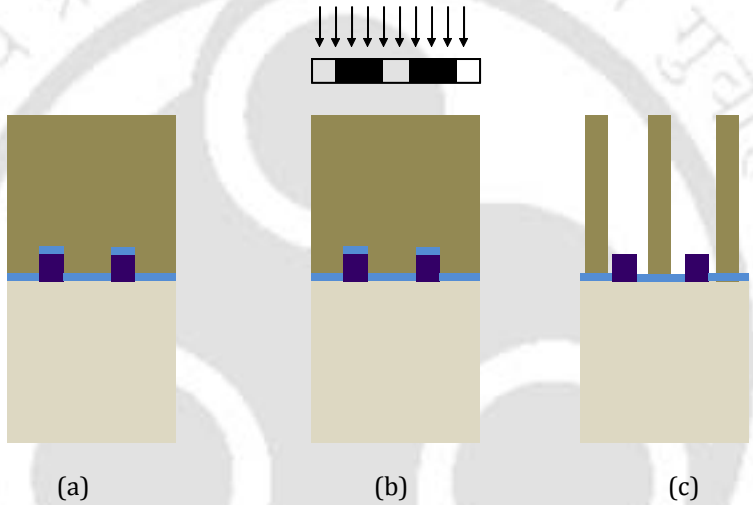

Figure 4.16. Fabrication steps (a) to (c) involved in fabricating SU-8 pillars on SAW resonator. (a) Coating of Omnicoat followed by SU-8 2035, (b) Pre-baking and UV exposure, and (c) post-baking and development.

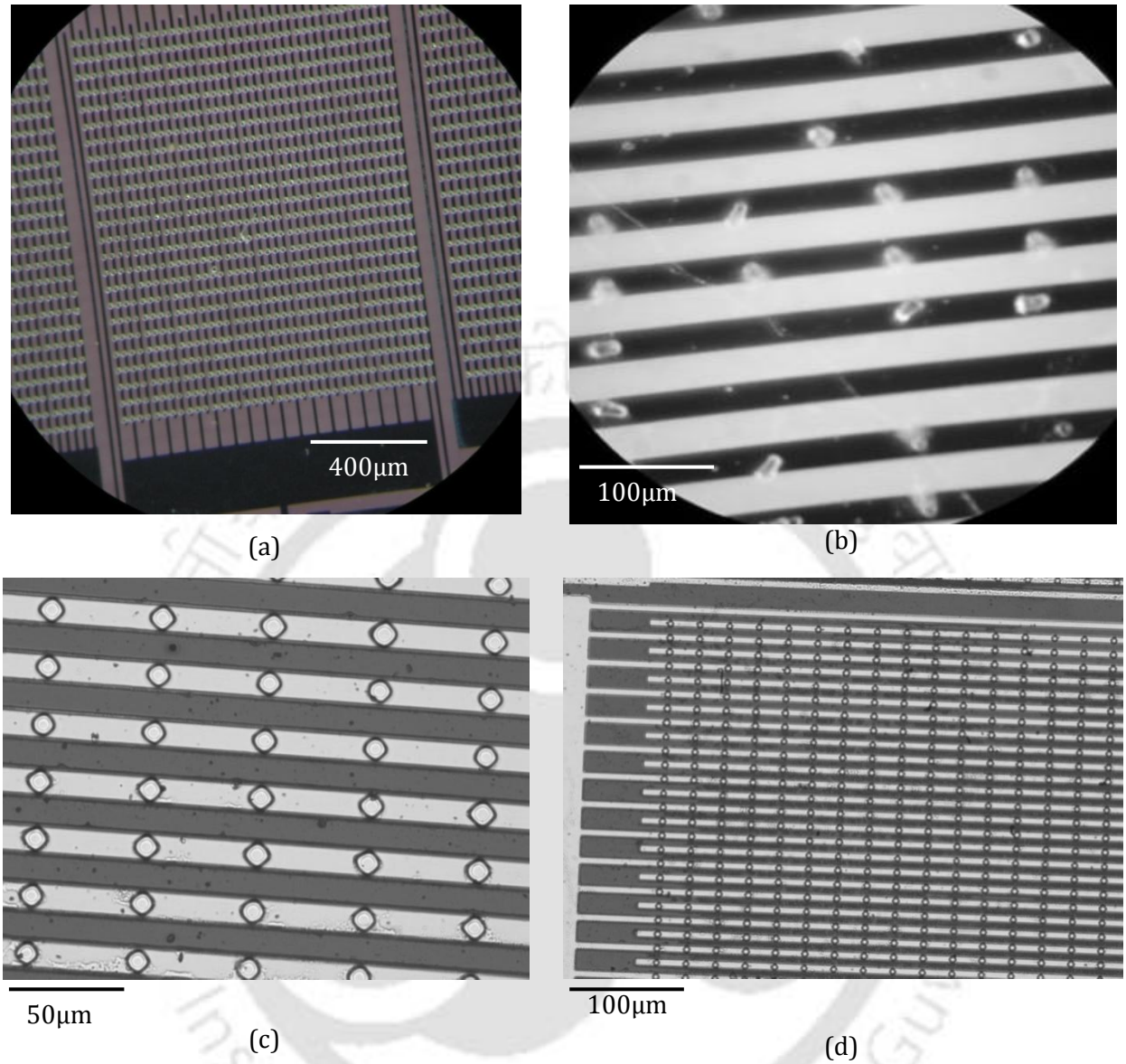

Figure 4.17. Optical microscope images showing the top view of fabricated SU-8 pillars on the surface of the SAW resonator. (a) Image showing closely packed pillars on the IDT and reflector electrodes, (b) Sample image showing fallen and bent pillars on substrate, (c) and (d) Image showing zoom in view of a pillars attached to resonator electrodes.

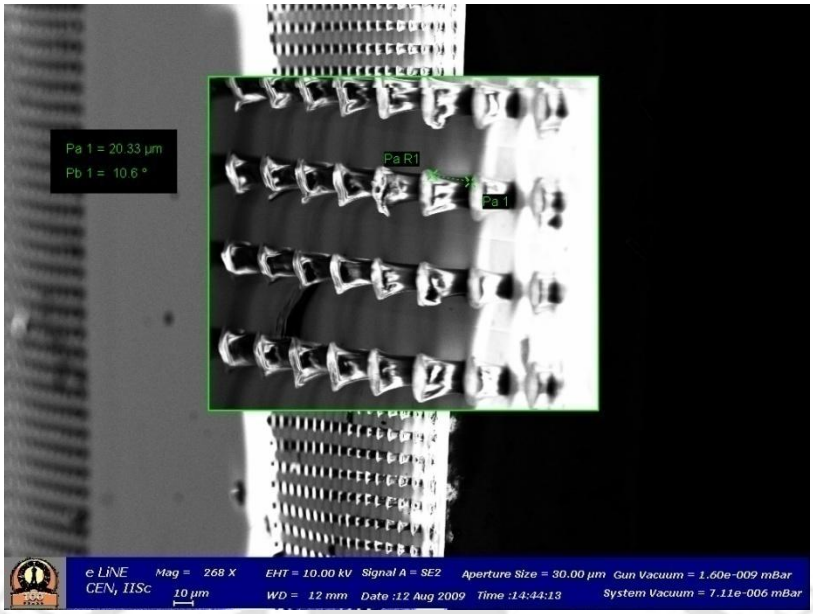

(a)

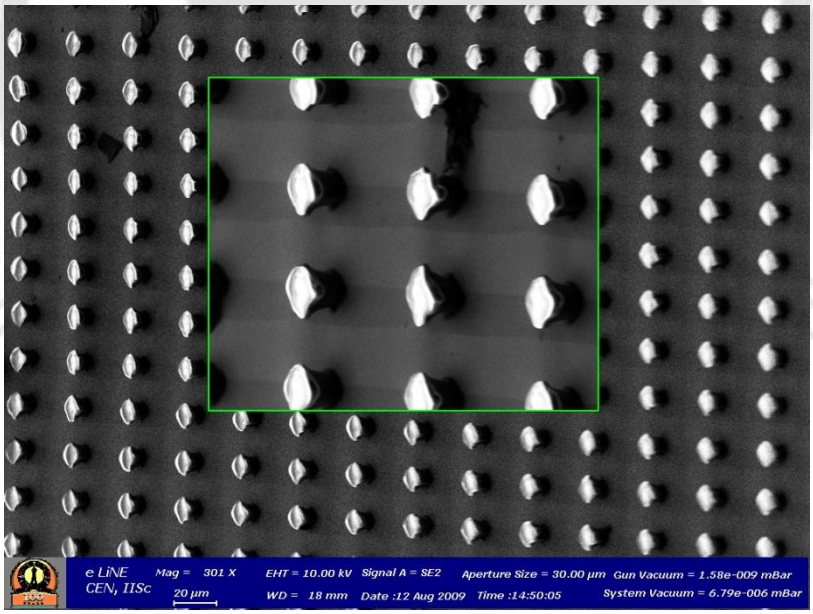

(b)

Figure 4.18 (a) and (b). SEM image of SU-8 pillars attached to the IDT fingers.

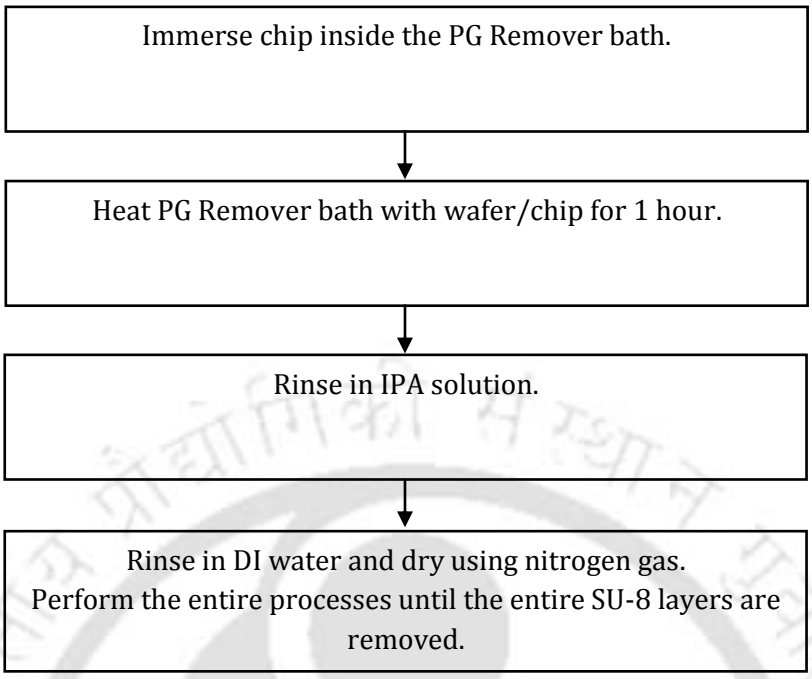

Figure 4.19. Processes flow for removing unwanted SU-8 layer from piezoelectric wafer or the SAW chip.

4.4.2 Process flow to remove SU-8 layers from piezoelectric substrate

In case of removal of SU-8 layers from substrate or the SAW device for reusability of the wafers, the SU-8 should be removed using separate process. Piranha solution does not help in clearing the layers and it results in black scum over the surface of the wafer and lead to permanent non-usability of the wafer. The PG Remover (Microchem, London) solution gave good results and the processes flow shown in figure 4.19 is used for removing unwanted SU-8 layers including the Omnicoat layers. Even though IDT structures did not get affected, we have repeated the entire fabrication process including the patterning the resonator structures while reusing the wafers.

4.4.3 Issues faced during SU-8 fabrication

Following are some of the challenges faced during the SU-8 fabrication

1. Using whole 4 inch wafer was difficult
2. Wafer cracks and breaks during baking process
3. Alignment of markers is cumbersome once the wafer breaks unexpectedly

4. The second layer mask did not turn out properly. The smaller dimensions were already disfigured in the mask itself. Use of lens 5 and better marker and layout design need to be carried out for future designs.

5. Spin parameters optimized for smaller wafer samples are not reproducible for the 4 inch wafer.

6. Development of SU-8 pillars takes longer time. Often smaller dimension pillars are destroyed during development process.

4.5 Summary

In this chapter we discussed the fabrication of SAW devices and SU-8 pillars. Important aspects of SAW device fabrication for the present study are briefly discussed. Large number of SAW resonators suitable for studying mass loading effect of SU-8 resonant structures are fabricated over an entire 4 inch lithium niobate wafer. Several SU-8 fabrication trials are conducted to optimize the recipe to fabricate SU-8 pillars over the previously fabricated SAW resonator. It was found that coating of OmniCoat thin film on the substrate prior to SU-8 film greatly helps in improving the adhesion of SU-8 pillars to the substrate. The processes and parameters are standardized and can be used for fabricating SU-8 structures over piezoelectric and metallic substrates.

A. Important Substrate Materials Used in SAW Sensor Applications

Important substrate materials used in SAW sensor application are shown in table A.1 [1], [3], and [80]

Table A.1. Important substrate materials used in SAW sensors

Substrate	**Propagation**	**K^2 (%)**	**Acoustic velocity (m/s)**
ST- quartz	X	1.89	3158
Y- quartz	X	1.1	3159
Y- $LiNbO_3$	Z	4.5	3488
Y -128° $LiNbO_3$	X	5.3	3992
77.5° Y- $LiTaO_3$	X	1.6	3379
36° Y- $LiTaO_3$	X	5	4160
Langasite	-	3.2	2742
100-011 GaAs	-	0.7	2864
Y-60° CdS	-	-	1702
ZnO	-	-	2639

B. Matrix Technique for Crystal Axes Rotation to given Euler Angles

It is important to rotate the crystal axes according to given Euler angles viz., ϕ, θ, and ψ rotated along x_1, x_2 and x_3 axis and align them with the required Cartesian co-ordinate axes. During such rotations, the stiffness matrix ($\mathbf{C}^E$), piezoelectric matrix (**e**) and dielectric matrix ($\boldsymbol{\varepsilon}$) of the material also gets transformed accordingly. A very efficient matrix technique has been developed for this purpose by W. L. Bond [29]. If the directional vector written as $\vec{r} = (x_1, x_2, x_3)$, then the directional vector written in terms of crystal axes: $\tilde{r}$ may be found using a coordinate transformation matrix **a,** and bond matrix $\mathbf{M_b}$. The rotated stiffness ($\tilde{\mathbf{C}}^E$), piezoelectric constant ($\tilde{\mathbf{e}}$), and permittivity matrix ($\tilde{\boldsymbol{\varepsilon}}$) can be obtained using the following equations

$$\tilde{r} = \mathbf{a}.\vec{r}$$

$$\tilde{\mathbf{C}}^{\mathbf{E}} = \mathbf{M}.\, C^E.\mathbf{M}'$$

$$\tilde{\mathbf{e}} = \mathbf{a}.\,\mathbf{e}.\,\mathbf{M}'$$

$$\tilde{\boldsymbol{\varepsilon}} = \mathbf{a}.\,\boldsymbol{\varepsilon}.\,\mathbf{a}$$

where the coordinate transform matrix **a** rotating around x_3, x_2 and x_1 (in the given order)as below

$$\mathbf{a} = \begin{pmatrix} a_{11} & a_{12} & a_{13} \\ a_{21} & a_{22} & a_{23} \\ a_{31} & a_{32} & a_{33} \end{pmatrix} = \begin{pmatrix} \cos(\phi)\cos(\theta) & \sin(\phi)\cos(\theta) & -\sin(\theta) \\ \cos(\phi)\cos(\theta)\sin(\psi) - \sin(\phi)\cos(\psi) & \cos(\phi)\cos(\psi) + \sin(\phi)\sin(\theta)\sin(\psi) & \cos(\theta)\sin(\psi) \\ \cos(\phi)\sin(\theta)\cos(\psi) + \sin(\phi)\sin(\psi) & \sin(\phi)\sin(\theta)\cos(\psi) + \cos(\phi)\sin(\psi) & \cos(\theta)\cos(\psi) \end{pmatrix}$$

The bond matrix $\mathbf{M_b}$ is as given below

$$\mathbf{M_b} = \begin{pmatrix} a_{11}^2 & a_{12}^2 & a_{13}^2 & 2a_{12}a_{13} & 2a_{13}a_{12} & 2a_{11}a_{12} \\ a_{21}^2 & a_{22}^2 & a_{23}^2 & 2a_{22}a_{23} & 2a_{23}a_{21} & 2a_{21}a_{22} \\ a_{31}^2 & a_{32}^2 & a_{33}^2 & 2a_{32}a_{33} & 2a_{33}a_{31} & 2a_{31}a_{32} \\ a_{23}a_{31} & a_{22}a_{31} & a_{23}a_{33} & a_{22}a_{11} + a_{23}a_{32} & a_{21}a_{33} + a_{23}a_{31} & a_{22}a_{31} + a_{21}a_{32} \\ a_{23}a_{31} & a_{22}a_{12} & a_{33}a_{13} & a_{12}a_{33} + a_{13}a_{32} & a_{13}a_{31} + a_{11}a_{33} & a_{11}a_{32} + a_{12}a_{21} \\ a_{11}a_{21} & a_{12}a_{22} & a_{13}a_{23} & a_{12}a_{23} + a_{13}a_{22} & a_{13}a_{21} + a_{11}a_{23} & a_{11}a_{22} + a_{12}a_{21} \end{pmatrix}$$

C. Material Constants of Lithium Niobate

Material constants of Lithium Niobate used in the thesis are taken from [43]. The constants for X cut Y - $LiNbO_3$ and Y cut Z- $LiNbO_3$ are given in section C.1 and C. 2, respectively.

C. 1Material constants of Y cut Z - $LiNbO_3$

Density (ρ) = 4675 kg/m^3

$$\text{Stiffness, } \mathbf{C}^E = \begin{pmatrix} 20.3 & 5.3 & 7.5 & 0.9 & 0 & 0 \\ 5.3 & 20.3 & 7.5 & -0.9 & 0 & 0 \\ 7.5 & 7.5 & 24.5 & 0 & 0 & 0 \\ 0.9 & -0.9 & 0 & 6.0 & 0 & 0 \\ 0 & 0 & 0 & 0 & 6.0 & 0.9 \\ 0 & 0 & 0 & 0 & 0.9 & 7.5 \end{pmatrix} \times 10^{10}\ \text{N/m}^2$$

$$\text{Piezoelectric constant , } \mathbf{e} = \begin{pmatrix} 0.0 & 0.0 & 0.0 & 0.0 & 3.7 & -2.5 \\ -2.5 & 2.5 & 0.0 & 3.7 & 0.0 & 0.0 \\ 0.2 & 0.2 & 1.3 & 0.0 & 0.0 & 0.0 \end{pmatrix} \text{C/m}^2$$

$$\text{Permittivity , } \boldsymbol{\varepsilon} = \begin{pmatrix} 44 & 0 & 0 \\ 0 & 44 & 0 \\ 0 & 0 & 29 \end{pmatrix}$$

C. 2 Material constants of Y cut Z - $LiNbO_3$

Density (ρ) = 4675 kg/m^3

$$\text{Stiffness, } \mathbf{C}^E = \begin{pmatrix} 24.24 & 7.52 & 7.52 & 0 & 0 & 0 \\ 7.52 & 20.3 & 5.73 & 0 & 8.5 & 0 \\ 7.52 & 5.73 & 20.3 & 0 & -8.5 & 0 \\ 0 & 0 & 0 & 7.52 & 0 & 8.5 \\ 0 & 8.5 & -8.5 & 0 & 5.95 & 0 \\ 0 & 0 & 0 & 8.5 & 0 & 5.95 \end{pmatrix} \times 10^{10}\ \text{N/m}^2$$

$$\text{Piezoelectric constant , } \mathbf{e} = \begin{pmatrix} 1.3 & 0.23 & 0.23 & 0 & 0 & 0 \\ 0 & 0 & 0.0 & -2.5 & 0 & 3.7 \\ 0 & -2.5 & 2.5 & 0 & 3.7 & 0 \end{pmatrix} \text{C/m}^2$$

$$\text{Permittivity , } \boldsymbol{\varepsilon} = \begin{pmatrix} 28.7 & 0 & 0 \\ 0 & 85.2 & 0 \\ 0 & 0 & 85.2 \end{pmatrix}$$

D. Absorbing Boundary Conditions

In order to avoid reflection of waves from the boundaries or edges of the SAW devices, absorbing boundary conditions are applied in the FEM simulations. The influence of wave reflections from boundaries can be reduced by assuming critical damping along the boundaries [38].This can be achieved by employing suitable values for Rayleigh damping coefficients in the COMSOL Multiphysics software [33].In Rayleigh damping model, the Rayleigh damping matrix **Z** is a linear combination of mass matrix and stiffness matrix as given below

$\xi = A_{dM} M + B_{dk} k$

where the mass proportional damping parameter (A_{dM}) and stiffness proportional damping parameter (B_{dk}) are damping coefficients and they are related to damping ratio (ξ) as

$$\xi = \frac{A_{dM} + B_{dk}\omega^2}{2\omega}$$

Absorbing boundary can be achieved by assuming critical damping, $\xi = 1$ and $A_{dm} = 0$ then $B_{dk} = 1/\pi.f$.

E. Mechanical Properties of SU-8

Table E.1.Mechanical properties of SU-8 [81]

Characteristics	Value	Conditions
Modulus of elasticity : *E*	4.02 GPa	In tension, postbaked at 95°C, screw tensile testing machine
	4.95 +/- 0.42 GPa	Hardbaked at 200°C, beam deflexion test
	4.4 GPa	Postbake at 95°C
Bi-axial modulus of elasticity	5.18 +/- 0.89 GPa	Postbaked at 95°C, thermal cycling test on Si wafer
Poisson ratio	0.22	Postbaked at 95°C, SM blend
Film stress	19 - 16 Mpa	For 0 - 400 mic. thick SU-8 film coated on a 3" 375 mic. thick Si wafer, prebaked, illuminated, postbaked at 95°C and brought back to room temperature (20°C)
Max stress	34 Mpa	Hardbaked at 200°C, lateral deflexion FEM analysis
Max sheer	0.009	Hardbaked at 200°C, lateral deflexion FEM analysis
Plastic domain limit	'no' plastic domain observed	Hardbaked at 200°C, sample pulled until

		fracture
Friction coefficient : μ	0.19	Postbaked at 95°C, pin-on-disc installation (10 g load)
Bond strength	4.8 +/- 1.2 MPa	On Au, Instrom pull test

Bibliography

[1] J. W. Gardner, V. K. Varadan, and O. O. Awadelkarim, *Microsensors MEMS and Smart Devices*. Chichester, U.K.: John Wiley & Sons, 2002.

[2] D. Morgan, *Surface Acoustic Wave Filters with Applications to Electronic Communications and Signal Processing*, London, U.K.: Elsevier, 2007.

[3] M. Thompson and D. C. Stone, in *Surface-Launched Acoustic Wave Sensors- Chemical Sensing and Thin-Film Characterization,* New York: Wiley & Sons, 1997.

[4] D. Amico, A. Palma, and E. Verona," Surface acoustic wave hydrogen sensor," *Sensor and Actuator*, vol. 3, pp. 31-39, 1982.

[5] T. M. Reeder, D. E. Cullen, and M. Gilden, "SAW oscillator pressure sensors," *Proc. IEEE Ultrasonics Symp.*, pp. 264 – 268, 1975.

[6] H. Wohltjen and R. E. Dessy, "Surface acoustic wave probe for chemical analysis," Analytical Chemistry, vol. 51, pp. 1458 – 1475, 1979.

[7] E. Gatti, A.Palma, and E. Verona, "A surface acoustic wave voltage sensor," *Sensors and Actuators*, vol. 4, pp. 45–54, 1983.

[8] A. J. Ricco, S. J. Martin, and T. E. Ziperian, "Surface acoustic wave gas sensor based on film conductivity changes", *Sensors and Actuator*, vol. 8, pp.319-333, 1985.

[9] A. D'Amico, A. Petri, P. Verardi, E. Verona, "Amonia surface acoustic wave gas detector," *Proc. IEEE Ultrasonics Symposium*, pp. 633- 636, 1987.

[10] S. W. Wenzel and R. M. white, "Flexural plate-wave gravimetric chemical sensor," *Sensors and actuators*, vol. 24, pp. 700-703, 1990.

[11] R. S. Falconer, I. F. Vetelino, D. J. Smith and M. J. Osbom , "An activation processes for increased sensitivity of a SAW gas microsensor," *proc. IEEE Ultrasonic Symposiu*m, pp. 315-318, 1990.

[12] J. Reichert, W. Coerdt, and H. J. Ache,"Development of a surface acoustic wave sensor array for the detection of methanol in fuel vapours," *Sensors and Actuators B,* vol. 13-14, pp. 293-296, 1993.

[13] K. B. Pfeifer, J.L. Sprung, and T.R. Galloway, "Polymer-coated surface acoustic wave monitoring of CCl_4 in a steam reforming reactor," *Sensor and Actuator B*, vol. 22, pp.37-45, 1994.

[14] J. Kondoh,Y. Matsuib, S. Shiokawab, and W. B. Wlodarski, "Enzyme-immobilized SH-SAW biosensor," *Sensors and Actuators B*, vol. 20, pp. 199-203, 1994.

[15] K. Beck, T. Kunzelmann, M. von Schickfus, and S. Hunklinger,"Contactless surface acoustic wave gas sensor," *Sensors and Actuators A*, vol. 76, pp. 103-106, 1999.

[16] F. Josse, F. Bender, and R. W. Cernosek, "Guided shear horizontal surface acoustic wave sensors for chemical and biochemical detection in liquids," *Analatical Chemistry*, vol. 73, pp. 5937-5944, 2001.

[17] D. D. Stubbs, S. H. Lee, and W. D. Hunt, "Molecular recognition for electronic noses using surface acoustic wave immunoassay sensors," *IEEE Sensors Journal*, vol. 2, pp. 294-300, 2002.

[18] M. Cole, G. Sehra, J. W. Gardner, and V. K. Wardan, "Development of smart tongue devices for measurement of liquid properties," *IEEE Sensors Journal*, vol. 4, pp. 543-550, 2004.

[19] Q. Jianga, X.M. Yangb, H.G. Zhoub, and J.S. Yangb, "Analysis of surface acoustic wave pressure sensors," *Sensors and Actuators A*, vol. 118, pp. 1–5, 2005.

[20] B. Joo , J. Huhb, and D. Lee Sensors, "Fabrication of polymer SAW sensor array to classify chemical warfare agents," *Sensors and Actuators B*, vol. 121, pp. 47–53, 2007.

[21] R. Arsat, M. Breedon, M. Shafiei, P.G. Spizziri, S. Gilje, R.B. Kaner, K. Kalantar-zadeh, and W. Wlodarski," Graphene-like nano-sheets for surface acoustic wave gas sensor applications," *Chemical Physics Letters,* vol. 467, pp. 344–347, 2009.

[22] G. L. Dybwad, "A sensitive new method for determination of adhesive bonding between a particle and a substrate," *Journal of Applied Physics*, vol. 58, pp. 2789-2790, 1985.

[23] A. Pomorska, D. Shchukin, R. Hammond, M. A. Cooper, G. Grundmeier, and D. Johannsmann "Positive frequency shifts observed upon adsorbing micron-sized solid objects to a quartz crystal microbalance from the liquid phase," *Analytical Chemistry,* vol. 82 pp. 2237-2242, 2010.

[24] W.R. Smith, H. M. Gerard, J.H. Collins, T.M. Reeder, and H.J.Shaw, "Analysis of interdigital surface wave transducers by use of an equivalent circuit model," *IEEE Transactions on Microwave Theory and Techniques*, vol. 17, pp. 856–864, 1969.

[25] A. B. Bhattacharyya, S. Tuli, and S. Mazumdar, "Spice simulation of surface acoustic wave interdigital transducers, *IEEE Transactions on Ultrasonics, Ferroelectrics, and Frequency Control*, vol. 42, pp. 784-786, 1995.

[26] J. Munshi and S. Tuli, "A circuit simulation compatible surface acoustic wave interdigital transducer macro-model," *IEEE Transactions on Ultrasonics, Ferroelectrics, and Frequency Control*, vol. 51, pp. 782-784, 2004.

[27] V. Plessky and J. Koskela, "Coupling-of-modes analysis of SAW devices," *International Journal of High Speed Electronics and Systems*, vol. 10, pp. 867–947, 2000.

[28] T. T. Wu, S. M. Wang, Y. Y. Chen, T. Y. Wu, P. Z. Chang, L. S. Huang, C. L. Wang, C. W. Wu, and C. K. Lee, "Inversion determination of coupling of modes parameters of surface acoustic wave resonators," *Japanese Journal of Applied Physic.,* vol.41, pp. 6610–6615, 2002.

[29] B.A. Auld, *Acoustic Fields and Waves in Solids*, vol. 1. Malabar, Florida: Robert E. Krieger Publishing Company, 2 ed., 1990.

[30] D. Royer and E. Dieulesaint, *Elastic waves in solids I Free and Guided Propagation.* Berlin: Springer-Verlag, 2000.

[31] V. K. Varadan, K. J. Vinoy, and S. Gopalakrishnan, *Smart Material Systems and MEMS: Design and Development Methodologies*, England: John Wiley & Sons, 2007.

[32] T. R. Hsu, *MEMS and Microsystems: Design and Manufacture*, McGraw-Hill Science, 2001.

[33] *COMSOL Multiphysics Version 3.4 Documentation*, COMSOL AB, Stockholm, Sweden, 2007.

[34] R. Lerch, "Simulation of piezoelectric devices by two-and-three-dimensional finite elements," *IEEE Transactions on Ultrasonics, Ferroelectrics and Frequency Control*, vol. 37, pp. 233–247, 1990.

[35] S. Rahman, M. Kataoka, C. H. W. Barnes, and H. P. Langtangen, "Numerical investigation of a piezoelectric surface acoustic wave interaction with a one-dimensional channel," *Physical Review B*, vol. 74, p. 035308, 2006.

[36] M. Z. Atashbar, B. J. Bazuin, M. Simpeh, and S. Krishnamurthy, "3D FE simulation of H_2 SAW gas sensor," *Sensors and Actuators B*, vol. 111, pp. 213–218, 2005.

[37] D. H. Wu and H. H. Chen, "Application of Taguchi robust design method to SAW mass sensing device," *IEEE Transactions on Ultrasonics, Ferroelectrics, and Frequency Control*, vol. 52, pp. 2403-2410, 2005.

[38] S. J. Ippolitto, K. Kalantar-Zadeh, D. A. Powell, and W. Wloderski, "A 3- Dimensional Finite Element Approach for Simulating Acoustic Wave Propagation in Layered SAW devices," in *proc. IEEE Ultrasonics Symposium*, pp. 303 – 306, 2003.

[39] X. Wang, and G. Xu, "Numerical Study of the Effects of Film Properties to the Mass Sensitivity of Surface Acoustic Wave Sensors," in *proc. IEEE Ultrasonics Symposium*, pp. 442 – 448, 2005.

[40] G. Xu, "Direct finite-element analysis of the frequency response of a Y-Z lithium niobate SAW filter," *Smart Mater. Struct.*, vol.9, pp. 973–980, 2000.

[41] H. Subramanian, V. K. Vardan, V. V. Vardan, and M. J. Vellekoop, "Design and fabrication of wireless remotely readable MEMS based microaccelerometers," *Smart Mater. Struct.*, vol. 6, pp. 730–738, 1997.

[42] M. Hofer, N. Finger, G. Kovacs, J. Schoberl, S. Zaglmayr, U. Langer, and R. Lerch, "Finite-element simulation of wave propagation in periodic piezoelectric SAW structures," *IEEE Transactions on Ultrasonics, Ferroelectrics, and Frequency Control,* vol. 53, pp. 1192–1201, 2006.

[43] A. W. Warner, M. Onoe, and G. A. Coquin, "Determination of elastic and piezoelectric constants for crystals in class (3M)," *The journal of the acoustical society of America*, vol. 42, pp. 1223-1231, 1968.

[44] Z. C. Feng and C. Chicone, "A delay differential equation model for surface acoustic wave sensors," *Sensors and Actuators A*, vol. 104, pp. 171-178, 2003.

[45] D. S. Ballantine, R. M. White, S. I. Martin, A. I. Ricco, E. T. Zellers, G. C. Frye, H. Wohltjen, *Acoustic Waves Sensors theory, design, and physico – chemical Applications*. New York: Academic Press, 1997.

[46] A. Fabre, E. Finot, J. Demoment, and S. Contreras, "In situ measurement of elastic properties of PdHx, PdDx, and PdTx," *Journal of Alloys and Compounds,* vol. 356-357, pp. 372-376, 2003.

[47] M. Penza, M. A. Tagliente, P. Aversa, and G. Cassano, "Organic-vapor detection using carbon-nanotubes nanocomposite microacoustic sensors," *Chemical Physics Letters*, vol. 409, pp. 349 - 354, 2005.

[48] T. Nomura, M. Takebayashi, and A. Saitoh, "Chemical sensor based on surface acoustic wave resonator using langmuir-blodgett film," *IEEE Transactions on Ultrasonics, Ferroelectrics, and Frequency Control,* vol. 45, pp. 1261-1263, 1998.

[49] Z. Chen and C. Lu, "Humidity sensors: a review of materials and mechanisms," *Journal of Sensor letters*, vol. 3, pp. 274–295, 2005.

[50] M. Penza and G. Cassano, "Relative humidity sensing by PVA-coated dual resonator SAW oscillator," *Sensors and Actuators B: Chemical*, vol. 68, pp 300-306, 2000.

[51] N. M. Tashtoush, J. D. N. Cheeke, N. Eddy , "*Surface acoustic wave humidity sensor based on a thin PolyXIO film*," *Sensors and Actuators B*, vol. 49, pp. 218–225, 1998.

[52] S. J. Ippolito, A. Ponzoni, K. Kalantar-zadeh, W. Wlodarski, E. Comini, G. Faglia, and G. Sberveglieri, "Layered WO3/ZnO/36° LiTaO3 SAW Gas Sensor Sensitive Towards Ethanol Vapour and Humidity," *Sensors and Actuators B: Chemical*, vol. 117, pp. 442-450, 2006.

[53] T. T. Wu, Y. Y. Chen and T. H. Chou, "*A high sensitivity nanomaterial based SAW humidity sensor*," *Journal of Physics D: Applied Physics*, vol. 41, p. 0815109, 2008.

[54] A. Khan, "Preparation and characterization of *N*-isopropylacrylamide/acrylic acid copolymer core–shell microgel particles*," Journal of Colloid and Interface Science,* vol. 313, pp. 697–704, 2007.

[55] V. Laude, L. Robert, W. Daniau, A. Khelif and S. Ballandras, "Surface acoustic wave trapping in a periodic array of mechanical resonators", *Applied Physics Letters*, vol. 89, p. 083515, 2006.

[56] L. Calabri, N. Pugno, W. Ding, and R. S. Ruoff, "Resonance of curved nanowires," *Journal of Physics: Condensed Matter,* vol. 18, p.2175, 2006.

[57] Q. Jiang, X. M. Yang, H. G. Zhou, and J. S. Yang, "Analysis of surface acoustic wave pressure sensors," *Sensors and Actuators A*, vol. 118, pp. 1- 5, 2005.

[58] W. Jakubik, M. Urbanczyk, S. Kochowski, and J. Bodzenta, "Surface acoustic wave hydrogen sensor with nickel pthalocyanine and palladium thin film layers," *Molecular and Quantum Acoustics*, vol. 23, pp. 473-482, 2002.

[59] K. Yamanaka, S. Ishikawa, N. Nakaso, and N. Takeda, "Ball SAW device for hydrogen gas sensor,"*proc. IEEE Ultrasonic Symposium*, pp. 299 – 302, 2003.

[60] Y. Im, C. Lee, R. P. Vasquez, M. A. Bangar, N. V. Myung, E. J. Menke, R. M. Penner, and M. Yu, "Investigation of a single Pd nanowire for use as a hydrogen sensor," *Small*, vol. 2, pp. 356 -358, 2006.

[61] E. C. Walter, F. Favier, and R. M. Penner, "Palladium mesowire arrays for fast hydrogen sensors and hydrogen-actuated switches," *Analytical Chemistry*, vol. 74, pp. 1546 -1553, 2002.

[62] F. Favier, E. C. Walter, M. P. Zach, T. Benter, and R. M. Penner, "Hydrogen sensors and switches from electrodeposited palladium mesowire arrays," *Science*, 2001, vol. 293, pp. 2227-2231.

[63] X. M. H. Huang, M. Manolidis, S. C. Jun, and J. Honea, "Nanomechanical hydrogen sensing,"*Applied Physical Letters*, vol. 86, p. 143104-1, 2005.

[64] A. Z. Sadek, W. Wlodarski, Y.X. Li, W. Yu, X. Li, X. Yu, and K. Kalantar-zadeh, "A ZnO nanorod based layered ZnO/64° YX LiNbO3 SAW hydrogen gas sensor," *Thin Solid Films*, vol. 515, pp. 8705-8708, 2007.

[65] V. R. Bhenthanabotla and S. Bhansali, *US Patent: 7047792*.

[66] Y. S. Huang, Y. Y. Chen, and T. T. Wu, "A passive wireless hydrogen surface acoustic wave sensor based on Pt-coated ZnO nanorods," *Nanotechnology*, vol. 21, p. 095503, 2010.

[67] M. M. E. L. Gowini and W. A. Moussa, "A finite element model of a MEMS-based surface acoustic wave hydrogen sensor," *Sensors*, vol. 10, pp. 1232- 1250, 2010.

[68] "Roditi-International", http://www.roditi.com/SingleCrystal/LiNbO3/LiNbO3.html

[69] T. T. Wu, H. T. Tang, and Y. Y. Chen, "Frequency response of a focused SAW device based on concentric wave surfaces: simulation and experiment," *J. Phys. D: Appl. Phys.*, vol. 38, pp. 2986–2994, 2005.

[70] S. Natarajan, D. A. C. Yen, and B. K. Gale "Large-area, high-aspect-ratio SU-8 moulds for the fabrication of PDMS microfluidic devices," *Journal of Micromechanics and Microengineering*, vol. 8, pp. 045021, 2008.

[71] G. Liu, Y. Tian, and Y. Kan, "Fabrication of high-aspect-ratio microstructures using SU-8 photoresist," *Microsystem Technologies*, vol. 11, pp. 343–346, 2005.

[72] K. D. Vora, B. Y. Shew, E. C. Harvey, J. P. Hayes, and A. G. Peele, "Specification of mechanical support structures to prevent SU-8 stiction in high aspect ratio structures," *Journal of Micromechanics and Microengineering*, vol. 15, pp. 978–983, 1998.

[73] D. Fukuoka, and Y. Utsumi, "Fabrication of the cyclical fluid channel using the surface acoustic wave actuator and continuous fluid pumping in the cyclical fluid channel," *Microsystem Technology*, vol. 14, pp. 1395–1398, 2008.

[74] L. Dellmann, S. Roth, C. Beuret, G. A. Racine, H. Lorenz, M. Despont, P. Renaud, P. Vettiger P, N. F. de Rooij, "Fabrication process of high aspect ratio elastic and SU-8 structures for piezoelectric motor applications," *Sensors and Actuators A*, vol.70, pp.42-47, 1998.

[75] SU-8 2035 Datasheet, http://www.microchem.com/products/pdf/SU-8_2035-2100.pdf

[76] OmniCoat Datasheet, http://www.microchem.com/products/pdf/OMNICOAT.pdf

[77] A. Laschitsch and D. Johannsmann, "High frequency tribological investigations on quartz resonator surfaces," *J. Appl. Phys.*, vol. 85, 1999, pp. 3759-3766, 1999.

[78] Q. L. Zhang, R. M. Lec, R. M, and K. Pourrezaei, "The study of an interaction of solid particles with various surfaces using TSM sensors," *IEEE Trans. Ultrason. Ferroelectr. Freq. Control*, vol. 53, pp. 167-174, 2006.

[79] E. Corrales, J. Verdu, P. de Paco, and O. Menendez, "Analysis technique for asymmetrically coupled resonator structures," *IEEE Transactions on Ultrasonics, Ferroelectrics, and Frequency Control*, vol.56, pp.1703-1707, 2009.

[80] "Piezoelectric Materials and Devices," http://www.newpiezo.com/product.html

[81] "SU-8: Thick Photoresist for MEMS," http://memscyclopedia.org/su8.html

List of Publications Related to Thesis

International Journal Publications

1. N. Ramakrishnan, Harshal B. Nemade, and Roy Paily Palathinkal "Mass Loading in Coupled Resonators Consisting of SU-8 Micro-Pillars Fabricated over SAW Devices," *IEEE Sensors Journal*, 2010, vol. 11,pp. 430-431. (doi:10.1109/JSEN.2010.2074193)

2. N. Ramakrishnan, Roy Paily Palathinkal, and Harshal B. Nemade, "Mass loading effects of high aspect ratio structures grown over SAW resonators," *Sensor Letters*, 2010, vol. 8, No. 2, pp. 253-257. (doi:10.1166/sl.2010.1258).

3. N. Ramakrishnan, Harshal B. Nemade, and Roy Paily Palathinkal "Finite element simulation of a surface acoustic wave hydrogen sensor with palladium nano-pillars as sensing medium," *Sensor Letters,* 2010, vol. 8, No. 6, pp. 824-828. (In Press, doi:10.1166/sl.2010.1352)

4. N. Ramakrishnan, T. Vamsi, A. Khan, Harshal B. Nemade, and Roy Paily Palathinkal, "Humidity sensor using NIPAAm nanogel as sensing medium in SAW devices," *International Journal of Nanoscience*, vol.10, 2011.(**In press**)

5. N. Ramakrishnan, Harshal B. Nemade, and Roy Paily Palathinkal "Fabrication of high aspect ratio SU-8 microstructures on piezoelectric transducers," (Submitted)

6. N. Ramakrishnan, Harshal B. Nemade, and Roy Paily Palathinkal "Experimental study on mass loading characteristics of high aspect ratio structures on surface acoustic wave sensors," (Submitted)

Patents Filed

1. N. Ramakrishnan, Harshal B. Nemade, and Roy Paily Palathinkal, "High aspect ratio resonant structures in surface acoustic wave devices," 2009, **Indian patent filed (No: 822/KOL/2009, CBR No.: 3600)**

Conference Publications

1. N. Ramakrishnan, Harshal B. Nemade, and Roy Paily Palathinkal, "Simplified finite element simulation of a SAW hydrogen sensor using COMSOL Multiphysics," *COMSOL Multiphysics user Conference* (Germany), Nov. 2008.

2. N. Ramakrishnan, Harshal B. Nemade, and Roy Paily Palathinkal, "Finite element method study of SAW sensor for mass sensitivity," *ICDF* (Coimbatore, India), Aug. 2008.

3. N. Ramakrishnan, Harshal B. Nemade, and Roy Paily Palathinkal, "Simulation of one port SAW resonator using COMSOL Multiphysics," *COMSOL Multiphysics user Conference* (Bangalore, India), Nov. 2006 (**BEST PAPER AWARD**).

4. N. Ramakrishnan, Harshal B. Nemade, and Roy Paily Palathinkal, "Modeling and analysis of SAW based liquid sensors," *Eighth International Conference on Nanostructured Materials* (Bangalore, India), Aug. 2006.

5. N. Ramakrishnan, Roy Paily Palathinkal,and Harshal B. Nemade, "Design of SAW based biosensor for heavy metal ion detection," *International Symposium on Nano-Bio Interface* (Kolkata, India), March 2006.